PHYSIK-DEPARTMENT

Measurement of the $\mu^+\mu^-$ Background for Neutral MSSM Higgs Searches with the ATLAS Detector

Diplomarbeit
von

Sebastian Stern

3. November 2009

TECHNISCHE
UNIVERSITÄT
MÜNCHEN

$\Delta p \cdot \Delta q \geq \frac{1}{2}\hbar$

Max-Planck-Institut für Physik
(Werner-Heisenberg-Institut)

Abstract

The subject of this work is the development of a data-driven method for the background estimation for neutral MSSM Higgs searches in the decay channel $h/H/A \rightarrow \mu^+\mu^-$. The method employs signal-free control samples from the e^+e^- and $e^\pm\mu^\mp$ final states and is based on the vanishing decay rate $h/H/A \rightarrow e^+e^-$. In contrast, for the background processes the decay rates into electrons and muons are equal at particle level. Differences between the electron and muon final states at reconstruction level arising from the detector response and the presence of Bremsstrahlung and final state radiation are studied in detail. The accuracy of the method is evaluated for the dominant background contributions from Z boson and $t\bar{t}$ decays. Detector-related systematic uncertainties concerning muon, electron and jet reconstruction are taken into account. Finally, the presented method for the background estimation is used to evaluate the exclusion limits at a confidence level of $95\,\%$.

Acknowledgments

I would like to thank all the people who supported me during the work on my diploma thesis.

First of all, I want to thank PD Dr. Hubert Kroha for giving me the chance to do my diploma thesis in the MDT group at the Max Planck Institut für Physik. I thank him for his help and support during the last year and for his thorough corrections of my work.

I want to express my greatest thanks to my immediate supervisor Dr. Sandra Horvat, for the huge amount of time she spent on discussing my results, helping me to focus on the essentials and guiding me through the whole year. Many thanks for the days and nights she spent during the last weeks to correct my thesis and making it possible to finish in time.

I also want to thank all the members of the MDT group for the great working atmosphere. It's been a pleasure, guys!

Zu guter Letzt möchte ich meinen Eltern Gudrun und Karl-Heinz Stern für ihre Unterstützung danken und dafür, dass sie mir mein Studium ermöglicht haben.

Contents

Chapter 1

Overview

The Large Hadron Collider (LHC) at CERN is now ready to start operations and first collisions are expected in late 2009. In the next 15 years the LHC will produce proton-proton collisions with a centre-of-mass energy of up to $\sqrt{s} = 14\,\mathrm{TeV}$ at a luminosity of up to $10^{34}\,\mathrm{cm}^2\mathrm{s}^{-1}$. This will allow to discover and study new phenomena which can give answers to open questions in our current understanding of the elementary particles, their interactions and the early evolution of the universe. In particular, the general-purpose detector ATLAS is designed to discover a large variety of new physics processes. The design and the properties of the ATLAS detector and the LHC are summarized in Chapter 2 since this thesis as been performed in the context of the ATLAS experiment.

Our current understanding of the elementary constituents of matter is combined in the standard model of particle physics. This theory was developed during the last century, has been tested thoroughly in the past decades and has proven to be extremly successful providing predictions of unprecedented accuarcy and very good agreement with measurements. The only prediction of the standard model which could not be confirmed yet by experiments is the existence of the Higgs boson. Its discovery is one of the main goals of the ATLAS experiment. In spite of its success, the standard model cannot give satisfactory answers to several observations and open questions in particle physics. Therefore many new theories have been developed which contain the standard model as an effective theory at low energies. One prominent model is the minimal supersymmetric standard model (MSSM) which introduces supersymmetry to the standard model with minimum modifications. Besides the extended particle content due to supersymmetric particles, the MSSM predicts five Higgs bosons, three neutral and two charged ones. In this thesis, the search for the neutral MSSM Higgs bosons with the ATLAS experiment is studied. An overview, of the standard model and the MSSM is given in Chapter 3.

The decay modes of the neutral MSSM Higgs bosons called A, h, H depend on a large number of parameters. In this thesis a common scenario is assumed where the couplings of the Higgs bosons to down-type fermions are strongly enhanced. In this case, the dominant discovery channel is the decay into a τ-lepton pair. With respect to this mode, the decay into two muons is suppressed. On the other hand the latter channel provides a very clean signature. In Chapter 4, the search for $h/H/A \rightarrow \mu^+\mu^-$ decays is discussed with focus on the study of the detector performance for the reconstruction of the signal signature. Furthermore, the signal production and the dominant background processes are discussed. Since the $h/H/A \rightarrow \mu^+\mu^-$ channel suffers from a low branching ratio and the signal is superimposed by standard model processes with high cross sections, both for discovery and exclusion of the signal, the background has to be known very well. In Chapter 5, a method for the estimation of the background from measured collision data is presented which employs signal-free control samples. The method makes use of the equal branching ratios and kinematic properties of the decays into electrons and muons in the background processes at particle level. Different effects on the reconstruction level which can degrade the performance of this method are studied in detail. Possible systematic effects arising from the event selection criteria are also discussed in this chapter. Finally the accuracy of the background estimation is evaluated for different integrated luminosities to probe its performance under several early data taking scenarios.

Systematic uncertainties play an important role for the signal sensitivity, especially for early data runs where several detector effects still have to be understood. The effects of systematic uncertainties on the expected signal and background as well as on the background estimation are studied in Chapter 6 with conservative assumptions on the level of understanding the detector performance.

Finally, in Chapter 7 the performance of the background estimation method developed in this thesis is tested. For that purpose the exclusion limits for the decay $h/H/A \to \mu^+\mu^-$ are evaluated using information from the control samples.

Chapter 2

The LHC and the ATLAS Experiment

The standard model of particle physics is one of the best theories ever established. Nevertheless neither all particles that are predicted by the standard model have been found, nor the standard model can answer all open questions remaining in particle physics. To discover further hints that could either prove the standard model or lead to new physics beyond, more powerful accelerators are needed that allow to create heavier particles or to study very rare processes. The Large Hadron Collider (LHC) at CERN is the next step in this progress. After more than 15 years of design and construction, it will be ready to start operations in autumn 2009. Four experiments will study the proton-proton and heavy ion collisions produced by the LHC: The two multi-purpose detectors ATLAS and CMS, the B-physics experiment LHCb dedicated to the CP-violation in the B-system and ALICE, an experiment specialized in heavy ion collsions to study the quark-gluon plasma.
Since this thesis is performed in the context of the ATLAS experiment, LHC and ATLAS are briefly introduced in the following. This chapter is based on the references [1] and [2] which provide more detailed information on this topic.

2.1 The Large Hadron Collider

The Large Hadron Collider (LHC) is an accelerator ring located at CERN[1] near Geneva and crosses the border of Switzerland and France. It is installed in the tunnel of the former LEP[2] e^+e^- collider which has a circumference of $26.7\,\mathrm{km}$. More than 1200 superconducting dipole magnets with a design magnetic field of more than $8\,\mathrm{T}$ deflect the two proton beams which are accelerated to an energy of up to 7 TeV per beam in opposite direction. This leads to proton-proton collisions with a maximum centre-of-mass energy of $\sqrt{s} = 14\,\mathrm{TeV}$. Each beam is divided into ~ 2800 bunches with up to 10^{11} protons per bunch. At a corresponding design luminosity of $\mathcal{L} = 10^{34}\,\mathrm{cm}^{-2}\mathrm{s}^{-1}$ the bunches will collide 40 million times per second at four interaction points where the experiments are placed. Figure 2.1 shows a drawing of the LHC ring and its four experiments ATLAS, CMS, ALICE and LHCb.
On average 24 inelastic p-p collisions will occur in every bunch crossing which leads to a severe experimental challenge: every possible interesting event is overlaid by 23 pile-up interactions. Furthermore due to the dominating QCD jet production cross-sections the pile-up is generally characterized by a large QCD jet activity. Therefore the LHC

---

[1] Counseil Européen pour la Recherche Nucléaire
[2] Large Electron Positron Collider

experiments have to be able to identifiy the rare physics processes of interest in a high background environment.

The LHC is also designed for heavy ion collisions. In this operation mode lead nuclei with an energy of $2.26\,\mathrm{TeV}$ per nucleon are used to probe for example the formation of the quark-gluon plasma. This colour-deconfined state of matter is supposed to be created at very high energy densities as they were present in the early evolution of the universe. In this operation mode the LHC can achieve a luminosity of $10^{27}\mathrm{cm}^{-2}\mathrm{s}^{-1}$.

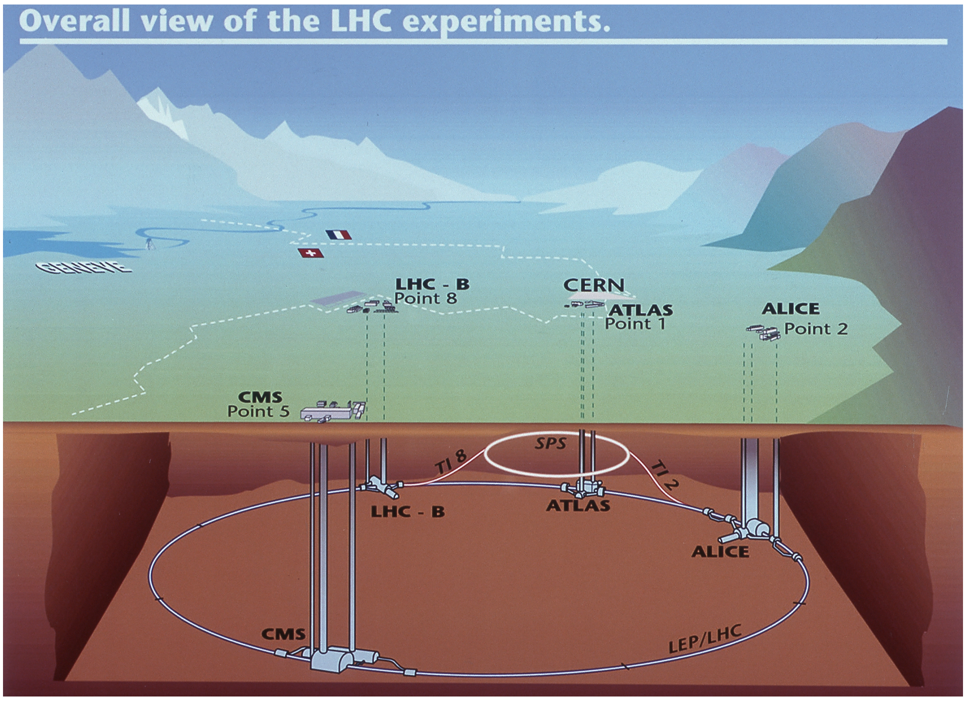

Figure 2.1: Schematic drawing of the LHC accelerator and the four experiments ALICE, ATLAS, CMS and LHCb. On the surface the CERN site and the access points are shown.

During the beam commissioning phase in September 2008 proton beams at an energy of $450\,\mathrm{GeV}$ circulated successfully in the LHC for the first time. On September 19^{th} a faulty superconducting connection between two dipole magnets lead to a severe damage of several magnets in one sector. The repair work demanded a shutdown which is still ongoing. Due to this incident it is planned to restart LHC operation in autumn 2009 with lower centre-of-mass energy and luminosity. During the first year of operation one expects an integrated luminosity of about $200\,\mathrm{pb}^{-1}$ at a centre-of-mass energy of $\sqrt{s} = 10\,\mathrm{TeV}$. The work presented in this thesis is dedicated to the analysis of those early collision data.

2.2 The ATLAS Experiment

The ATLAS[3] detector is a multi-purpose experiment. With its overall size of $44\,\mathrm{m}$ in length and $25\,\mathrm{m}$ in height it is the largest particle detector ever built. Figure 2.2 gives an overview of the ATLAS detector and its subdetectors. The experiment is designed to study the rich physics potential at the LHC, ranging from precision measurements of standard model parameters up to the search for new physics phenomena. The following list introduces a few benchmark physics goals:

---

[3] A Toroidal LHC ApparatuS

- The precision measurements of the standard model parameters include the measurement of the top-quark and gauge boson properties, since those particles will be produced in abundance at the LHC. An accurate measurement of the corresponding production cross-sections allows for a better understanding of the background contributions to all new physics searches.

- The most prominent new particle ATLAS is searching for is the Higgs boson. The Higgs boson of the standard model will be produced with a very low cross-section of some $10\,\mathrm{pb}$, depending on its mass and it will decay in several decay modes. For a discovery of the Higgs boson therefore several decay channels have to be studied. This puts stringed requirements on the detector performance in particle and jet identification, momentum measurements and the reconstruction of the missing transverse energy E_T^{miss}. Similar searches are also performed for the Higgs bosons predicted by supersymmetric theories.

- In supersymmetric theories with conserved R-parity the sleptons and gauginos are decaying in cascades, producing standard model particles and a lightest stable supersymmetric particle (LSP). The LSP interacts only weakly and therefore escapes the detector without leaving any signal. This would result in a significant missing transverse energy and therefore requires a reliable measurement of E_T^{miss}.

- With its unprecedented centre-of-mass energy the LHC provides access to a wide sprectrum of new exotic physics processes. The range of exotic physics reaches from heavy gauge bosons W' and Z' over lepton flavour violation (LFV) up to the creation of mini black holes. To be sensitive to such signatures ATLAS has to provide for a good charge identification and high-resolution momentum measurements and charge identification of leptons and jets in the TeV-range.

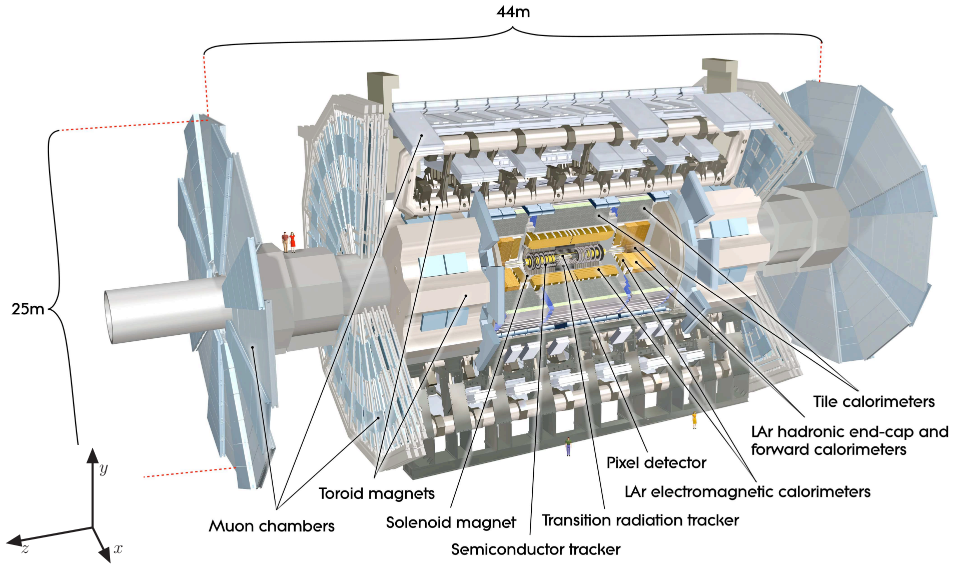

Figure 2.2: Cut-away view of the ATLAS detector. The overall dimensions and its subsystems are indicated.

For many of the above processes one expects very low cross-sections and therefore high luminosity and interaction rates are aimed. This leads on the other hand to a high experimental challenge to cope with: With the cross-section for inelastic proton-proton collisions of $80\,\mathrm{mb}$ the LHC will produce 10^9 inelastic events per second which implies that every potential new physics event will be overlayed by 23 inelastic events per bunch crossing.

To study the wide range of physics under the hard experimental conditions ATLAS has to fulfill the following requirements:

- Fast and radiation-hard electronics and sensor elements with high detector granularity to cope with the high particle fluxes.
- Hermetic detector coverage around the interaction point up to the very forward regions for a precise measurement of the missing transverse energy.
- Excellent momentum resolution and reconstruction efficiency of charged particles.
- High-resolution tracking detectors close to the interaction point to reconstruct the tracks as well as primary and secondary vertices in a high-track density environment.
- Electromagnetic calorimeter with high energy and spatial resolution to identify electrons and photons and measure their energy as precise as possible.
- Hermetic hadronic calorimeter to measure the jet energies and E_T^{miss}.
- Efficient trigger system which provides strong background rejection combined with high signal efficiencies at very high event rates.

The above requirements have set the standards for the design of the ATLAS detector. In the following the most important parts of ATLAS will be described in detail. The innermost part is the traching detector (inner detector), surrounded by the electromagnetic and hadronic calorimeters. The outermost part is the muon spectrometer. The inner detector and the muon spectrometer are operated in a magnetic field which bends the charged particle trajectories and thus allows for a charge and momentum measurement.

2.2.1 The ATLAS Coordinate System

The ATLAS coordinate system (see Fig. 2.2) is used throughout this thesis and should be presented briefly:

- The nominal interaction point defines the origin of the right-handed coordinate system.
- The positive x-axis is pointing to the centre of the LHC ring.
- The positive y-axis is pointing upwards.
- The positive z-axis is pointing in beam direction to the LHCb experiment.
- The azimuthal angle ϕ is measured around the beam axis.
- The polar angle θ is the measured from the beam axis.
- The pseudorapidity is defined as $\eta = -\ln\tan(\theta/2)$
- Quantities like the transvers momentum p_T, the transverse energy E_T and the missing transverse energy E_T^{miss} are defined as projections into the x-y plane.
- The angular distance ΔR in the (η, ϕ)-space is defined as $\Delta R = \sqrt{\Delta\eta^2 + \Delta\phi^2}$

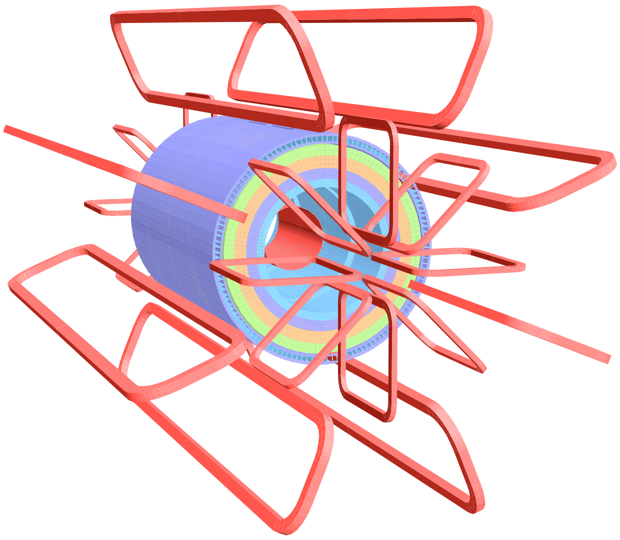

Figure 2.3: Geometry of the magnet coils and the tile calorimeter steel. The eight barrel toroid and end-cap coils are indicated, the solenoid coil is placed inside the calorimeter volume. For clarity the end-cap calorimeters are not displayed.

2.2.2 The Magnet System

The ATLAS magnet system consists of 4 superconducting magnets, the solenoid, the barrel toroid and two end-cap toroid magnets. The whole system is 26 m long and 22 m in diameter and stores an energy of $1.6\,\mathrm{GJ}$. A complete view on the layout of the magnet coils and a sketch of the field configuraton is shown in Figures 2.3 and 2.4.

The inner detector is surrounded by a thin solenoid magnet providing a magnetic field of $2\,\mathrm{T}$ in beam direction. The magnet coil has a diameter of $2.6\,\mathrm{m}$ and a length of $5.8\,\mathrm{m}$. Close to the interaction point the field is highly homogeneous. Since the solenoid is placed in front of the calorimeter system its radiative thickness is minimised to achieve a maximum calorimeter performance. Therefore the central solenoid shares the same vacuum vessel as the electromagnetic liquid argon calorimeter and the iron absorber of the tile calorimeter is used as return yoke for the solenoid field.

Outside the calorimeter system the superconducting toroid magnets provide a large magnetic field with a volume of more than $11000\,\mathrm{m}^3$ in which the muon spectrometer is integrated. The toroidal layout provides a field which is mostly orthogonal to the muons trajectories and the air-core design minimises the degradation of resolution due to multiple scattering. In the barrel part eight coils housed in their own cryostats provide a non-homogeneous field of $0.5-2.5\,\mathrm{T}$ resulting in a bending power[4] of $1.5-5.5\,\mathrm{Tm}$. The length of the barrel toroid system is 25 m with inner and outer diameters of $9.4\,\mathrm{m}$ and $20.1\,\mathrm{m}$.

In the end-cap region, additional eight coils are placed in one cryostat on each side of the barrel region. This completes the toroidal field to large pseudorapidities. The end-cap toroids produce a magnetic field of $0.5 - 3.5\,\mathrm{T}$ which translates in a bending power of $1.0 - 7.5\,\mathrm{Tm}$. To keep the bending power in the transition region between barrel and end-cap toroids as high as possible, the end-cap toroids are to some extent inserted in the barrel toroid and rotated by 22.5° with respect to the barrel coils. Each end-cap toroid is $5\,\mathrm{m}$ in axial length and has inner and outer diameters of $1.6\,\mathrm{m}$ and $10.7\,\mathrm{m}$ respectively.

---

[4] The performance of the magnet system is given in terms of the bending power. The bending power is calculated via the field integral $\int B_\perp \mathrm{d}l$ along a trajectory of an infinite-momentum muon between the innermost and outermost planes of the muon spectrometer. $B_\perp$ is the field component orthogonal to the muon direction.

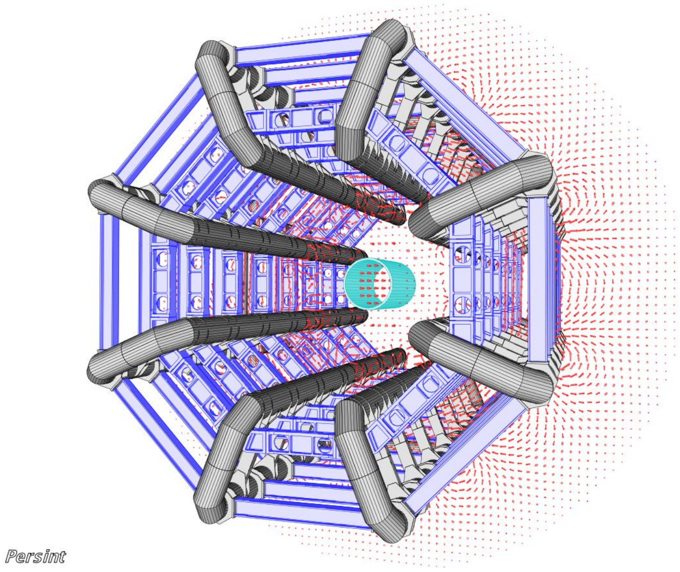

Figure 2.4: Sketch of the magnetic field configuration of the ATLAS detector. The field is projected on the x-y plane at $z = 0$. The barrel toroid coils and the central solenoid are shown. For clarity the end-cap toroid coils are not displayed.

2.2.3 The Inner Detector

At a design luminosity approximately 1000 particles will emerge at the interaction point every 25 ns in a pseudorapidity range of $|\eta| < 2.5$. In this high track density environment the main requirements on the ATLAS inner detector (ID) are robust pattern recognition, excellent momentum resolution and both primary and secondary vertex reconstruction for charged tracks within a pseudorapidity range up to $|\eta| < 2.5$. In addition the inner detector has to perform in a high-radiation environment which poses stringent requirements on the sensors, electronics and mechanical structure. The complete inner detector has a length of 3.5 m and a diameter of 2.3 m and is surrounded by the solenoid magnet which provides a magnetic field of 2 T. A view of the complete inner detector is shown in Figure 2.5.

The inner detector consists of three independent sub-detectors:

The innermost part, the **pixel detector** constists of three silicon-pixel layers in the barrel part and additional three discs in each end-cap. A total of more than 80 million pixels, each with a size of $50 \times 400\,\mu\mathrm{m}^2$ and equipped with an individual readout channel, measure discrete space-points of charged particles with an excellent resolution of $10\,\mu\mathrm{m}$ in the $(R-\phi)$ plane and $115\,\mu\mathrm{m}$ in the $z\,(R)$ direction in the barrel (endcap) region.

The pixel detector is surrounded by the **semiconductor tracker** (SCT). Four layers of small-angle stereo silicon microstrip sensors in the barrel part and nine discs in each end-cap region provide another set of space-points for each charged particle originating from the interaction point. The microstrips are about 6 cm long and have a pitch of $80\,\mu\mathrm{m}$. To measure two coordinates, the strips of one sensor pair are rotated 40 mrad with respect to each other. The resulting position resolution is $17\,\mu m$ in $(R-\phi)$ and $580\,\mu m$ in $z\,(R)$ for the barrel (endcap) region. In total, the SCT has 6.3 million readout channels.

The outermost part of the ID is the **transition radiation tracker** (TRT). In total more than 350000 straw drift tubes in $73\,(160)$ layers in the barrel (endcap) region filled with an $Xe/CO_2/O_2$ gas mixture provide an average of 36 additional hits per track for $|\eta| < 2$. In addition X-rays from transition radiation produced in carbon fibers and foils between the layers can be detected to contribute to the discrimination between electrons and hadrons. The intrinsic resolution of a single straw tube is $130\,\mu m$ in $(R-\phi)$, the z (R) coordinate is

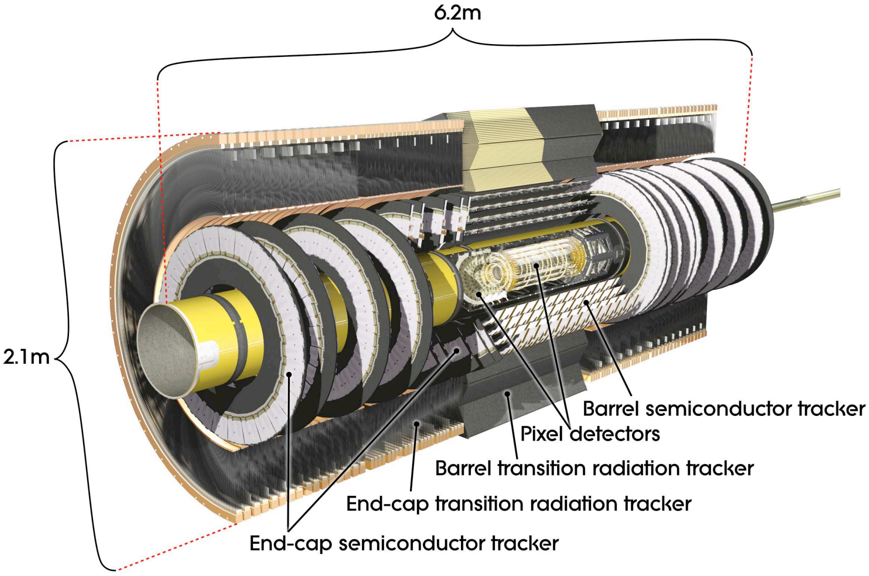

Figure 2.5: Cut-away view of the ATLAS inner detector.

not measured in the barrel (end-cap) region.

2.2.4 The Calorimeter System

The ATLAS calorimeter system is composed of different types of sampling calorimeters dedicated to the various physics requirements over the large η-range up to $|\eta| = 4.9$. A view of the complete calorimeter system is shown in Figure 2.6. The requirements on the calorimeters are a maximum coverage of the solid angle around the interaction point and a good containment of electromagnetic and hadronic showers to minimise punch-through effects. The latter is provided by a sufficient calorimeter thickness. Optimization of these requirements allows for the desired performance of the jet reconstruction and E_T^{miss} measurements. Futhermore a fine granularity in the electromagnetic calorimeter is needed for precision measurements of electrons and photons. In total, there are about 250000 readout channels in the ATLAS calorimeter system.

2.2.4.1 Electromagnetic Calorimeter

The electromagnetic (EM) calorimeter is a liquid argon (LAr) sampling calorimeter. The active material LAr is flushing accordion-shaped kapton electrodes and lead absorber plates. The accordion geometry provides complete symmetry in ϕ without azimuthal cracks.

In the barrel part ($|\eta| < 1.475$) the LAr calorimeter shares a common vacuum vessel with the central solenoid to reduce absorbing material in front of the calorimeters. The barrel calorimeter is separated in two halves divided by a gap of $4\,mm$ at $z = 0$.

The end-cap calorimeters ($1.375 < |\eta| < 3.2$) housed in their own cryostats are divided in two coaxial wheels on each side. The outer wheel covers a η region of $1.375 < |\eta| < 2.5$, the inner one a region of $2.5 < |\eta| < 3.2$.

In addition for $|\eta| < 1.8$ a presampling detector is placed in front of the calorimeter to allow for corrections for the energy lost by electrons and photons in the inner detector, cyrostat and magnet coils. It consists of an active LAr layer of 1.1 cm (0.5 cm) thickness in the barrel (endcap) region.

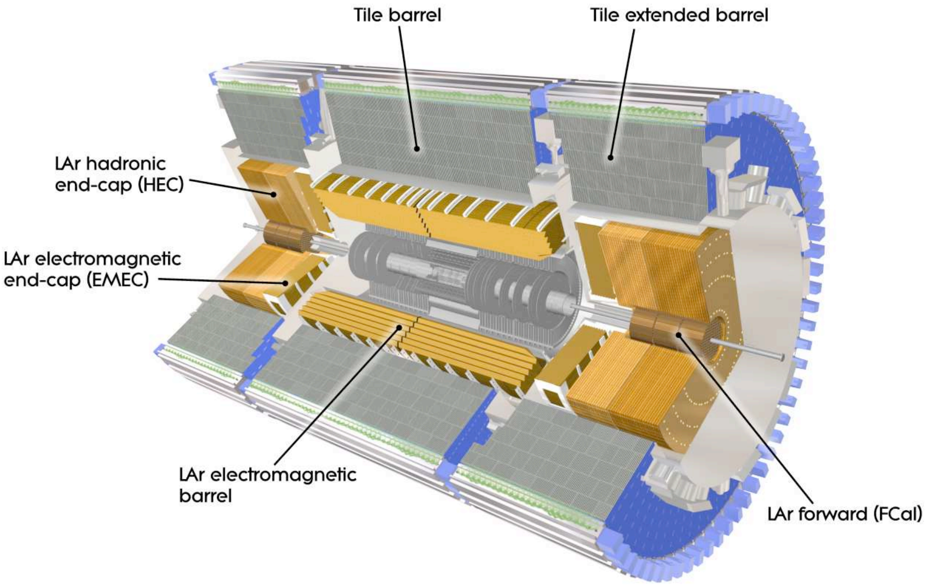

Figure 2.6: Cut-away view of the ATLAS calorimeter system.

2.2.4.2 Hadron Calorimeters

Due to the performance requirements and the η-dependent radiation rate the ATLAS hadron calorimeter is divided into three parts.

Immediately outside the EM calorimeter cryostat the tile calorimeter is placed. It consists of a barrel part ($|\eta| < 1.0$) and and two extended barrel parts ($0.8 < |\eta| < 1.7$) on each side of the detector. Steel absorbers between scintillating tiles as active materials are used in this sampling calorimeter.

At higher $|\eta|$ just behind the EM end-cap calorimeter the hadronic end-cap calorimeter (HEC) is placed. It uses copper plates as absorbers interleaved with gaps for the active LAr medium. To provide a good hermeticity the HEC overlaps with the tile calorimeter as well as with the LAr forward calorimeter resulting in a pseudorapidity coverage of $1.5 < |\eta| < 3.2$.

At very high η the forward calorimeter (FCal) is integrated into the end-cap cryostats. With its η coverage from 3.1 up to 4.9 it increases the uniformity of the whole calorimeter system. The FCal is separated into three modules in each end-cap: the first, using copper as passive material, is optimised for electromagnetic measurements, whereas the outer two modules are designed to measure hadronic interactions and therefore tungsten is used as absorber. Similarly as in the HEC and EM calorimeter, LAr is used as active material, allowing for a reliable operation in high-radiation environments.

2.2.5 The Muon Spectrometer

The outermost and at the same time the largest part of ATLAS is the muon spectrometer (MS) shown in Figure 2.7. The momentum of muons escaping the calorimeters is measured via their deflection in the magnetic field of the large superconducting air-core toroid magnet. Muons from the interaction point feel a bending power of approximately $1 - 7.5\,\mathrm{Tm}$ and their trajectories are measured in trigger and precision chambers that are embedded in the magnetic field. Three cylindrical layers of chambers in the barrel part and three wheels of chambers in each end-cap collect three space points for each muon track which allows for a full track reconstruction without using the information from the inner detector. The overall coverage of the muon spectrometer reaches up to $|\eta| = 2.7$. In the range $|\eta| < 1.4$ the muons are deflected by the barrel toroid and for $1.6 < |\eta| < 2.7$ the bending is provided by the end-cap toroids. In the transition region between $1.4 < |\eta| < 1.6$ the deflection is provided by a combination of both fields.

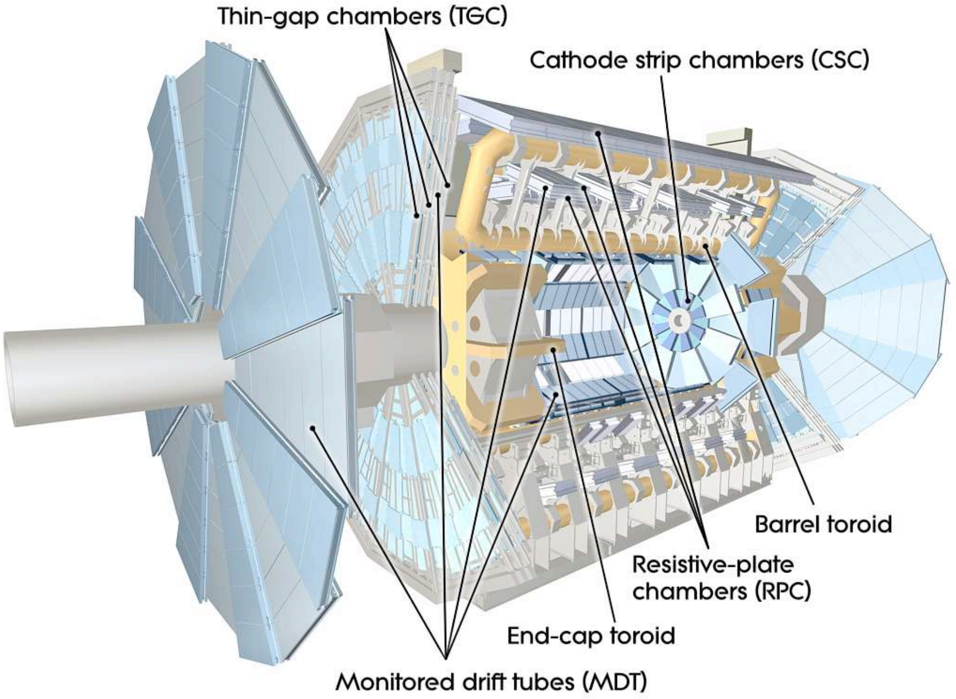

Figure 2.7: Cut-away view of the ATLAS muon spectrometer.

The requirements on the muon spectrometer are a stand-alone transverse momentum resolution of 3% for $200\,\mathrm{GeV}$ muons and better than 10% for $1\,\mathrm{TeV}$ tracks and also the capability to trigger on muon tracks for $|\eta| < 2.4$. To cope with these criteria the muon spectrometer is equipped with pairs of precision-tracking chambers and fast trigger chambers.

As trigger chambers, resistive plate chambers (RPC) are used in the barrel region ($|\eta| < 1.05$) while in the end-cap region ($1.05 < |\eta| < 2.4$) thin gap chambers (TGC) are installed. These chambers measure the track position in the η and in the ϕ plane with a spatial resolution of $\leq 10\,\mathrm{mm}$. Designed to provide track information only a few tens of nanoseconds after the muon has transversed, these chambers allow for bunch-crossing identification with a probability of $\geq 99\%$.

The momentum measurement is performed by the precision chambers, measuring the coordinate of the track in the bending (η) plane with an high position resolution of $\leq 40\,\mu m$. Except in the very forward region of the innermost end-cap layer ($2.0 < |\eta| < 2.7$), the precision measurement is provided by monitored drift tube chambers (MDT). These chambers consist of three to eight layers of single drift tubes filled with Ar/CO_2 gas mixture and operate under a $3\,$bar gas presure and high voltage of about $3000\,\mathrm{V}$. With the single tube resolution of $80\,\mu\mathrm{m}$, one MDT chamber achieves a track-point resolution of $35\,\mu\mathrm{m}$ in the bending plane.

At large pseudorapidities ($2.0 < |\eta| < 2.7$) cathode strip chambers (CSC) are used in the innermost tracking disc. In contrast to the MDT chambers, the CSC chambers are multiwire proportional chambers with cathode strips in orthogonal directions which allow for a simultaneous measurement of both track coordinates with an increased time resolution. This technology in addition to the higher granularity compared to the MDT chambers meets

the demands of the higher muon-track density and background rate in the forward region. The resolution of one CSC chamber is $40\,\mu\mathrm{m}$ in the bending plane.
To achieve the desired stand-alone momentum resolution mentioned above the sagitta of the muon tracks has to be measured with a resolution of $\leq 50\,\mu\mathrm{m}$. Therefore the positions of the MDT wires and CSC strips must be known to better than $30\,\mu\mathrm{m}$. For this purpose two alignment procedures (optical and track based) are applied.
Each MDT chamber is equipped with an optical inplane alignment system that is monitoring internal deformations of the chambers. Furthermore the relative position of every MDT and CSC chamber with respect to its neighbours is also optically monitored. Nevertheless the optical alignment system cannot determine the absolute postion of the chambers and is insufficient to achieve the aimed alignment accuracy. To manage a global postioning and to achieve the required sagitta accuracy, track-based alignment algorithms must be used in combination with the optical system.

2.2.6 The Trigger System

The LHC will provide an extremely high event rate of approximately 1 GHz. This rate has to be reduced by a factor of $\sim 5 \cdot 10^6$ down to a technically feasible rate for data taking of ~ 200 Hz. Since the physics processes of interest are very rare, one must ensure that only as few of such events as possible are thrown away. These demands define the challenge of every trigger system and in particular for experiments at the LHC.

The ATLAS trigger system is staged in three levels:

- The level-1 trigger (L1) uses the information from the trigger chambers of the muon spectrometer and the calorimeters. Its task is to select events with high-p_T leptons, photons and jets or events with large missing transverse energy and large total transverse energy. If a set of thresholds for these objets is exceeded the event is ranked as interesting event. In this case not the whole detector information but the so-called regions of interest (RoI) are passed to the next trigger level. The L1 trigger reduces the event rate from 1 GHz to a maximum of 75 kHz.

- The second level trigger (L2) receives the RoIs defined by the L1 trigger and searches again for criteria quoted above. As opposed to L1 where only a low granularity information is used, L2 is using the information of all detector components in the RoIs. The L2 trigger reduces the event rate to 3.5 kHz.

- The third level trigger or the so-called event filter (EF) forms together with L2 the high-level trigger (HLT). The EF uses fully-built events and applies offline analysis procedures to finally select events for data storage. The EF reduces the event rate to ~ 200 Hz and performs a full reconstruction of the event on dedicated computer farms. Thereby every single event is reconstructed on one processor within about 4 seconds.

After passing all trigger levels the events are stored, further processed and copied to computing centres all over the world. From there they can be accessed and analysed by users via the worldwide computing grid. At design operation approximately 15000 terabyte of data have to be stored per year.

Chapter 3

The Standard Model and its Minimal Supersymmetric Extension

In this chapter, an overview of the standard theory describing the elementary particles and their interaction is presented (Section 3.1). The studies in the following chapters concern seaches for neutral Higgs bosons predicted by the minimal supersymmetric extension of the standard model (MSSM). Therefore the MSSM will be introduced in Section 3.2. After the introduction of the two models, the last part of this chapter deals with the production (Section 3.3) of MSSM Higgs bosons at the LHC and their decay modes (Section 3.4).

3.1 The Standard Model of Particle Physics

The standard model (SM) of particle physics is a highly successful theory describing our current understanding of the fundamental particles and their interactions. The SM is a spontaneously broken local gauge theory based on the symmetry group $SU(3)_C \times SU(2)_L \times U(1)_Y$ which is a direct product of the three simplest special unitary transformation groups. These Lie groups fully characterize the fundamental interactions, the strong, the weak and the electromagnetic force.

The standard model contains the following three different classes of particles (see also Table 3.1 and Figure 3.3):

The **fermions** with spin $1/2$ are the fundamental constituents of matter. They are classified as leptons and quarks which appear in three generations with increasing mass. The leptons take part in the weak and (if they are charged) electromagnetic interactions and the quarks in addition in the strong interaction.

Another class of particles in the SM are the **vector bosons** with spin 1. The vector bosons of the gauge fields correspond to the generators of the gauge symmetry groups and are mediating the fundamental forces: the photon is the carrier of the electromagnetic force, the $W^{\pm}$ and Z bosons mediate the weak interaction and the eight gluons are responsible for the strong interaction.

The SM is completed by one scalar boson with spin 0, the **Higgs boson**. It is the only particle in the SM that has not been discovered yet. The Higgs boson is related to the spontaneous breaking of the electroweak gauge symmetry and the origin of the fermion and boson masses in the SM via the Higgs mechanism.

In the following, the SM and the Higgs mechanism are discussed in more detail. Reference [3] provides further information on this topic.

3.1.1 The Standard Model

The SM provides a unified framework to describe the fundamental forces in nature except the gravitation. It contains quantum chromo-dynamics (QCD) [4] and the electroweak gauge theory proposed by Glashow, Salam and Weinberg [5,6,7] which unifies the electromagnetic and weak interaction. The SM is a renormalizable quantum field theory in which the fundamental matter and gauge fields are representations of the gauge symmetries of the three interactions.

The Matter Fields

The matter fields in the SM comprise three generations of left-handed and right-handed fermions, quarks and leptons, $f_{L,R} = \frac{1}{2}(1 \mp \gamma_5)f$. The left-handed fermions carry third components of the weak isospin of $I_f^{3,L} = \pm\frac{1}{2}$ and are assigned to weak isospin doublets

$$\begin{aligned} L_1 &= \begin{pmatrix} \nu_e \\ e^- \end{pmatrix}_L, \; L_2 = \begin{pmatrix} \nu_\mu \\ \mu^- \end{pmatrix}_L, \; L_3 = \begin{pmatrix} \nu_\tau \\ \tau^- \end{pmatrix}_L; \\ Q_1 &= \begin{pmatrix} u \\ d \end{pmatrix}_L, \; Q_2 = \begin{pmatrix} c \\ s \end{pmatrix}_L, \; Q_3 = \begin{pmatrix} t \\ b \end{pmatrix}_L; \end{aligned} \tag{3.1}$$

where $L_{1,\ldots,3}$ represent the lepton and $Q_{1,\ldots,3}$ the quark generations. The right-handed fermions are weak isosinglets with $I_f^{3,R} = 0$ under $SU(2)_L$ and do not interact weakly:

$$\begin{aligned} e_{R_1} &= e_R^-, \; e_{R_2} = \mu_R^-, \; e_{R_3} = \tau_R^-, \\ u_{R_1} &= u_R, \; u_{R_2} = c_R, \; u_{R_3} = t_R, \\ d_{R_1} &= d_R, \; d_{R_2} = s_R, \; d_{R_3} = b_R. \end{aligned} \tag{3.2}$$

Since the neutrinos are massless in the SM, they have no right-handed isosinglet components and the SM only contains left-handed neutrinos. Besides the weak isospin quantum numbers, the left- and right-handed fermions carry weak hypercharge which is defined by

$$Y_f = 2Q_f - 2I_f^3 \tag{3.3}$$

with the electric charge quantum number Q_f.

In addition, the quarks are assigned to colour triplets under the $SU(3)_C$ symmetry group.

$$q = \begin{pmatrix} q_r \\ q_g \\ q_b \end{pmatrix} \quad \text{with} \quad q = (u, d, s, c, t, b)\,. \tag{3.4}$$

The leptons are $SU(3)_C$ singlets without colour charge since they do not take part in strong interactions. Color confinement forbids free coloured states. All coloured particles (i.e. quarks and gluons) are bound in colourless singlets (baryons and mesons), like for example the charged pion:

$$\pi^+ = \frac{1}{\sqrt{3}}\left(u_r\bar{d}_{\bar{r}} + u_g\bar{d}_{\bar{g}} + u_b\bar{d}_{\bar{b}}\right). \tag{3.5}$$

The Gauge Fields

The gauge fields correspond to the spin-1 bosons mediating the fundamental interactions. For the electroweak interaction there is the B_μ field corresponding to the generator of the weak hypercharge of the $U(1)_Y$ symmetry group. In addition, there are the fields $W_\mu^{1,2,3}$

which correspond to the generators T^a ($a = 1, 2, 3$) of the symmetry group $SU(2)_L$. These generators obey the relations

$$\begin{aligned} [T^a, T^b] &= i\epsilon^{abc}T_c \\ T^a &= \frac{1}{2}\tau^a \\ [Y, Y] &= 0 \end{aligned} \tag{3.6}$$

where τ^a are the Pauli matrices and ϵ^{abc} is the antisymmetric tensor.
The strong interaction is mediated by an octet of gluon fields $G_\mu^{1,\cdots,8}$ which correspond to the eight generators $T_{SU(3)}^{1,\ldots,8}$ of the $SU(3)_C$ symmetry group. These generators fulfil the relations

$$\begin{aligned} [T^a_{SU(3)}, T^b_{SU(3)}] &= if^{abc}T_{c\,SU(3)} \\ T^a_{SU(3)} &= \frac{1}{2}\lambda^a \end{aligned} \tag{3.7}$$

where f^{abc} are the structure constants of $SU(3)$ and $\lambda^{1,\cdots,8}$ are the Gell-Mann matrices.

The gauge field strengths are given by:

$$\begin{aligned} G^a_{\mu\nu} &= \partial_\mu G^a_\nu - \partial_\nu G^a_\mu + g_3 f^{abc} G^b_\mu G^c_\nu, \\ W^a_{\mu\nu} &= \partial_\mu W^a_\nu - \partial_\nu W^a_\mu + g_2 \epsilon^{abc} W^b_\mu W^c_\nu, \\ B_{\mu\nu} &= \partial_\mu B_\nu - \partial_\nu B_\mu, \end{aligned} \tag{3.8}$$

where g_1, g_2 and g_3 are the coupling constants of $U(1)_Y$, $SU(2)_L$ and $SU(3)_C$.
In equation 3.8 one can see the non-abelian character of the $SU(2)$ and $SU(3)$ groups which leads to self-interactions between their gauge fields.

Matter-Gauge Field Coupling

The matter fields ψ are minimally coupled to the gauge fields through the gauge covariant derivate D_μ which is defined as

$$D_\mu\psi = \left(\partial_\mu - ig_3\frac{\lambda_a}{2}G^a_\mu - ig_2\frac{\tau_a}{2}W^a_\mu P_L - ig_1\frac{Y_f}{2}B_\mu\right)\psi, \tag{3.9}$$

with the operator $P_{L,R}$ projecting the chiral fields ψ in their left- and right-handed components $\psi_{L,R} = P_{L,R}\psi$.
The Lagrangian of the SM, invariant under $SU(3)_C \times SU(2)_L \times U(1)_Y$ gauge transformations before electroweak symmetry breaking, is given by:

$$\begin{aligned} \mathcal{L}_{SM} = &-\frac{1}{4}G^a_{\mu\nu}G^{\mu\nu}_a - \frac{1}{4}W^a_{\mu\nu}W^{\mu\nu}_a - \frac{1}{4}B_{\mu\nu}B^{\mu\nu} + \\ &+ \bar{L}_i iD_\mu\gamma^\mu L_i + \bar{e}_{R_i} iD_\mu\gamma^\mu e_{R_i} + \bar{Q}_i iD_\mu\gamma^\mu Q_i + \\ &+ \bar{u}_{R_i} iD_\mu\gamma^\mu u_{R_i} + \bar{d}_{R_i} iD_\mu\gamma^\mu d_{R_i}. \end{aligned} \tag{3.10}$$

By inserting equation 3.9 in the equation 3.10 one obtaining

$$\begin{aligned} \mathcal{L}_{SM} &= \mathcal{L}_{free} + \mathcal{L}_{interaction} \\ &= \mathcal{L}_{free} + \mathcal{L}_{GSW} + \mathcal{L}_{QCD} \end{aligned} \tag{3.11}$$

where the free Lagrangian contains the free gauge and matter fields while $\mathcal{L}_{GSW}$ and $\mathcal{L}_{QCD}$ contain the matter-gauge field couplings of the electroweak and strong interaction, respectively.

$\mathcal{L}_{GSW}$ can be expressed in terms of flavour-changing and flavour-conserving weak interactions called the charged current[1] and the neutral current interactions $\mathcal{L}_{CC}$ and $\mathcal{L}_{NC}$, respectively:

$$\mathcal{L}_{GSW} = \mathcal{L}_{NC} + \mathcal{L}_{CC} = -g_1 j_Y^\mu B_\mu - g_2 j_I^{\mu,3} W_\mu^3 - \frac{g_2}{\sqrt{2}} \left(j_I^{\mu,-} W_\mu^+ + j_I^{\mu,+} W_\mu^- \right) \quad (3.12)$$

with

$$\begin{aligned} j_Y^\mu &= -\bar{\psi}_f \frac{Y_f}{2} \gamma^\mu \psi_f , \\ j_I^{\mu,a} &= -\bar{\psi}_L \frac{\tau_a}{2} \gamma^\mu \psi_L \quad (a = 1,2,3), \\ j_I^{\mu,\pm} &= \frac{1}{\sqrt{2}} \left(j_I^{\mu,1} \pm j_I^{\mu,2} \right) . \end{aligned} \quad (3.13)$$

This formulation already contains the physical gauge bosons $W^\pm$ of the weak charged current interaction defined by

$$W^\pm = \frac{1}{\sqrt{2}} \left(W_\mu^1 \mp W_\mu^2 \right) . \quad (3.14)$$

The electromagnetic field A_μ and the weak neutral current force field Z_μ^0 are generated by a rotation of the gauge fields B_μ and W_μ^3

$$\begin{pmatrix} A_\mu \\ Z_\mu^0 \end{pmatrix} = \begin{pmatrix} \cos\theta_W & \sin\theta_W \\ -\sin\theta_W & \cos\theta_W \end{pmatrix} \begin{pmatrix} B_\mu \\ W_\mu^3 \end{pmatrix} \quad (3.15)$$

with the Weinberg angle θ_W which is chosen such that the coupling of the neutrino to the photon field is zero:

$$\cos\theta_W = \frac{g_2}{\sqrt{g_2^2 + g_1^2}}, \quad \sin\theta_W = \frac{g_1}{\sqrt{g_2^2 + g_1^2}}, \quad (3.16)$$

such that

$$\begin{aligned} Z_\mu^0 &= \frac{g_2 W_\mu^3 - g_1 B_\mu}{\sqrt{g_2^2 + g_1^2}}, \\ A_\mu &= \frac{g_1 W_\mu^3 + g_2 B_\mu}{\sqrt{g_2^2 + g_1^2}}. \end{aligned} \quad (3.17)$$

The Lagrangian in equation 3.10 does not contain any mass terms for fermions and bosons. This is in contradiction to experimental observations of finite fermion and weak gauge boson masses and leads to the question of how the masses in the SM can be generated without the loss of the gauge invariance.

The mass terms for the strong interaction are not problematic. On the one hand the gluons are massless particles and on the other hand Dirac mass terms in the form $-m_q \bar{\psi}\psi$ can be implemented in the $SU(3)_C$ Lagrangian for quarks without breaking the $SU(3)$ gauge invariance.

This is different for the electroweak interaction. Here, the Dirac mass terms of the form

$$\mathcal{L}_{mass} = -m\bar{\psi}\psi = -m(\bar{\psi}_L \psi_R + \bar{\psi}_R \psi_L) \quad (3.18)$$

---

[1] The term current in this sense is of the from $\bar{\psi}\gamma^\mu\psi$. For example the electromagnetic current of QED is given by $j^\mu_{QED} = \sum_f Q_f \bar{\psi}_f \gamma^\mu \psi_f$. With this definition the interactions in the SM can be described as a current-gauge field coupling.

violate the global $SU(2)_L$ gauge invariance. Because due to parity violation in the weak interaction the left- and right-handed field components transform differently under $SU(2)_L$. In addition, Klein-Gordon mass terms ($-\frac{1}{2}M_W^2 W_\mu^+ W^{-,\mu}$ and $-\frac{1}{2}M_Z^2 Z_\mu^0 Z^{0,\mu}$) for the weak gauge bosons violate the local $SU(2)_L \times U(1)_Y$ gauge invariance.

Since the gauge invariance is necessary for the renormalizability of the SM, an alternative way has to be found to generate gauge boson and fermion masses in the SM without violating the $SU(2)_L \times U(1)_Y$ symmetry of the Lagrangian. A solution has been proposed by P.W. Higgs, F. Englert, R. Brout, G.S. Guralnik, C.R. Hagen and T.W.B. Kibble [8,9,10,11,12]. The so-called Higgs mechanism is introduced in the following section.

3.1.2 The Higgs Mechanism

The Higgs mechanism consists of the addition of a scalar field to the standard model. Since the purpose is to create masses for the weak gauge bosons, at least three degrees of freedom for the scalar field are necessary. The simplest way to achieve this is the introduction of a complex scalar field with four degrees of freedom

$$\Phi = \begin{pmatrix} \phi^+ \\ \phi^0 \end{pmatrix} = \frac{1}{\sqrt{2}} \begin{pmatrix} \phi_3 + i\phi_4 \\ \phi_1 + i\phi_2 \end{pmatrix}, \tag{3.19}$$

which is a $SU(2)_L$ doublet. Its components have hypercharge $Y_\phi = +1$.

Since only the electroweak gauge symmetry is broken, we consider only the electroweak part of the Lagrangian in equation 3.10.

$$\mathcal{L}_{el.\,weak} = -\frac{1}{4} W_{\mu\nu}^a W_a^{\mu\nu} - \frac{1}{4} B_{\mu\nu} B^{\mu\nu} + \bar{L} i D_\mu \gamma^\mu L + \bar{e}_R i D_\mu \gamma^\mu e_R + ... \tag{3.20}$$

with the covariant derivate

$$D_\mu \Phi = \left(\partial_\mu - i g_2 \frac{\tau_a}{2} W_\mu^a - i g_1 \frac{Y_\Phi}{2} B_\mu \right) \Phi. \tag{3.21}$$

The scalar field contributes to the Lagrangian with

$$\mathcal{L}_S = (D^\mu \Phi)^\dagger (D_\mu \Phi) - V = (D^\mu \Phi)^\dagger (D_\mu \Phi) - \mu^2 \Phi^\dagger \Phi - \lambda (\Phi^\dagger \Phi)^2 \tag{3.22}$$

where V is the Higgs potential with the mass parameter μ and the self coupling parameter λ of the scalar field Φ.

For $\mu^2 < 0$ the scalar field developes an infinite number of ground states with field strength different from zero,

$$\Phi_0^2 = -\frac{\mu^2}{2\lambda} \neq 0. \tag{3.23}$$

By choosing one particular ground state, for example[2]

$$\langle \Phi \rangle_0 = \begin{pmatrix} 0 \\ \frac{v}{\sqrt{2}} \end{pmatrix} \tag{3.24}$$

with the vacuum expectation value $v = \sqrt{\frac{-\mu^2}{2\lambda}}$, the local $SU(2)_L \times U(1)_Y$ symmetry is spontaneously broken

Field exitations from this ground state can then be parametrized as

$$\Phi(x) = \exp\left[i \frac{\zeta_a(x) \tau^a}{v} \right] \begin{pmatrix} 0 \\ \frac{1}{\sqrt{2}}(v + H(x)) \end{pmatrix} \tag{3.25}$$

---

[2] Since the electromagentic $U(1)_Q$ symmetry should remain unbroken, the vacuum expectation value of the charged component is choosen to be zero, $\langle \phi^+ \rangle_0 = 0$.

which, after transformation to the unitary gauge, become

$$\Phi(x) \rightarrow \exp\left[-i\frac{\zeta_a(x)\tau^a}{v}\right]\Phi(x) = \frac{1}{\sqrt{2}}\begin{pmatrix} 0 \\ v + H(x) \end{pmatrix} \tag{3.26}$$

with massless unphysical excitations $\zeta_a(x)$ ($a = 1, 2, 3$) and a physical massive Higgs field $H(x)$.

After insertion of the equations 3.21 and 3.26 in equation 3.22, the kinematic term of the scalar Lagrangian is given by

$$\begin{aligned} T =& \frac{1}{2}\partial^\mu H \partial_\mu H + \frac{g^2 v^2}{8}(W_\mu^+ W^{\mu,+} + W_\mu^- W^{\mu,-}) \\ &+ \frac{g^2 v^2}{8\cos^2\theta_W} Z_\mu^0 Z^{\mu,0} \\ &+ \frac{g^2}{4}(H^2 + 2vH)\left(W_\mu^+ W^{\mu,-} + \frac{1}{2\cos^2\theta_W} Z_\mu^0 Z^{\mu,0}\right), \end{aligned} \tag{3.27}$$

where the expressions in equations 3.14 and 3.17 for the physical gauge fields are already implemented. Using the same procedure as for the kinematic term, the potential of the scalar field can be written as

$$\begin{aligned} V &= \mu^2 \Phi^\dagger \Phi + \lambda(\Phi^\dagger\Phi)^2 \\ &= -\mu^2 H^2 + \lambda v H^3 + \frac{\lambda}{4}H^4. \end{aligned} \tag{3.28}$$

Finally the complete Lagrangian of the scalar field Φ is given by

$$\begin{aligned} \mathcal{L}_S =& \frac{1}{2}\left(\partial^\mu H \partial_\mu H - M_H^2 H^2\right) - \lambda v H^3 - \frac{\lambda}{4}H^4 \\ &+ \frac{g^2}{4}(H^2 + 2vH)\left(W_\mu^+ W^{\mu,-} + \frac{1}{2\cos^2\theta_W} Z_\mu^0 Z^{\mu,0}\right) \\ &+ \frac{1}{2}M_W^2\left(W_\mu^+ W^{\mu,+} + W_\mu^- W^{\mu,-}\right) + \frac{1}{2}M_Z^2 Z_\mu^2 Z^{\mu,0}. \end{aligned} \tag{3.29}$$

This expression contains the mass terms for the gauge bosons with $M_W = {}^{gv}/_2$ and $M_Z = {}^{M_W}/_{\cos\theta_W}$ and for the Higgs boson with mass

$$M_H = \sqrt{2\lambda v^2}. \tag{3.30}$$

The parameters λ and v, and thus the Higgs mass, are free parameters of the theory which have to be determined by experiment.

The fermion masses are generated by introducing Yukawa couplings between the fermions and the same scalar field, Φ in a $SU(2)_L \times U(1)_Y$ invariant Lagrangian which has the following form for every fermion generation:

$$\mathcal{L}_f = -\lambda_e \bar{L}\Phi e_R - \lambda_d \bar{Q}\Phi d_R - \lambda_u \bar{Q}\tilde{\Phi} u_R + h.c. \tag{3.31}$$

with the conjugate isodoublet $\tilde{\Phi} = i\tau_2\Phi^*$ with hypercharge $Y = -1$.
After the same transformations as for the gauge bosons above one obtains a mass term for every fermion f given by

$$m_f = \frac{\lambda_f v}{\sqrt{2}}. \tag{3.32}$$

In summary, the masses for fermions and bosons have been generated by introducing one additional complex scalar field Φ with negative squared mass parameter , $\mu^2 < 0$. The complete Lagrangian of the standard model

$$\mathcal{L}_{SM} = \mathcal{L}_{SU(3)} + \mathcal{L}_{SU(2)\times U(1)} + \mathcal{L}_S + \mathcal{L}_f \tag{3.33}$$

is still $SU(3)_C \times SU(2)_L \times U(1)_Y$ gauge invariant. By choosing one particular ground state of the Higgs field, the electroweak gauge symmetry is spontaneously broken while the electromagnetic symmetry is preserved which is exactly what we observe in nature.

$$SU(2)_L \times U(1)_Y \xrightarrow{SSB} U(1)_Q. \tag{3.34}$$

3.1.3 Tests of the SM

The SM has been tested in high-precision measurements at LEP[3], SLAC[4], Tevatron and elsewhere over the last decades. The results are all in general in excellent agreement with the theoretical predictions. Thus, these tests performed with per mille level accuracy have established the SM as an effective describtion of the strong and electroweak interactions at present energies. The only particle that remaines undiscovered is the Higgs boson. Up to now, the experimental searches at LEP and Tevatron provide only constraints on its mass [13], with $m_H > 114.4\,\text{GeV}$ at a confidence level of $95\,\%$ from direct searches at LEP and an upper limit from indirect precision measurements of $m_H < 186\,\text{GeV}$.

Particle	Mass	Spin	Weak Isospin	Hypercharge	Colour
ν_e	$< 2.2\,\text{eV}$	$\frac{1}{2}$	$\left(\frac{1}{2}, +\frac{1}{2}\right)$	-1	0
e	$0.511\,\text{MeV}$	$\frac{1}{2}$	$\left(\frac{1}{2}, -\frac{1}{2}\right)$	-1	0
ν_μ	$< 0.19\,\text{MeV}$	$\frac{1}{2}$	$\left(\frac{1}{2}, +\frac{1}{2}\right)$	-1	0
μ	$106\,\text{MeV}$	$\frac{1}{2}$	$\left(\frac{1}{2}, -\frac{1}{2}\right)$	-1	0
ν_τ	$< 18.2\,\text{MeV}$	$\frac{1}{2}$	$\left(\frac{1}{2}, +\frac{1}{2}\right)$	-1	0
τ	$1.78\,\text{GeV}$	$\frac{1}{2}$	$\left(\frac{1}{2}, -\frac{1}{2}\right)$	-1	0
u	$\sim 7\,\text{MeV}$	$\frac{1}{2}$	$\left(\frac{1}{2}, +\frac{1}{2}\right)$	$+\frac{1}{3}$	r, g, b
d	$\sim 5\,\text{MeV}$	$\frac{1}{2}$	$\left(\frac{1}{2}, -\frac{1}{2}\right)$	$+\frac{1}{3}$	r, g, b
c	$\sim 1.4\,\text{GeV}$	$\frac{1}{2}$	$\left(\frac{1}{2}, +\frac{1}{2}\right)$	$+\frac{1}{3}$	r, g, b
s	$\sim 0.104\,\text{GeV}$	$\frac{1}{2}$	$\left(\frac{1}{2}, -\frac{1}{2}\right)$	$+\frac{1}{3}$	r, g, b
t	$171 \pm 2\,\text{GeV}$	$\frac{1}{2}$	$\left(\frac{1}{2}, +\frac{1}{2}\right)$	$+\frac{1}{3}$	r, g, b
b	$\sim 4.2\,\text{GeV}$	$\frac{1}{2}$	$\left(\frac{1}{2}, -\frac{1}{2}\right)$	$+\frac{1}{3}$	r, g, b
γ	0	1	$(0, 0)$	0	0
Z^0	$91\,\text{GeV}$	1	$(1, 0)$	0	0
$W^\pm$	$80\,\text{GeV}$	1	$(1, \pm 1)$	0	0
g	0	1	$(0, 0)$	0	$g\bar{r}, r\bar{b}, b\bar{g}$ $r\bar{g}, b\bar{r}, g\bar{b}$ $r\bar{g}, b\bar{r}, g\bar{b}$ $r\bar{r} - g\bar{g}$ $r\bar{r} + g\bar{g} - 2b\bar{b}$
H	$> 114.4\,\text{GeV}$	0	$\left(\frac{1}{2}, -\frac{1}{2}\right)$	1	0

Table 3.1: Particle content of the standard model, including their quantum numbers.

---

[3] Large Electron Positron Collider

[4] Standford Linear Accelerator Center

3.2 The Minimal Supersymmetric Extension of the Standard Model

In this section the minimal supersymmetric standard model (MSSM) is introduced. After a brief discussion of the principles of supersymmetry. A detailed describtion of this model can be found for example in reference [14].

3.2.1 The Concept of Supersymmetry

As described in the previous section, the SM has passed extremely precise tests. Still, it is widely believed that the SM is an effective theory which is only valid at the presently accessible energies, since there are several open questions the SM cannot answer. These questions point to new physics beyond the SM and therefore a more fundamental theory.

3.2.1.1 Open Questions in the Standard Model

The following list mentiones a few selected problems for which the SM has no satisfactory answers:

- The SM cannot describe the fourth fundamental force in nature: the gravitation.

- In its simplest form it does not include the masses of the neutrinos which are proven to be different from zero by the discovery of neutrino oscillations. Even if neutrino masses are added like for the other fermions, it is not explained why neutrino masses are so much smaller than the other fermion masses.

- The SM gauge theory is based on the direct product of the three simplest special unitary groups which is not a true unification of the three interactions. Therefore one expects a more fundamental Grand Unified Theory[5] (GUT) which describes the forces by a single gauge group, like $SU(5)$ or $SO(10)$, which contains the SM gauge symmetries as subgroups. However, the precision measurements at LEP and elsewhere show, that the values for the SM gauge coupling constants fail to meet at high energies if only the known SM particles are taken into account (see Fig. 3.1).

- Astrophysical observations have shown that there should be a large contribution of cold dark matter in the universe. This non-baryonic matter has to consist of particles which are stable, massive, electrically neutral and only weakly interacting. The SM does not include any particle candidate fulfilling these requirements.

- The fine-tuning problem: In the standard model, radiative corrections to M_H^2 lead to quadratic divergences in the cut-off scale Λ beyond which the theory ceases to be valid. At higher energies new physics should appear. For consistency reasons, the Higgs mass is expected be in the range near the electroweak symmetry breaking scale ($v \sim 250\,\text{GeV}$) and it has to be at least smaller than $1\,\text{TeV}$ to guarantee unitarity of the theory. If one now choses Λ to be at the GUT scale, the radiative corrections ΔM_H^2 lead to a Higgs mass of the order of the GUT scale. To guarantee $M_H < 1\,\text{TeV}$ one has to add counterterms to ΔM_H^2 in the Lagrangian which have to be fine-tuned with a unnatural high accuracy of $\mathcal{O}(10^{-30})$.

  Strongly related is the hierarchy problem which asks for an explanation why $\Lambda \gg M_Z$ or why the weak force is 10^{32} times stronger than gravity.

---

[5] The symmetry group G of a Grand Unified Theory has to contain the symmetry group of the standard model $G \supset SU(3)_C \times SU(2)_L \times U(1)_Y$. The standard model is then regarded as an effective theory after another spontaneous symmetry breaking at the GUT scale, above which all couplings are equal: $GUT \xrightarrow{M_{GUT}} SU(3)_C \times SU(2)_L \times U(1)_Y \xrightarrow{M_{el.weak}} SU(3)_C \times U(1)_Q$.

3.2.1.2 Supersymmetry as a Possible Solution

Many extensions of the standard model involve supersymmetry (SUSY), because it could solve several shortcomings of the SM in an attractive way. Some of these aspects are mentioned at the end of this section after briefly introducing the basics of SUSY.
SUSY models introduce a new symmetry between bosons and fermions. The generator $\mathcal{Q}$ transforms the two classes of particles into each other. The fermions are transformed into their bosonic superpartners (sfermions), the bosons into their fermionic superpartners (gauginos) with the same quantum numbers (except their spin):

$$\begin{aligned} \mathcal{Q}|\text{Fermion}\rangle &= |\text{Boson}\rangle, \\ \mathcal{Q}|\text{Boson}\rangle &= |\text{Fermion}\rangle. \end{aligned} \tag{3.35}$$

The supersymmetric partner particles are usually called SUSY particles. If the symmetry is exact und unbroken, the bosonic and fermionic fields have the same masses.
In nature, supersymmetry has to be broken because no partners of the SM particles with equal masses have been observed. This breaking of supersymmetry has to be soft enough such that the superpartners are not too heavy. Otherwise the hierarchy problem of the SM would re-appear (see below).
Details of dynamical SUSY breaking mechanisms are at present still unknown. One can only introduce effective SUSY breaking terms into a low-energy SUSY theory which leads to many additional free parameters and a strong model dependence of the predictions. One of the best studied SUSY models is the minimal supersymmetric standard model, (MSSM) which is explained in the rest of this chapter. Before concentrating on the MSSM, the solution to selected SM problems by SUSY is briefly discussed:

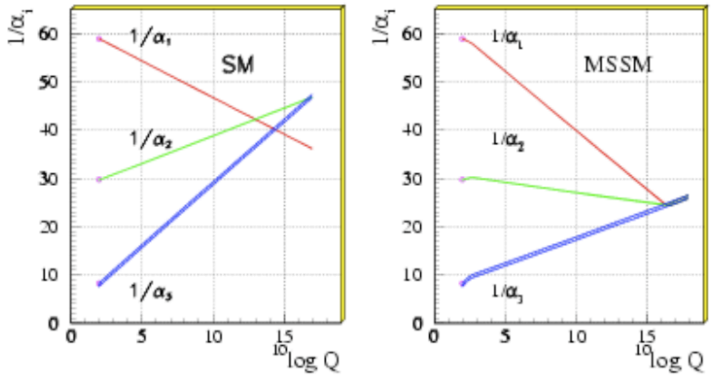

Figure 3.1: Running of the gauge coupling constants of the electromagnetic (α_1), weak (α_2) and strong interaction (α_3) in the standard model (left) and MSSM (right): While the values of the couplings fail to meet at a common point for the SM, they unifiy in MSSM at $\sim 2 \cdot 10^{16}$ GeV which marks the GUT energy scale.

- If SUSY is introduced as a local symmetry, it incorporates gravity and appears automatically in Superstring theories.

- The new SUSY particle spectrum modifies the running of the SM gauge coupling constants such that they meet at the GUT energy scale (see Fig. 3.1) above which the interactions are unified.

- The additional requirement of R-parity conservation results in a stable lightest SUSY particle. Such a particle is a promising candidate for cold dark matter since it is expected to be massive, weakly interacting and electrically neutral.

- Additional sfermion($\tilde{f}$)-loop corrections in SUSY extensions to the SM cancel the divergencies of the radiative corrections to the Higgs mass ΔM_H^2. This leads to a Higgs mass $M_H \lesssim 135\,\text{GeV}$ without unnatural fine-tuning as in the SM (see Fig. 3.2).

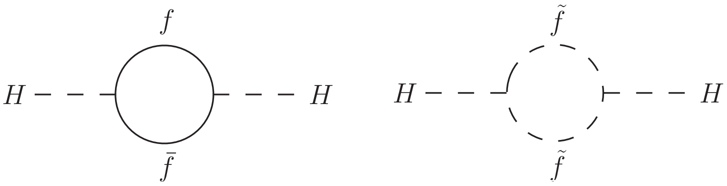

Figure 3.2: Contributions of fermionic and scalar loops to the Higgs boson mass: in the SM the fermion loops (left) lead to divergencies in the radiative corrections $\Delta M_H^2 \sim \Lambda^2$ which are compensated by scalar loops (right) in SUSY extensions of the SM.

3.2.2 The Minimal Supersymmetric Standard Model

The minimal supersymmetric extension of the standard model is based on the **minimal gauge symmetry group** $SU(3)_C \times SU(2)_L \times U(1)_Y$ of the standard model. The spin-1 gauge bosons of the SM obtain their spin-$1/2$ superpartners, the gauginos, i.e. the bino $\tilde{B}$, three winos $\tilde{W}_{1,\ldots,3}$ and eight gluinos $\tilde{G}_{1,\ldots,8}$ which together form vector supermultiplets (see Table 3.2).

Name	gauge boson	gaugino	$SU(3)_C$,$SU(2)_L$,$U(1)_Y$
gluon, gluino	$G^\mu_{1,\ldots,8}$	$\tilde{G}_{1,\ldots,8}$	($\mathbf{8}$,$\mathbf{1}$,0)
W bosons, winos	$W^\mu_{1,\ldots,3}$	$\tilde{W}_{1,\ldots,3}$	($\mathbf{1}$,$\mathbf{3}$,0)
B boson, bino	B^μ	$\tilde{B}$	($\mathbf{1}$,$\mathbf{1}$,0)

Table 3.2: MSSM vector supermultiplets and their quantum numbers.

Similar to the bosons also the SM fermions obtain their superpartners, the spin-0 sfermions $\tilde{f}$. The fermion-sfermion pairs form chiral supermultiplets (see Table 3.3). Furthermore, two scalar Higgs doublets under $SU(2)_L$, H_1 and H_2, are needed to cancel chiral anomalies (see subsection 3.2.3). They have spin-$^1/_2$ superpartners $\tilde{H}_1$ and $\tilde{H}_2$ to form Higgs supermuliplets. All supermultiplets together form the **minimal particle content** of the MSSM. Tables 3.2 and 3.3 show the charge eigenstates of the MSSM particles. The charge eigenstates with the same charge quantum numbers can mix to form mass eigenstates which are measured in the experiments (compare Table 3.4):

- The neutral and the charged higgsino fields mix with the neutral and charged winos, respectively and with the bino to give two chargino $\chi^\pm_{1,2}$ and four neutralino $\chi^0_{1,2,3,4}$ mass eigenstates.

- The mass eigenstates of the sfermions[6] $\tilde{f}_1$ and $\tilde{f}_2$ originate from the mixing of the charge eigenstates $\tilde{f}_L$ and $\tilde{f}_R$.

- The two complex Higgs doublets result in five massive Higgs bosons after electroweak symmetry breaking: two charged bosons $H^\pm$, two neutral CP-even Higgs bosons h, H and one pseudoscalar CP-odd A boson (see section 3.2.3 for more details).

Name	fermions	sfermions	$SU(3)_C$,$SU(2)_L$,$U(1)_Y$
quarks, squarks	(u_L,d_L)	$(\tilde{u}_L,\tilde{d}_L)$	$(\mathbf{3},\mathbf{2},\frac{1}{3})$
	$\bar{u}_R$	$\tilde{\bar{u}}^*_R$	$(\bar{\mathbf{3}},\mathbf{1},-\frac{4}{3})$
	$\bar{d}_R$	$\tilde{\bar{u}}^*_R$	$(\bar{\mathbf{3}},\mathbf{1},\frac{2}{3})$
leptons, sleptons	(ν,e_L)	$(\tilde{\nu},\tilde{e}_L)$	$(\mathbf{1},\mathbf{2},-1)$
	$\bar{e}_R$	$\tilde{\bar{e}}^*_R$	$(\mathbf{1},\mathbf{1},2)$
Higgs, higgsino	H_1	$\tilde{H}_1$	$(\mathbf{1},\mathbf{2},-1)$
	H_2	$\tilde{H}_2$	$(\mathbf{1},\mathbf{2},1)$

Table 3.3: MSSM chiral and scalar supermultiplets and their quantum numbers. The symbols u, d, e represent up-type, down-type and electron-type fermions and sfermions, respectively.

Particle	mass eigenstates	charge eigenstates
neutralinos	$\tilde{\chi}^0_1$, $\tilde{\chi}^0_2$, $\tilde{\chi}^0_3$, $\tilde{\chi}^0_4$	$\tilde{B}^0$, $\tilde{W}^0$, $\tilde{H}^0_1$, $\tilde{H}^0_2$
charginos	$\tilde{\chi}^\pm_1$, $\tilde{\chi}^\pm_2$	$\tilde{W}^\pm$, $\tilde{H}^-_1$, $\tilde{H}^+_2$
squarks	$\tilde{q}_{1,2}$	$\tilde{q}_{L,R}$
sleptons	$\tilde{l}_{1,2}$	$\tilde{l}_{L,R}$
Higgs bosons	h, H, A, $H^\pm$	H^0_1, H^0_2, H^-_1, H^+_2

Table 3.4: Mass eigenstates of MSSM particles and the corresponding charge eigenstates.

The most general MSSM model contains terms which lead to the violation of baryon and lepton number conservation. In order to enforce conservation of these quantum numbers at the electroweak energy scale, a new symmetry, called **R-parity**, is introduced. It corresponds to a multiplicative quantum number defined as

$$R_p = (-1)^{2s+3B+L}, \tag{3.36}$$

where L and B are the lepton and baryon numbers and s is the spin quantum number. All SM particles have $R_p = +1$ and the supersymmetric particles $R_p = -1$. The consequence of R-parity conservation is that SUSY particles are always produced in pairs and that the lightest supersymmetric particle (LSP) is stable. In most SUSY scenarios, the LSP is the lightest of the four neutralinos which is massive, electrically neutral and only weakly interacting. With conserved R-parity, the LSP is one of the most promising candidates for cold dark matter in the Universe.

As already mentioned above, supersymmetry has to be broken since otherwise the SUSY particles would have the same masses as their SM partners. To maintain the cancelation of quadratic divergences in radiative corrections to the Higgs mass, SUSY breaking has to be such that the masses of the superpartners do not become much larger than about 1 TeV. This is achieved by the so-called **soft SUSY breaking** terms in the low-energy effective Lagrangian which parametrizes explicitely the effect of the unknown SUSY breaking meachanism:

- Mass terms for the gauginos: M_1, M_2, M_3,
- mass terms for the sfermions: $m_{\tilde{Q}_{1,...,3}}$, $m_{\tilde{L}_{1,...,3}}$, $m_{\tilde{u}_{1,...,3}}$, $m_{\tilde{d}_{1,...,3}}$, $m_{\tilde{l}_{1,...,3}}$,
- mass and bilinear coupling terms for the Higgs bosons: m_{H_1}, m_{H_2}, B and μ,
- trilinear couplings between sfermions and Higgs bosons: A^u_{ij}, A^d_{ij}, A^l_{ij}, with the fermion generation indices $i, j = 1, ..., 3$.

---

[6] Very often the 1^{st} and 2^{nd} generation sfermion masses are considered to be zero, in this case the sfermion mixing is reduced to the 3^{rd} generation.

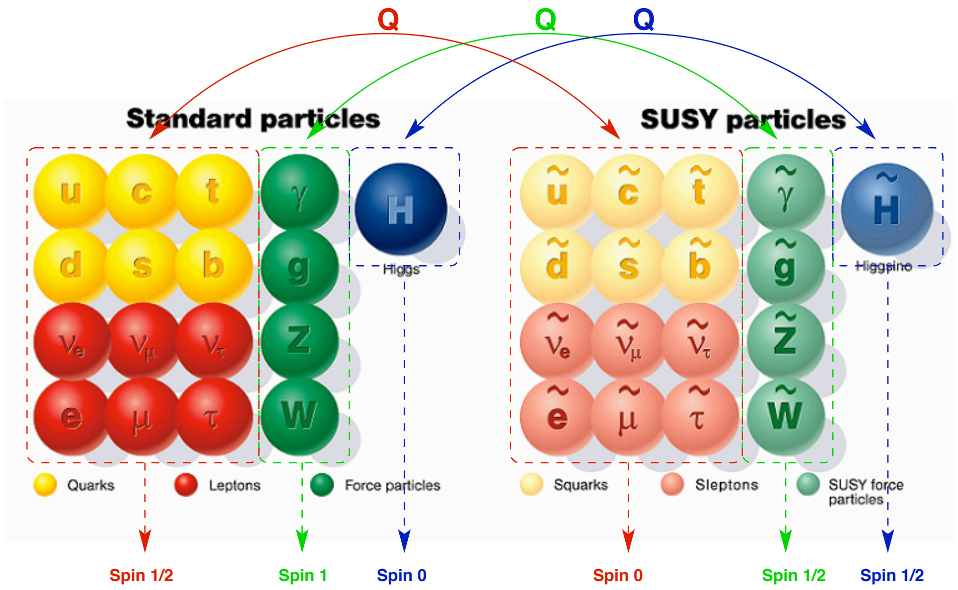

Figure 3.3: Particle content of the MSSM: every standard model particle (left) gets a superparter (right). The SUSY operator $\mathcal{Q}$ transforms these partners into each other.

To avoid the need for an unnatural fine-tuning as in the SM, an upper bound on the SUSY breaking scale M_S is imposed, which is in the case of vanishing 1^{st} and 2^{nd} generation sfermion masses given as

$$M_S = \sqrt{m_{\tilde{t}_1} m_{\tilde{t}_2}} \lesssim 2\,\mathrm{TeV}. \tag{3.37}$$

In the most general case where one allows for intergenerational mixing and complex phases of the parameters, the soft SUSY breaking terms introduce 105 free parameters in addition to the 19 free parameters of the SM. This case is referred to as the unconstrained MSSM. In order to reduce the large parameter space, several assumptions can be made:

- All soft SUSY breaking parameters are real. Therefore, no additional CP-violation except the one from the quark mixing matrix CKM of the SM is generated.
- The matrices for the sfermion masses and for the trilinear couplings are all diagonalizable. This prevents the appearance of flavour changing neutral currents (FCNCs) at the tree level which are strongly constrained experimentally.
- For the first and second sfermion generation the soft SUSY breaking masses and trilinear couplings are the same at low energy to be in compliance with tight experimental constraints from K^0-$\bar{K}^0$ mixing for example.

With these assumptions, the large number of free parameters is reduced to only 22:

- $\tan\beta$: the ratio of the vacuum expectation values of the two Higgs doublets,
- $m_{H_1}^2$, $m_{H_2}^2$: the Higgs mass parameters squared,
- M_1, M_2, M_3: the bino, wino and gluino mass parameters,
- $m_{\tilde{q}}$, $m_{\tilde{u}_R}$, $m_{\tilde{d}_R}$, $m_{\tilde{l}}$, $m_{\tilde{e}_R}$: the sfermion mass parameters equal for the first and second generation,
- A_u, A_d, A_e: the equal first/second-generation trilinear couplings,
- $m_{\tilde{Q}}$, $m_{\tilde{t}_R}$, $m_{\tilde{b}_R}$, $m_{\tilde{L}}$, $m_{\tilde{\tau}_R}$: the third generation sfermion mass parameters,

- A_t, A_b, A_τ: the third generation trilinear couplings.

The model with this set of free parameters is usually called the phenomenological MSSM (pMSSM).

The pMSSM can be further constrained if one assumes that SUSY breaking occurs in a hidden sector which communicates with the visible sector of particles only through gravitational interactions. If these interactions are flavour-blind, another set of boundary conditions for the SUSY breaking terms can be applied which assumes following unifications of parameters at the GUT scale M_{GUT}:

- Unification of the gaugino masses:

$$M_1\left(M_{GUT}\right) = M_2\left(M_{GUT}\right) = M_3\left(M_{GUT}\right) = m_{1/2}. \tag{3.38}$$

- Universal scalar masses:

$$\begin{aligned} m_{squarks}\left(M_{GUT}\right) &= m_{sleptons}\left(M_{GUT}\right) \\ &= m_{H_1}\left(M_{GUT}\right) = m_{H_2}\left(M_{GUT}\right) = m_0. \end{aligned} \tag{3.39}$$

- Universal trilinear couplings:

$$A^u_{ij}\left(M_{GUT}\right) = A^d_{ij}\left(M_{GUT}\right) = A^l_{ij}\left(M_{GUT}\right) = A_0\delta_{ij}. \tag{3.40}$$

With these further assumptions the model is called the constrained MSSM (cMSSM) or mSUGRA model.

Sfermion Mixing The mixing between left- and right-handed sfermions already mentioned above also needs to be discussed. The sfermion mass matices read

$$\mathcal{M}^2_{\tilde{f}} = \begin{pmatrix} m_f^2 + m_{LL}^2 & m_f X_f \\ m_f X_f & m_f^2 + m_{RR}^2 \end{pmatrix} \tag{3.41}$$

with the entries given by

$$\begin{aligned} m_{LL}^2 &= m^2_{\tilde{f}_L} + \left(I_f^{3L} - Q_f \sin^2\theta_W\right) M_Z^2 \cos 2\beta, \\ m_{RR}^2 &= m^2_{\tilde{f}_R} + Q_f \sin^2\theta_W M_Z^2 \cos 2\beta, \\ X_f &= A_f - \mu\left(\tan\beta\right)^{-2I_f^{3L}}. \end{aligned} \tag{3.42}$$

The mass matrices are diagonalized by the rotation of the sfermion mixing angles $\theta_{\tilde{f}}$, given by

$$\sin 2\theta_{\tilde{f}} = \frac{2m_f X_f}{m^2_{\tilde{f}_1} - m^2_{\tilde{f}_2}}. \tag{3.43}$$

The soft SUSY breaking sfermion masses are often considered to be degenerated. In this case, the sfermion mixing angles $\theta_{\tilde{f}}$ are in most of the MSSM parameter space either close to zero or to $-\pi/4$. This implies that the mixing between left- and right-handed sfermions becomes either minimal or maximal. These scenarios are therefore called the *no-mixing* and the *maximal-mixing* scenario respectively. The sfermion mixing is usually described in terms of the parameter X_f, which is either zero in the no-mixing scenario or reaches large values in the maximal-mixing scenario.

In this thesis, particular attention will be payed to the Higgs bosons prediced by the MSSM. Therefore, the MSSM Higgs sector will be discussed in more detail in the next section.

3.2.3 The Higgs Sector of the MSSM

In SUSY theories at least two doublets of scalar fields are needed to break the electroweak symmetry for the following reasons:

- Due to an additional charged spin-$1/2$ particle, the charged higgsino, chiral anomalies spoil the renormalizability of the theory which only can be canceled if at least two Higgs doublets are introduced.

- In the SM, the field Φ and its conjugate $\tilde{\Phi}$ generate the masses of the down- and up-type fermions, respectively. In SUSY theories, however, the Higgs sector of the Lagrangian cannot contain the conjugate fields. Therefore a second Higgs doublet with the same hypercharge as the conjugate field is needed to generate masses for the up-type fermions.

In the MSSM the minimum of two doublets of scalar fields with opposite hypercharge is introduced:

$$\begin{aligned} H_1 &= \begin{pmatrix} H_1^0 \\ H_1^- \end{pmatrix} \quad \text{with} \quad Y_{H_1} = -1, \\ H_2 &= \begin{pmatrix} H_2^+ \\ H_2^0 \end{pmatrix} \quad \text{with} \quad Y_{H_2} = +1. \end{aligned} \tag{3.44}$$

The Higgs potential V_H has three different components:
The D terms for the two Higgs fields leading to the Higgs self-couplings,

$$\begin{aligned} V_D =& \frac{g_2^2}{8}\left[4|H_1^\dagger H_2|^2 - 2|H_1|^2|H_2|^2 + \left(|H_1|^2\right)^2 + \left(|H_2|^2\right)^2\right] \\ &+ \frac{g_1^2}{8}\left(|H_2|^2 - |H_1|^2\right), \end{aligned} \tag{3.45}$$

and the F term for the mass terms,

$$V_F = \mu^2\left(|H_1|^2 + |H_2|^2\right). \tag{3.46}$$

In addition, there are Higgs mass and bilinear coupling terms from soft-SUSY breaking:

$$V_{soft} = m_{H_1}^2 H_1^\dagger H_1 + m_{H_2}^2 H_2^\dagger H_2 + B\mu\left(H_2 \cdot H_1 + h.c.\right). \tag{3.47}$$

The full scalar potential is then the sum of all three terms

$$V_H = V_D + V_F + V_{soft}. \tag{3.48}$$

If one chooses now the vacuum expectation value of H_1^- to be zero, one automatically obtains $\langle H_2^+\rangle_0 = 0$. This means there is no non-vanishing vacuum expectation value for charged Higgs fields. Therefore this potential can only break the $SU(2)_L \times U(1)_Y$ gauge symmetry but preserves the electromagnetic $U(1)_Q$ symmetry.
After the insertion of equation 3.44 in the D-, F- and SUSY breaking terms and the substitutions

$$\bar{m}_1^2 = |\mu|^2 + m_{H1}^2, \quad \bar{m}_2^2 = |\mu|^2 + m_{H2}^2, \quad \bar{m}_3^2 = B\mu \tag{3.49}$$

the scalar potential 3.48 contains five parameters: $\bar{m}_1^2$, $\bar{m}_2^2$, $\bar{m}_3^2$ and $g_{1,2}$. Furthermore, the Higgs potential is CP conserving at tree level because the phase of the only complex variable $B\mu$ can be absorbed in the phases of the fields H_1 and H_2.

Electroweak Symmetry Breaking in MSSM To achieve electroweak symmetry breaking, a combination of the fields H_1^0 and H_2^0 is need to acquire a negative squared mass term. This is the case if

$$\bar{m}_3^4 > \bar{m}_1^2 \bar{m}_2^2. \tag{3.50}$$

Futhermore, to bound V_H from below for large values of the Higgs fields,

$$\bar{m}_1^2 + \bar{m}_2^2 > 2|\bar{m}_3^2| \tag{3.51}$$

has to be satisfied. This requires explicitly $\bar{m}_1^2 \neq \bar{m}_2^2$ or

$$m_{H_1}^2 \neq m_{H_2}^2. \tag{3.52}$$

Therefore, to break the electroweak symmetry one also has to break the supersymmetry, because $V_{soft} \neq 0$. In constrained MSSM models the soft SUSY breaking Higgs masses are equal at high energy, $m_{H_1} = m_{H_2}$, and only their running to lower energies lifts this degeneracy so that equation 3.52 is satisfied. This means that in MSSM the electroweak symmetry is broken through radiative corrections (radiative symmetry breaking) which makes it more natural and elegant than in the SM where the breaking is forced with the definition $\mu^2 < 0$.

The MSSM Higgs Bosons As in the SM, the neutral components of the two Higgs fields acquire non-zero vacuum expectation values[7]

$$\langle H_1^0 \rangle_0 = \frac{v_1}{\sqrt{2}}, \qquad \langle H_2^0 \rangle_0 = \frac{v_2}{\sqrt{2}}. \tag{3.53}$$

An important parameter is the ratio of the two vacuum expectation values, defined as

$$\tan\beta = \frac{v_2}{v_1}. \tag{3.54}$$

With the knowledge of $\tan\beta$, m_{H_1} and m_{H_2}, the values B and μ^2 are fixed while the sign of μ stays undetermined.

To obtain the Higgs bosons (i.e. the mass eigenstates of the Higgs fields) one parametrizes the exitations of the complex scalar field doublets with respect to the vacuum expectation value in the following way:

$$\begin{aligned} H_1 &= \frac{1}{\sqrt{2}} \begin{pmatrix} v_1 + H_1^0 + iP_1^0 \\ H_1^- \end{pmatrix} \\ H_2 &= \frac{1}{\sqrt{2}} \begin{pmatrix} H_2^+ \\ v_2 + H_2^0 + iP_2^0 \end{pmatrix} \end{aligned} \tag{3.55}$$

where the real components correspond to the CP-even Higgs bosons and the imaginary parts to the CP-odd Higgs and Goldstone bosons. After the diagonalization of the squared Higgs mass matrices

$$\mathcal{M}_{ij}^2 = \frac{1}{2} \frac{\partial^2 V_H}{\partial H_i \partial H_j} \bigg|_{\langle H_1^0 \rangle_0 = v_1/\sqrt{2},\ \langle H_2^0 \rangle_0 = v_2/\sqrt{2},\ \langle H_{1,2}^\pm \rangle_0 = 0} \qquad (i,j = 1,2) \tag{3.56}$$

one obtains relations for the Higgs boson masses and their mixing angles.

The Higgs mass eigenstates are obtained by the following rotation of the charged and the real and imaginary parts of the neutral Higgs states, respectively:

$$\begin{pmatrix} G^\pm \\ H^\pm \end{pmatrix} = \begin{pmatrix} \cos\beta & \sin\beta \\ -\sin\beta & \cos\beta \end{pmatrix} \begin{pmatrix} H_1^\pm \\ H_2^\pm \end{pmatrix} \tag{3.57}$$

---

[7] Also here the vacuum expectation value of the charged components of the scalar fields is zero for the same reason as in the SM: the electromagnetic gauge symmetry must remain unbroken.

$$\begin{pmatrix} G^0 \\ A \end{pmatrix} = \begin{pmatrix} \cos\beta & \sin\beta \\ -\sin\beta & \cos\beta \end{pmatrix} \begin{pmatrix} P_1^0 \\ P_2^0 \end{pmatrix} . \tag{3.58}$$

$$\begin{pmatrix} H \\ h \end{pmatrix} = \begin{pmatrix} \cos\alpha & \sin\alpha \\ -\sin\alpha & \cos\alpha \end{pmatrix} \begin{pmatrix} H_1^0 \\ H_2^0 \end{pmatrix} \tag{3.59}$$

with the mixing angle α given by

$$\alpha = \frac{1}{2} \arctan \left(\tan 2\beta \frac{M_A^2 + M_Z^2}{M_A^2 - M_Z^2} \right) \tag{3.60}$$

The neutral and charged Goldstone bosons G^0, $G^\pm$ are massless and, as in the SM, absorbed by the electroweak gauge bosons Z^0 and $W^\pm$ to form their longitudinal components and to acquire their masses.
The mass eigenstate of the neutral CP-odd Higgs boson A is

$$M_A^2 = -\frac{2\bar{m}_3^2}{\sin 2\beta} \tag{3.61}$$

while the masses of the CP-even neutral Higgs bosons h and H are

$$M_{h,H}^2 = \frac{1}{2} \left[M_A^2 + M_Z^2 \mp \sqrt{(M_A^2 + M_Z^2)^2 - 4M_A^2 M_Z^2 \cos^2 2\beta} \right] , \tag{3.62}$$

respectively.
The mass eigenstates of the charged Higgs bosons are

$$M_{H^\pm}^2 = M_A^2 + M_W^2 , \tag{3.63}$$

where M_W is the mass of the W boson.

As one can see, the MSSM Higgs sector is very constrained. The two scalar field doublets require in principle six parameters $M_h, M_H, M_A, M_{H^\pm}, \beta$ and α. At tree level, only two of these parameters are free, usually chosen to be M_A and $\tan\beta$. Furthermore, at tree level the Higgs masses obey a strict hierarchy:

$$\begin{aligned} M_H &> \max(M_A, M_Z), \\ M_{H^\pm} &> M_W, \\ M_h &\leq \min(M_A, M_Z) \cdot |\cos 2\beta| \leq M_Z . \end{aligned} \tag{3.64}$$

Thus, the upper limit on the mass of the h boson is M_Z at tree level. Higher-order corrections move this mass limit to about 130 GeV in the maximal mixing scenario.
A consequence of these constraints is the M_A-dependency of all Higgs masses (see Fig. 3.4) and the degeneracy of the masses of either A and h at small M_A or A and H at large M_A. In the most extreme case for $M_A \sim 130$GeV and high $\tan\beta$, all three neutral Higgs bosons are degenerate, i.e. have the same mass.

3.2.4 Constraints on the MSSM Higgs Sector

Further constraints on the free parameters of the MSSM Higgs sector can be obtained from the requirement on the consistency of the theory and from direct experimental searches. This subsection gives a short overview of the major constraints. More detailed information and indirect bounds from electroweak precision measurements can be found in Ref. [14].

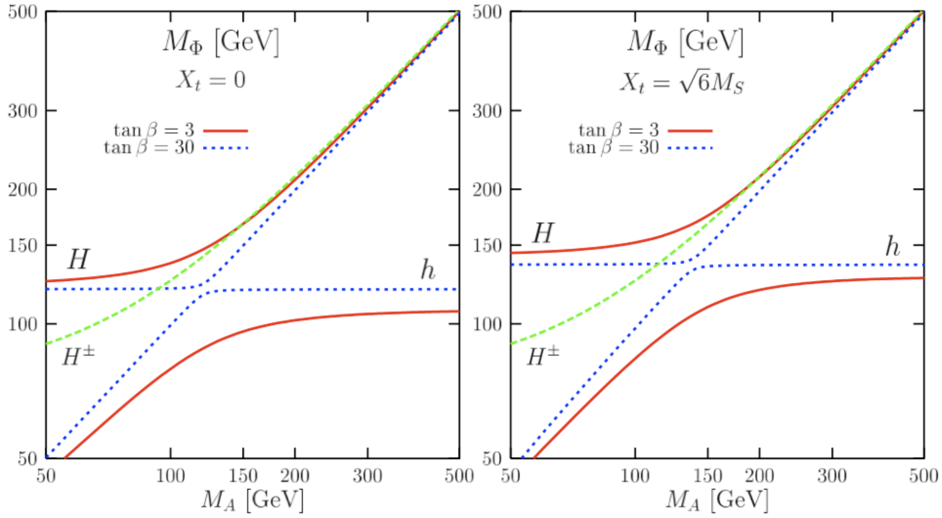

Figure 3.4: MSSM Higgs boson masses as a function of M_A for two values of $\tan\beta$ in the no mixing (left) and maximal mixing (right) scenario with the SUSY breaking scale $M_S = 2\,\mathrm{TeV}$. All other SUSY parameters are set to 1 TeV, radiative corrections are included.

3.2.4.1 Theoretical Bounds

- The free parameter $\tan\beta$ can be constrained by requiring that Higgs couplings to fermions to remain small enough for perturbative calculations. This leads to loose bounds of $0.3 \leq \tan\beta \leq 150$. Withing the framework of the contrained MSSM (cMSSM) these bounds tighten to

$$1 \leq \tan\beta \leq \frac{m_t}{m_b} \approx 60, \tag{3.65}$$

as described in [15].

- According to equation 3.64, the value of M_h at tree level has to be lower than M_Z. However, radiative corrections lead to higher values. To estimate the maximum value for M_h one has to vary all SUSY parameters which contribute to the radiative corrections. Including theoretical and experimental uncertainties one obtains a conservative maximum of

$$M_h^{max} \simeq 144\,\mathrm{GeV} \quad \text{for} \quad m_t \simeq 178\,\mathrm{GeV} \ \ [16,17]. \tag{3.66}$$

3.2.4.2 Constraints from Direct Higgs Boson Searches

Experimental bounds on the Higgs boson masses and $\tan\beta$ have been obtained from the Higgs searches at LEP2 and Tevatron. Since in this thesis the search for neutral MSSM Higgs boson at the LHC is studied, only the bounds on the neutral Higgs bosons are discussed:

- At LEP2 searches were performed for the pair production channel $e^+e^- \to hA/HA$ with subsequent decays into $(bb)(bb)$ or $(bb)(\tau\tau)$ [18]. 95 % CL limits on the h and A masses of

$$\begin{aligned} M_h &> 91.0\,\mathrm{GeV} \quad \text{and} \\ M_A &> 91.9\,\mathrm{GeV}, \end{aligned} \tag{3.67}$$

have been derived, where maximal coupling of the hA pairs to the Z boson has been assumed, which is the case in the anti-decoupling regime[8] as well as for large $\tan\beta$.

- Another Higgs production process at LEP2 is the Higgs-strahlung process $e^+e^- \rightarrow Zh/ZH$. In the decoupling regime[9] or also the anti-decoupling regime the lower bound on the SM Higgs mass is also valid for the MSSM Higgs bosons h/H:

$$M_{h/H} > 114.4\,\mathrm{GeV} \tag{3.68}$$

- More recent limits were obtained at Tevatron where neutral MSSM Higgs searches are mainly performed in the $h/H/A \rightarrow \tau\tau$ channel. The results can be found in Ref. [19]. The constraints on the $M_A - \tan\beta$ parameter space are shown in Fig. 3.5.

3.3 Neutral MSSM Higgs Boson Production at the LHC

The last two sections in this chapter deal with the production and decay channels for MSSM Higgs bosons accessible at the LHC. In proton-proton collisions at the LHC, the neutral MSSM Higgs bosons are produced in four different processes (for the tree-level Feynman graphs see Fig. 3.6):

- The CP-even Higgs bosons h and H can be produced in association with weak gauge bosons W/Z: $q\bar{q} \rightarrow W/Z + h/H$. This mode is also called Higgs-strahlung. The pseudoscalar Higgs boson A cannot be produced in this channel since it does not couple to gauge bosons at tree level because of CP-invariance in the MSSM.
- For the same reason only the h and H bosons can be produced via vector boson fusion: $qq \rightarrow qq + V^*V^* \rightarrow qq + h/H$ (where $V = W, Z$).
- In the gluon-gluon fusion process, all neutral MSSM Higgs bosons can be generated: $gg \rightarrow h/H/A$.
- Finally, a very important Higgs production mode is the associated production with heavy quarks: $gg, q\bar{q} \rightarrow Q\bar{Q} + h/H/A$ ($Q = t, b$), which can be used for trigger and background suppression.

A summary of the production cross sections for the neutral MSSM Higgs bosons at the LHC is given in Fig. 3.7. The cross sections for the individual processes as well as the total Higgs production cross section are plotted as functions of the Higgs masses for $\tan\beta = 3$ and $\tan\beta = 30$. The maximal mixing scenario with $X_t = \sqrt{6}M_S$ and $M_S = 2\,\mathrm{TeV}$ was chosen. Furthermore, the top and bottom quark masses are set to $m_t = 178\,\mathrm{GeV}$ and $m_b = 4.9\,\mathrm{GeV}$, respectively, and NLO QCD corrections have been taken into account.
As one can see, the gluon fusion and the associated production with b-quarks are dominating by at least an order of magnitude. Especially for higher values of $\tan\beta$, the associated production with b-quarks becomes dominant. This will have a strong impact on the searches for the neutral MSSM Higgs bosons performed in this thesis.

---

[8] In the anti-decoupling regime, the pseudoscalar Higgs boson is very light: $M_A \ll M_Z$. Here, at large values of $\tan\beta$ the h and the A bosons are degenerate in mass, while the H boson is degenerate in mass with the Z boson. Therefore the properties of the h and H bosons are reversed compared to the decoupling regime.

[9] In the decoupling regime, the pseudoscalar Higgs boson mass becomes large, $M_A \gg M_Z$, and the light CP-even Higgs boson reaches its maximal mass. The masses of the other Higgs bosons H and $H^\pm$ get then very close to M_A: $M_A \simeq M_H \simeq M_{H^\pm}$. One characteristic of this regime is that, especially for large $\tan\beta$, the couplings of the h boson to SM particles approach the couplings of the SM Higgs while the couplings of the H boson are reduced to the value for the pseudoscalar Higgs boson A (up to a sign).

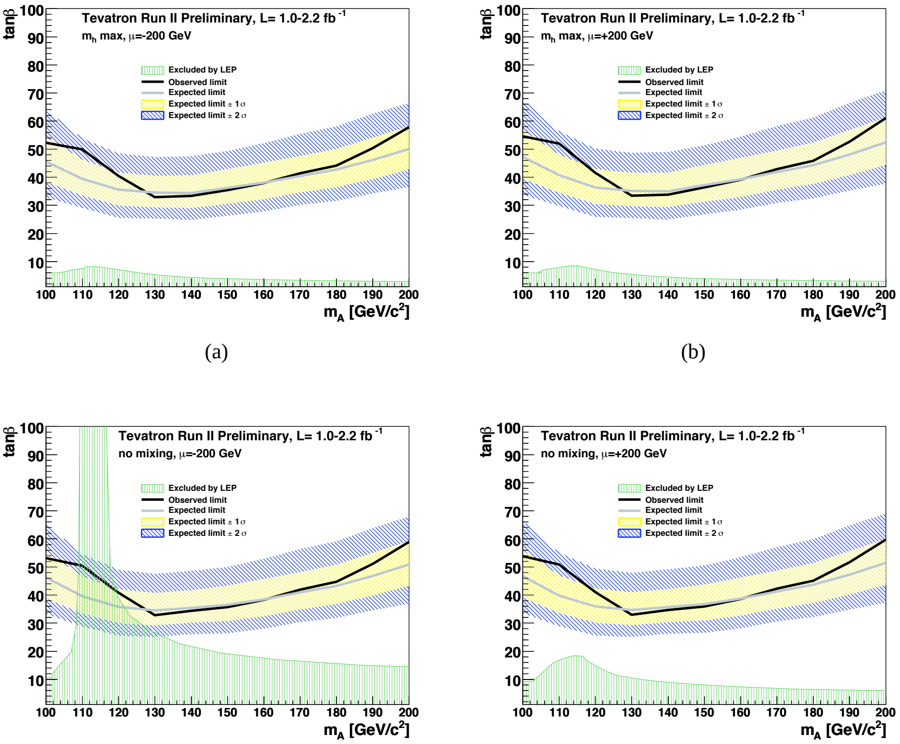

(a) (b)

(c) (d)

Figure 3.5: 95% CL exclusion contours in the $\tan\beta - M_A$ plane from direct searches at Tevatron [19]. The results are shown for the maximal mixing (top) and no-mixing (bottom) scenarios for $\mu < 0$ (left) and $\mu > 0$ (right). The black line denotes the observed limit, the grey line the expected limit with hatched yellow and blue 1 and $2\,\sigma$ error bands, respectively. The hatched light-green areas indicate the limits from LEP.

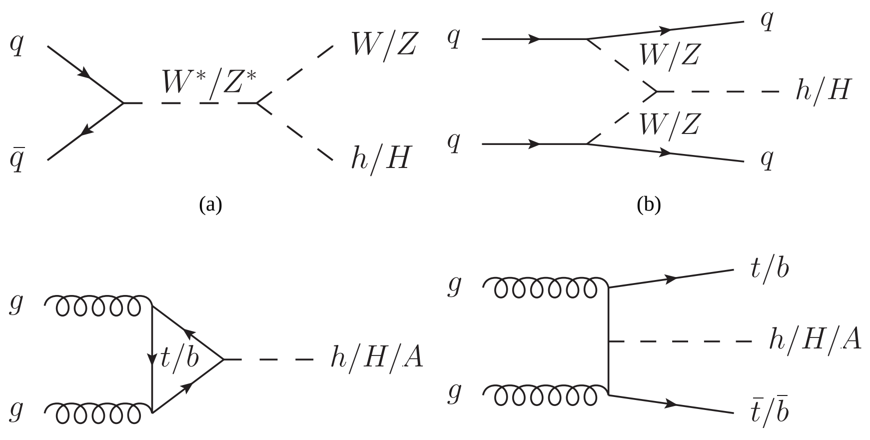

(a) (b) (c) (d)

Figure 3.6: The dominant production modes for neutral MSSM Higgs bosons at the LHC: (a) Higgsstrahlung, (b) vector boson fusion, (c) gluon fusion and (d) associated production with heavy quarks.

For comparison of the Higgs boson production with usual production rates of standard model particles, the total proton-proton production cross-section and cross-sections for several standard model processes are shown in Fig. 3.8. Many standard model processes are sources of background for the Higgs signal processes and their overwhelmingly high cross-sections pose a serious challenge for the Higgs searches. This underlines the need for a good understanding of the background processes, efficient event selection and precise background estimation.

3.4 Decay Modes of the Neutral MSSM Higgs Bosons

In the standard model the tree-level production and decay properties of the Higgs boson are fully determined once its mass is fixed. Since its couplings to fermions and gauge bosons are proportional to the particle masses, the Higgs boson will decay dominantly into the heaviest particles allowed by the phase space. In the MSSM however, this is not the case since the MSSM Higgs couplings depend on $\tan\beta$ and the mixing angle α given in equation 3.60. The most important neutral MSSM Higgs boson couplings normalized to the ones of the standard model Higgs boson are listed in Table 3.5. Besides these standard model-like decays, there are additional modes that should be mentioned.

Φ	$g_{\Phi\bar{u}u}$	$g_{\Phi\bar{d}d}$	$g_{\Phi VV}$
H_{SM}	1	1	1
h	$\cos\alpha/\sin\beta$	$-\sin\alpha/\cos\beta$	$\sin(\beta-\alpha)$
H	$\sin\alpha/\sin\beta$	$\cos\alpha/\cos\beta$	$\cos(\beta-\alpha)$
A	$\cot\beta$	$\tan\beta$	0

Table 3.5: Neutral MSSM Higgs boson (Φ) couplings to up-type and down-type fermions and to gauge bosons normalized to the SM Higgs boson couplings.

The decay modes of the neutral MSSM Higgs bosons can be grouped into three classes:

- **Decay into SM particles:** These are the most important decay modes. Their branch-

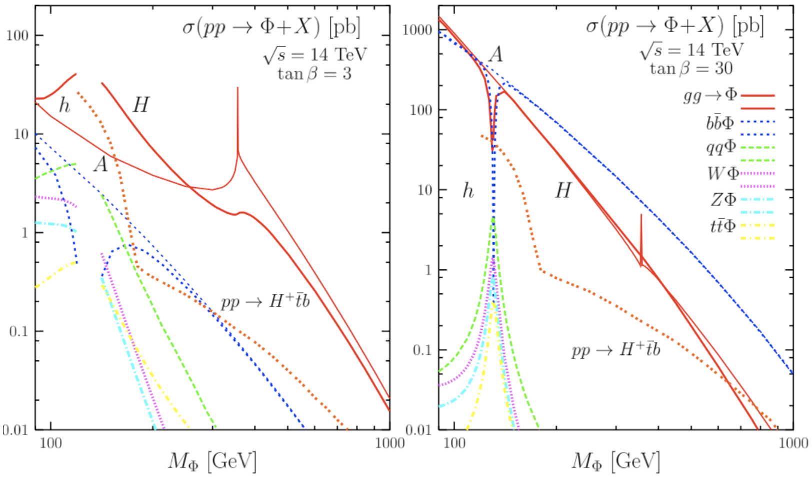

Figure 3.7: Production cross sections for the MSSM Higgs bosons $\Phi = h, H, A, H^{\pm}$ at the LHC for $\tan\beta = 3$ (left) and $\tan\beta = 30$ (right).

ing ratios are, however, depending on the MSSM parameters and will be discussed in more detail in the following.

- **Decay into other Higgs bosons:** The presence of additional Higgs bosons allows for decays of the heavy CP-even H boson into a pair of lighter CP-even or CP-odd Higgs bosons h or A. These decays, however, are only relevant in small regions of the MSSM parameter space.
- **Decay into SUSY particles:** Due to the additional SUSY particle content in the MSSM a wide spectrum of new decay modes opens up, however only when these particles are lighter than the Higgs bosons. The decays involving SUSY particles are treated, for example, in Ref. [14].

The decay rates of MSSM Higgs bosons into standard model particles depend on the choice of MSSM parameters. Starting from standard model-like decays of the light CP-even h boson at low mass values the prefered decay modes change with increasing Higgs masses and $\tan\beta$. We concentrate in the following on scenarios with $\tan\beta \gg 1$, where the coupling to down-type fermions is strongly enhanced.

The decay branching ratios of the neutral MSSM Higgs bosons are shown in Fig. 3.9 for $\tan\beta = 30$. Radiative corrections are included and the maximal-mixing benchmark scenario was chosen. Like in previous sections the properties of the Higgs sector are discussed for the decoupling and the anti-decoupling regimes. Reference [14] also provides information on several other parameter regimes.

Decoupling Regime For the assumed value of $\tan\beta = 30$, the decoupling regime starts at $M_A \gtrsim 150\,\mathrm{GeV}$. In this case, the lighter CP-even h boson reaches a maximal value of $M_h \approx 130\,\mathrm{GeV}$ and its couplings are equal to the couplings of the standard model Higgs boson. Therefore the dominant decay channels prefered by phase space are the decays into $b\bar{b}$ and WW^*. For the chosen scenario with $\tan\beta \gg 1$, the heavier Higgs bosons H and A decay almost exclusively into $b\bar{b}$ and $\tau^+\tau^-$ due to the enhanced couplings to down-type fermions. An additional decay channel which is subject of this thesis, is the decay into $\mu^+\mu^-$ which is significantly enhanced compared to the standard model. All other kinematically allowed decay modes are suppressed for high values of $\tan\beta$.

Anti-Decoupling Regime The anti-decoupling regime for $\tan\beta = 30$ corresponds to $M_A \lesssim 130\,\mathrm{GeV}$. The degenerate h and A bosons decay dominantly into down-type

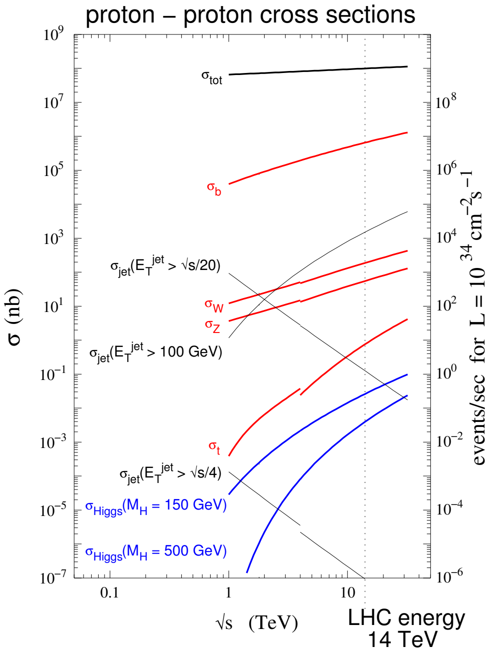

Figure 3.8: Predictions of proton-proton cross sections as a function of the c.m. energy: the total cross section as well as production cross sections of important processes at the LHC are shown.

fermions, like A and H in the decoupling regime. In this regime, the heavier Higgs boson H with its mass of $M_H \sim 140\,\text{GeV}$ plays the role of the standard model Higgs decaying dominantly to the heaviest particles allowed by phase space. One important difference occurs in the low M_A-range: if h and A are light enough the decays $H \to hh$ and $H \to AA$ are by far the dominant ones with branching ratios of $\sim 50\,\%$.

Discovery Channels for Neutral MSSM Higgs Bosons Fig. 3.9 shows that the neutral MSSM Higgs bosons decay predominantly ($\sim 90\,\%$) into $b\bar{b}$. This channel, however is not preferred experimentally since the overwhelming QCD background produced in proton-proton collisions poses a serious challenge and it is difficult to trigger on the signal. With a branching ratio of about $10\,\%$, the decay into a τ-lepton pair is still rather frequent. Assuming a precise τ reconstruction and identification, this channel is the most favoured

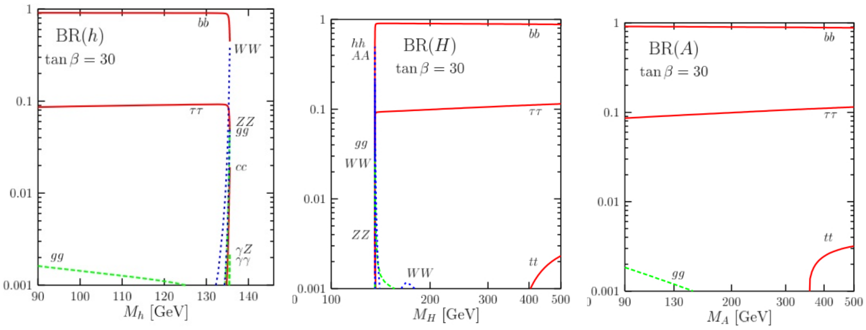

(a) (b) (c)

Figure 3.9: The decay branching ratios of the (a) light CP-even, (b) the heavy CP-even and (c) the CP-odd neutral MSSM Higgs bosons as a function of their masses for a $\tan\beta = 30$.

one for discovery or exclusion in a wide parameter range of MSSM.
Another interesting channel is the decay into two muons, $h/H/A \rightarrow \mu^+\mu^-$, in spite of the low branching ratio of about 3×10^{-4}, which is rather constant over the whole M_A range. The $h/H/A \rightarrow \mu^+\mu^-$ channel provides a very clean signature in the detector and allows for the most precise Higgs mass measurement due to the fully reconstructable final state. Therefore, this decay mode, which is also the subject of this thesis, is an important addition to the $h/H/A \rightarrow \tau^+\tau^-$ channel.

Chapter 4

Search for the Neutral MSSM Higgs Bosons in the Decay Channel $h/H/A \to \mu^+\mu^-$

This chapter deals with the MSSM Higgs boson search in the decay channel $h/H/A \to \mu^+\mu^-$ with the ATLAS detector. A reference ATLAS study of this channel has been performed in [20] assuming p-p collisions at the nominal centre-of-mass energy of $\sqrt{s} = 14\,\mathrm{TeV}$. Since the LHC will start operation at lower c.m. energies of $\sqrt{s} = 7 - 10\,\mathrm{TeV}$, the work presented in this thesis gives an update on the expected performance in this analysis channel for early data. Therefore data from Monte Carlo simulations with a c.m. energy of $\sqrt{s} = 10\,\mathrm{TeV}$ were analysed using modified analysis cuts to cope with the expected conditions at lower energies.

The analysis is performed for a $\mu^+\mu^-$ invariant mass range from 120 up to $500\,\mathrm{GeV}$ with three different Higgs masses in the $b\bar{b}A$ associated production mode. This chapter introduces the analysis strategies and sets the stage for the development of a background estimation method which is presented in Chapter 5. Since the background contribution can be estimated from final states with one or two electrons, Section 4.4 describes the electron reconstruction. The background processes are simulated using a detailed (full) simulation of the ATLAS detector with the nominal detector layout. The three signal datasets were simulated by the faster ATLFAST detector simulation based on a parametrization of the detector response to different particles.

4.1 Motivation

In the Standard Model the decay $H \to \mu^+\mu^-$ is very unlikely since the Higgs boson couples dominantly to the gauge bosons $W^\pm$ and Z^0 or the heavy fermions t, b and τ. This is however not the case in the MSSM where for large values of $\tan\beta$ the decay into down-type fermion pairs including two muons is strongly enhanced.

Since the couplings of the Higgs bosons to the fermions are proportional to the fermion masses, the branching ratios of $h/H/A \to \tau\tau/\mu\mu/ee$ scale as $m_\tau^2/m_\mu^2/m_e^2$. Thus the decay into two electrons can be neglected and $h/H/A \to \mu^+\mu^-$ is suppressed by a factor of ~ 280 with respect to the $h/H/A \to \tau^+\tau^-$ decay. Nevertheless, the dimuon channel provides a very clean signature in the detector and the excellent dimuon mass resolution of the ATLAS detector allows for the most precise Higgs mass measurements. With these properties, the $h/H/A \to \mu\mu$ decay is a promising channel for either the exclusion of a

wide region of the $m_A - \tan\beta$ parameter space or the discovery of the Higgs boson.
The study presented in this chapter concentrates on Higgs masses of 130, 150 and 200 GeV at a benchmark point of $\tan\beta = 40$ and is performed within the m_h^{max} MSSM scenario. For comparison, a detailed study of the discovery potential at $\sqrt{s} = 14$ TeV with an integrated luminosity of 30 fb^{-1} is presented in [21].

4.2 Signal and Background Processes

4.2.1 Signal

The dominant production modes for neutral MSSM Higgs bosons have been mentioned in the previous chapter. Figure 3.7 shows that the cross sections for the direct production via gluon fusion and the associated production with b-quarks exceed the other processes by at least an order of magnitude. The gluon fusion process $gg \to h/H/A$ is important in the low $\tan\beta$ region ($\tan\beta < 10$) where the Higgs bosons couple strongly to up-type quarks. For larger $\tan\beta$ values the $b\bar{b}(h/H/A)$ production becomes dominant.
The studies presented here concentrate on the large $\tan\beta$ region and therefore on the $b\bar{b}(h/H/A)$ production with a subseqent decay into two muons (see Fig. 4.1). The large $\tan\beta$ region is most promising for studies of the early LHC data, since the A and H boson production cross sections increase approximately quadratically with $\tan\beta$ and also the branching ratio for the decay into two muons is enhanced for larger values of $\tan\beta$. The h production is $\tan\beta$-dependent only for $m_A < 130$ GeV and the branching ratio for $h \to \mu^+\mu^-$ is also rather insensitive to m_A and $\tan\beta$.
The mass degeneracy of the neutral Higgs bosons leads to an additional benefit. For A boson masses $m_A < 130$ GeV, the h and A bosons are degenerate in mass while the heavy H boson mass is rather constant, $m_H \sim 130$ GeV. For $m_A > 130$ GeV, the h boson mass reaches its maximum value of $m_h \sim 130$ GeV while the A and H bosons are degenerate in mass. In the case of $m_A \approx 130$ GeV all three bosons have very similar masses, in particular for large $\tan\beta$. In all cases the mass degeneracy of the A, H and h bosons (illustrated in Fig. 3.4) enhances the signal which has contributions from two or even all three mass eigenstates.

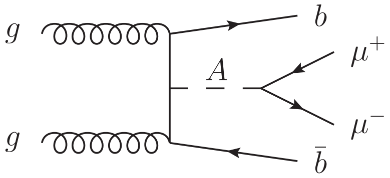

Figure 4.1: Tree-level Feynman diagram for the bbA signal production with subsequent decay of the Higgs boson into two muons.

4.2.2 Background

The search for new physics phenomena at the LHC suffers from extremely high background. In case of the $h/H/A \to \mu^+\mu^-$ decay channel, all processes resulting in a dimuon final state contribute to the background. These processes are discussed in this section, their tree-level Feynman diagrams are shown in Figure 4.2.

Z Boson Production The inclusive Z boson production at the LHC has a relatively high cross section resulting in a large background for searches for new physics. The following production and decay channels are relevant for the $h/H/A \to \mu^+\mu^-$ analysis:

- The dominant background is the Drell-Yan Z production with subsequent decay into two muons. This process has a cross-section of about $1\,\text{nb}$ and results in a high Z peak in the invariant mass distribution. Even the trailing edge of the Z resonance is high enough to produce a dominant background for the MSSM Higgs searches up to masses of several hundred GeV. This process can, however, be efficiently suppressed by requiring the presence of a b-jet in the final state.

- The Z production in association with light jets is a significant background contribution, even after requiring a b-jet in the final state, due to misidentification of light jets as b-jets.

- The $Z + b$-jet production is an irreducible background for the $A/h/H \rightarrow \mu^+\mu^-$ search in the $b\bar{b}A$ production mode, having almost the same signature as the signal.

- In addition to the $Z \rightarrow \mu^+\mu^-$ decay mode the decay channel $Z \rightarrow \tau\tau$ with subsequent leptonic τ decays $\tau \rightarrow \mu\nu\nu$ can contribute to the background. This is however minor because in only $\sim 3\,\%$ of $Z \rightarrow \tau\tau$ events both τ leptons decay into muons and furthermore the invariant dimuon mass is shifted to lower values because of the neutrinos in the τ decay. For the vanishing contribution of this background see Section 4.5.

Top-Pair Production The process $t\bar{t} \rightarrow (W^+b)(W^-\bar{b}) \rightarrow (\mu^+\nu b)(\mu^-\nu\bar{b})$ is another background particularly with the requirement of b-jets in the final state, as will be shown in Section 4.5. This process gives a flat dimuon mass distribution over a wide mass range. Characteristic signatures of the $t\bar{t}$ background are high jet activity and large missing transverse energy caused by the neutrinos from the W decay which both can be used for the suppression of this background.

Diboson Production Finally also WW and ZZ diboson production with dimuon final state contribute to the background for $h/H/A \rightarrow \mu^+\mu^-$. The contributions of these processes are suppressed because of the much lower production cross sections. In Reference [21] it has been shown that the WW and ZZ contributions can be neglected. Thus these backgrounds are not considered in this study.

4.3 Data Samples

Three different Monte Carlo generators are used to simulate the signal and background processes. The following list gives a brief overview of their characteristics, more detailed information can be found in [22]:

- PYTHIA is a general-purpose leading-order (LO) generator for hadronic interactions in pp, e^+e^- and ep collisions. PYTHIA simulates QCD, electroweak, SUSY and other beyond SM processes with two particles in the initial state and with intial- and final state hadronic showers, underlying event, hadronization and particle decays of the partons not involved in the hard collision.

- ALPGEN is a leading-order generator for standard model processes in hadronic collisions. ALPGEN can generate large jet muliplicites and hard jets which is important for processes with jet activity like $Z+$ jets production.

- MC@NLO includes next-to-leading order (NLO) QCD corrections which is, for instance, important for the generation of $t\bar{t}$ production. MC@NLO is interfaced with the Herwig program for hadronization and underlying event simulation.

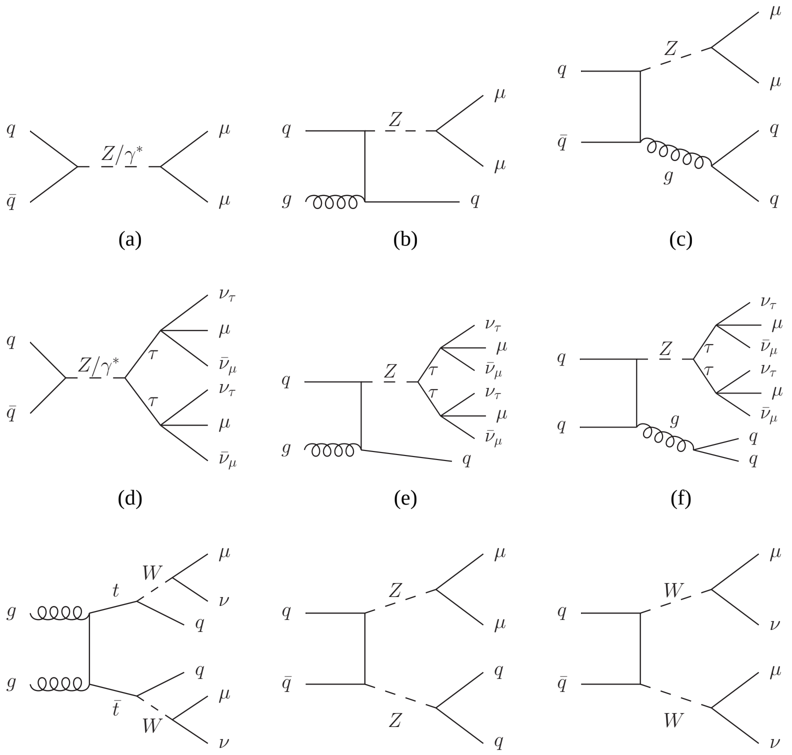

(a) (b) (c)

(d) (e) (f)

(g) (h) (i)

Figure 4.2: Tree-level Feynman diagrams of the most important background processes to the $h/H/A \rightarrow \mu^+\mu^-$ search: Z boson production (a)-(f), $t\bar{t}$ production (g) and diboson production (h)-(i).

The simulated data samples used in this thesis are listed in Table 4.1 and have been generated in the official ATLAS Monte Carlo production[1]. The response of the ATLAS detector to the generated events is simulated using the GEANT4 [23] [24] program within the ATLAS ATHENA [25] software framework. The simulation is followed by the event reconstruction which uses the same algorithms which will be used for data from real p-p collisions. The signal data samples have been simulated with the faster, parametrized detector simulation ATLFAST-II [26]. The good agreement between the full and fast detector simulations has been demonstrated in [27].
In this study for early LHC operation, no pile-up and cavern background effects were considered. At the beginning of the LHC operation, the luminosity will be relatively low and therefore little additional interactions per event are expected and the background radiation in the ATLAS cavern due to secondary neutrons and photons from the collision products (cavern background) should not affect the detector performance.

4.4 Detector Performance

This section deals with the performance of the reconstruction algorithms used for the studies presented in this thesis. The particle reconstruction and identification methods are inparticluar discussed for muons, electrons and photons. Even though electrons are not part of the $A \to \mu^+\mu^-$ final state, electron and photon reconstruction plays an important role for the estimation of the muon background as described in the next chapter.

The detector performance can be characterized in terms of:

- **Efficiency:** The reconstruction efficiency ε is defined as the number of reconstructed and correctly indentified objects $N_{matched}$ divided by the total number of generated truth objects $N_{generated}$:
$$\varepsilon = \frac{N_{matched}}{N_{generated}}, \tag{4.1}$$
where $N_{matched}$ is obtained by matching a reconstructed object ot a generated object within an angular distance of $\Delta R = 0.1$ for electrons and muons, $\Delta R = 0.2$ for photons and $\Delta R = 0.4$ for jets.

- **Fake rate:** The fake rate $\mathcal{F}$ is given by the number of reconstructed but wrongly identified objects N_{fake} which cannot be matched to a generated object by using the above criteria divided by the total number of reconstructed objects $N_{reconstructed}$:
$$\mathcal{F} = \frac{N_{fake}}{N_{reconstructed}}. \tag{4.2}$$

- **Rejection:** The rejection is related to the fakerate and is often used in the context of jet flavour identification. For example, in case of b-jet tagging, the c- and light-jet rejection
$$\mathcal{R}_{u,d,s,c-jets} = \frac{N_{u,d,s,c-jets}}{N^{b-tagged}_{u,d,s,c-jets}}, \tag{4.3}$$
is the ratio of the number of all generated c- or light-jets $N_{u,d,s,c-jets}$ to the number of mistagged c- or light-jets $N^{b-tagged}_{u,d,s,c-jets}$.

---

[1] All Monte Carlo data were generated in the official ATLAS Monte Carlo run MC08. Fully simulated data with the production tag e384-s462-r635-t53 were used, i.e. data without pileup with displaced vertex positions $(1.5\,\mathrm{mm}, 2.5\,\mathrm{mm}, -9.0\,\mathrm{mm})$ simulated with the ATLAS-GEO-02-01-00 detector geometry. For the fast simulated data, the ATLFAST configuaration a82 was used.

Process	Generator	σ[fb]	N_{events}	$\mathcal{L}$[fb^{-1}]	Type
$bbA \rightarrow \mu\mu$, (130, 20)	PYTHIA	15.42	25000	$1.6 \cdot 10^3$	atlfast
$bbA \rightarrow \mu\mu$, (150, 20)	PYTHIA	9.483	25000	$2.6 \cdot 10^3$	atlfast
$bbA \rightarrow \mu\mu$, (200, 20)	PYTHIA	3.372	15000	$4.4 \cdot 10^3$	atlfast
$Z \rightarrow ee$ incl., ($1l$ filter)	PYTHIA	$1143.96 \cdot 10^3$	4547602	3.98	full sim.
$Z \rightarrow \mu\mu$ incl., ($1l$ filter)	PYTHIA	$1143.96 \cdot 10^3$	5069623	4.43	full sim.
$Z \rightarrow \tau\tau$ incl., ($1l$ filter)	PYTHIA	$1128.37 \cdot 10^3$	598866	0.53	full sim.
$Z \rightarrow ee + 0p$ l-jets	ALPGEN	$898.18 \cdot 10^3$	419180	0.45	full sim.
$Z \rightarrow ee + 1p$ l-jets	ALPGEN	$206.57 \cdot 10^3$	45575	0.22	full sim.
$Z \rightarrow ee + 2p$ l-jets	ALPGEN	$72.50 \cdot 10^3$	216945	2.99	full sim.
$Z \rightarrow ee + 3p$ l-jets	ALPGEN	$21.08 \cdot 10^3$	110314	5.23	full sim.
$Z \rightarrow ee + 4p$ l-jets	ALPGEN	$6.00 \cdot 10^3$	1940	0.32	full sim.
$Z \rightarrow ee + 5p$ l-jets	ALPGEN	$1.73 \cdot 10^3$	5500	3.18	full sim.
$Z \rightarrow ee + 0p$ b-jets	ALPGEN	12220	129843	11	full sim.
$Z \rightarrow ee + 1p$ b-jets	ALPGEN	4947	149262	30	full sim.
$Z \rightarrow ee + 2p$ b-jets	ALPGEN	1960	39985	20	full sim.
$Z \rightarrow ee + 3p$ b-jets	ALPGEN	950	10000	11	full sim.
$Z \rightarrow \mu\mu + 0p$ l-jets	ALPGEN	$900.21 \cdot 10^3$	416462	0.463	full sim.
$Z \rightarrow \mu\mu + 1p$ l-jets	ALPGEN	$205.21 \cdot 10^3$	90449	0.441	full sim.
$Z \rightarrow \mu\mu + 2p$ l-jets	ALPGEN	$69.35 \cdot 10^3$	283829	4.09	full sim.
$Z \rightarrow \mu\mu + 3p$ l-jets	ALPGEN	$21.63 \cdot 10^3$	54706	2.53	full sim.
$Z \rightarrow \mu\mu + 4p$ l-jets	ALPGEN	$6.08 \cdot 10^3$	38464	6.33	full sim.
$Z \rightarrow \mu\mu + 5p$ l-jets	ALPGEN	$1.70 \cdot 10^3$	721	0.424	full sim.
$Z \rightarrow \mu\mu + 0p$ b-jets	ALPGEN	12280	298964	24	full sim.
$Z \rightarrow \mu\mu + 1p$ b-jets	ALPGEN	4924	147710	30	full sim.
$Z \rightarrow \mu\mu + 2p$ b-jets	ALPGEN	1917	39352	21	full sim.
$Z \rightarrow \mu\mu + 3p$ b-jets	ALPGEN	936.9	10000	11	full sim.
$Z \rightarrow \tau\tau + 0p$ l-jets	ALPGEN	$902.71 \cdot 10^3$	333393	0.369	full sim.
$Z \rightarrow \tau\tau + 1p$ l-jets	ALPGEN	$209.26 \cdot 10^3$	76428	0.365	full sim.
$Z \rightarrow \tau\tau + 2p$ l-jets	ALPGEN	$70.16 \cdot 10^3$	239460	3.41	full sim.
$Z \rightarrow \tau\tau + 3p$ l-jets	ALPGEN	$21.07 \cdot 10^3$	6485	0.308	full sim.
$Z \rightarrow \tau\tau + 4p$ l-jets	ALPGEN	$6.04 \cdot 10^3$	16500	2.73	full sim.
$Z \rightarrow \tau\tau + 5p$ l-jets	ALPGEN	$1.71 \cdot 10^3$	750	0.439	full sim.
$Z \rightarrow \tau\tau + 0p$ b-jets	ALPGEN	12370	299664	24.2	full sim.
$Z \rightarrow \tau\tau + 1p$ b-jets	ALPGEN	4883	149558	30.6	full sim.
$Z \rightarrow \tau\tau + 2p$ b-jets	ALPGEN	1928	39968	20.7	full sim.
$Z \rightarrow \tau\tau + 3p$ b-jets	ALPGEN	971.8	10000	10.3	full sim.
$t\bar{t}$ (no filter)	MC@NLO	$373.6 \cdot 10^3$	2809658	7.5	full sim.

Table 4.1: Signal and background data samples used for the studies in this thesis. σ is the production cross section at $\sqrt{s} = 10\,\text{TeV}$ (in LO for PYTHIA and ALPGEN and NLO for MC@NLO) and $\mathcal{L}$ is the integrated luminosity corresponding to σ and the number of generated events N_{events}.

- **Resolution:** For instance the transverse momentum resolution is determined as the standard deviation of a Gaussian fit to the distribution of the relative error

  $$\delta p_T = \frac{p_T^{reco} - p_T^{truth}}{p_T^{truth}} \tag{4.4}$$

  in bins of p_T or η, where p_T^{reco} is the reconstructed transverse momentum and p_T^{truth} the corresponding true transverse momentum at generator level.

Muon Reconstruction In the case of the $A \to \mu^+\mu^-$ analysis, the reconstruction and identification of muons is the most important task. One motivation for the study of this channel with low branching ratio is the excellent muon performance of the ATLAS detector. The muon reconstruction in ATLAS [28, 29] includes several strategies:

- **Standalone Muons:** The standalone muon reconstruction algorithm first searches for track segments in each of the three muon stations of the muon spectrometer and then connects them by fitting a curved muon track in the magnetic field. This track is then extrapolated to the interaction point. The standalone muon spectrometer algorithm provides an η coverage up to $|\eta| = 2.7$.

- **Combined Muons:** Combined muon tracks are reconstructed by matching the standalone muons to nearest inner detector tracks via a statistical combination of the two sets of track parameters in the STACO programm [28]. The quality of the matching is given by a χ^2_{match} variable. Combined muons are characterized by very low fake rate but can only be reconstructed up to $|\eta| = 2.5$.

- **Tagged Muons:** Tagged muons are found by extrapolating an inner detector track to the muon spectrometer. This algorithm is particularly important for low momentum muons which do not transverse all three layers of the spectrometer and muons going through the transition region of the spectrometer or the detector gap at $|\eta| \approx 0$. The reconstruction program takes an inner detector track and searches for a nearby track segment in the inner stations of the muon spectrometer. The track parameters of tagged muons are only obtained from the inner detector track while the muon spectrometer segment identifies the object as a muon.

The muon reconstruction efficiencies and fake rates for the three algorithms above are shown in Figs. 4.3 and 4.4. Since the combined muon algorithm provides the best combination of high efficiency and low fake rate, combined muons from the STACO family [28] are used throughout this thesis. Beside the reconstruction efficiency also the muon momentum resolution is important. Figure 4.5 shows the p_T-resolution of combined muons in bins of p_T and η. The average p_T resolution is better than $2 - 3\,\%$. Further details on the muon reconstruction can be found in Reference [30].

Electron Reconstruction The standard electron reconstruction in ATLAS is performed by the EGamma program [31]. It starts from a cluster seed in the electromagnetic calorimeter with transverse energy $E_T \gtrsim 3\,\text{GeV}$. Subsequently a matching track in the inner detector is searched for among all reconstructed tracks except for those which belong to a photon conversion. An electron candidate is found if the extrapolated track matches the calorimeter cluster in a window of $\Delta\eta \times \Delta\phi < 0.05 \times 0.10$ and if the ratio $E^{cluster}/p^{track}$ is lower than 10. On these electron candidates several identification cuts are applied using the information from the calorimeters and the inner detector, classifying the electrons in three categories:

- **Loose electrons:** The least stringent identification criteria are cuts on the energy deposit in the hadron calorimeter (hadronic leakage) and on electromagnetic shower

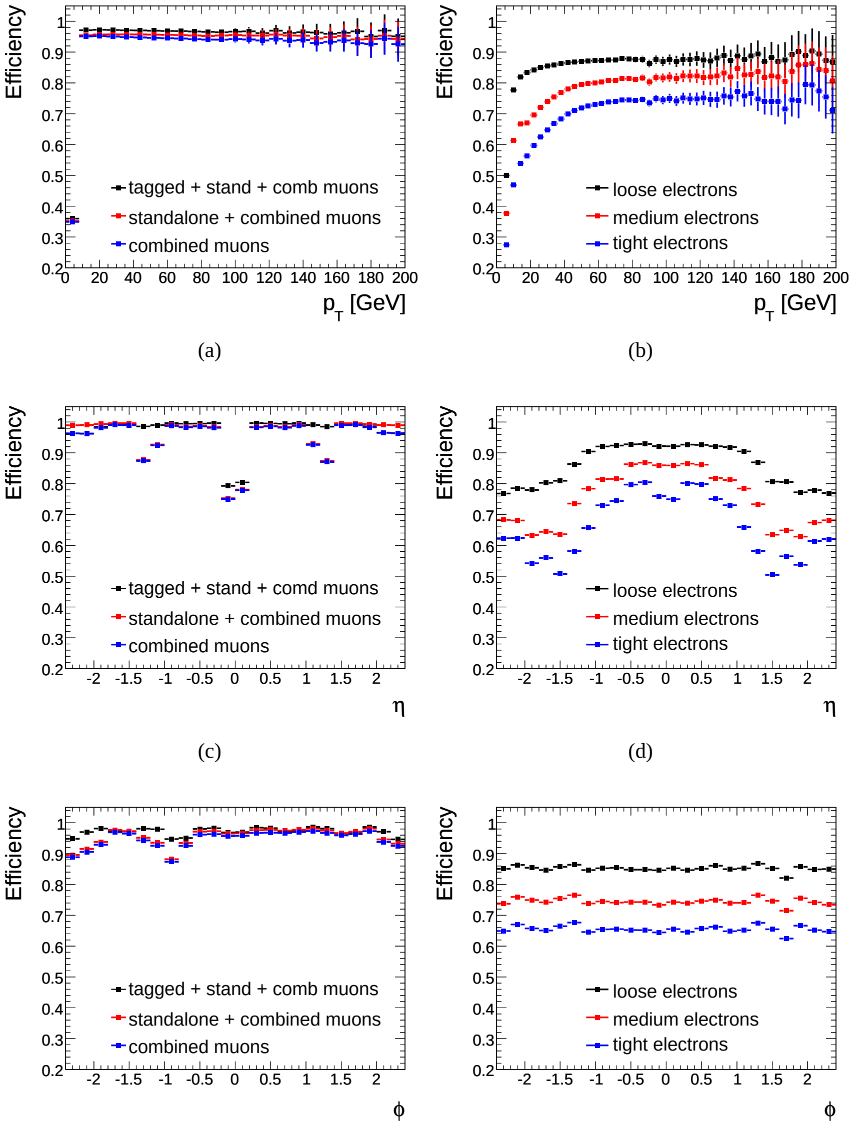

(a) (b)

(c) (d)

(e) (f)

Figure 4.3: Reconstruction efficiencies for muons (a,c,e) and electrons (b,d,f) in inclusive Z events.

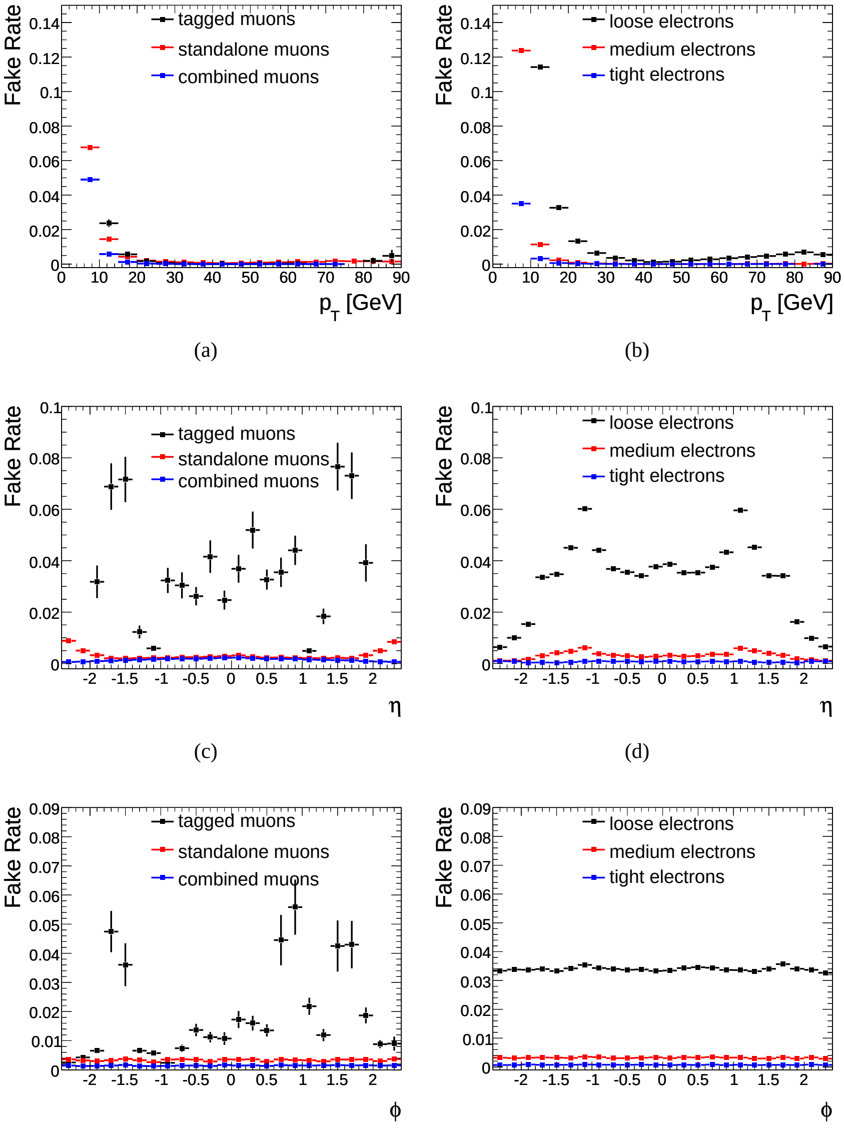

(a) (b)

(c) (d)

(e) (f)

Figure 4.4: Fake rates for muons (a,c,e) and electrons (b,d,f) in inclusive Z events.

shape variables (lateral shower shape and width), obtained only from the middle layer of the EM calorimeter. These criteria provide a high identification efficiency but relatively low rejection of misidentified jets.

- **Medium electrons:** The identification quality can be improved by adding further requirements to the above loose set of cuts. For medium electrons, additional calorimeter information from the strips in the first EM-layer is used improving the shower shape determination. Furthermore, tracking variables like the number of SCT or Pixel hits are included. The medium cuts increase the jet rejection by a factor of 3 with respect to the loose cuts while reducing the efficiency by $\sim 10\%$.
- **Tight electrons:** This set of cuts makes use of all particle-identification tools available for electrons. In addition to the medium cuts the information from the pixel detector and the TRT are used to reduce hadronic background and electrons from photon conversion. The energy deposition around the electron candidate is taken into account to evaluate the isolation of the electron showers. Finally, also the track-shower matching is refined to a window of $\Delta\eta \times \Delta\phi = 0.005 \times 0.02$.

For the studies presented in this thesis medium electrons were chosen which provide a good compromise between good reconstruction efficiency and low fake rate (see Figs. 4.3 and 4.4). The momentum resolution for medium electrons is shown in Figure 4.5. More details on electron reconstruction in ATLAS can be found in [31].

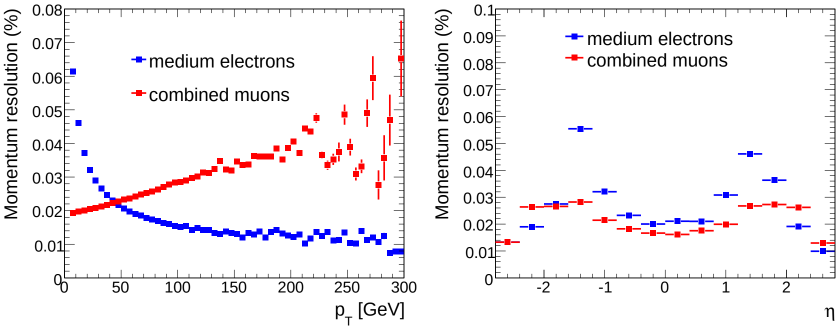

(a) (b)

Figure 4.5: Transverse momentum resolution for muons and and electrons in bins of p_T (a) and η (b), in inclusive Z events.

Photon Reconstruction The reconstruction of photons is very similar to the electron reconstruction and starts with a cluster in the electromagnetic calorimeter. The track matching condition for electrons within a window of $\Delta\eta \times \Delta\phi = 0.05 \times 0.10$ is turned around to veto electrons for the identification of photon candidates. Three different algorithms can be used for photon identification in ATLAS. The default used also for this thesis is a simple cut-based method which makes use of several discriminating variables from the calorimeter system and the inner detector: Hadronic leakage, shower shape variables and track isolation are used to reject fake photons originating from jets containing neutral hadrons like π^0 or η.
More detailed information of the photon reconstruction and identification in ATLAS can be found in [32].

Jet Reconstruction and b-Tagging Also for the jet reconstruction in ATLAS calorimeter clusters are used as a starting point. Clusters in the calorimeters are reconstructed by two different algorithms, the so-called “Tower” and the “Topological” algo-

rithm. Tower clusters are defined in the $\eta - \phi$ plane whereas the topological clusters obtain three-dimensional information on energy depositions.
Calorimeter clusters form the input seeds for the jet algorithms. Again, two algorithms are widely used, the "Cone" and the "k_T" algorithm, which are not decribed further here. More information on the jet reconstruction in ATLAS is provided in Reference [33].
For this analysis, the Cone algorithm with a cone size of $\Delta R = 0.4$ and topological clusters as seeds is chosen.

One characteristic feature of the $b\bar{b}A$ signal is the presence of b-jets with rather low transverse momenta as shown in Figure 4.6. This signature can be used to select the signal events while rejecting the Z (+light jets) background. Several algorithms for the identification of b-jets (b-tagging) can be used to determine whether a given jets originates from a b-quark.

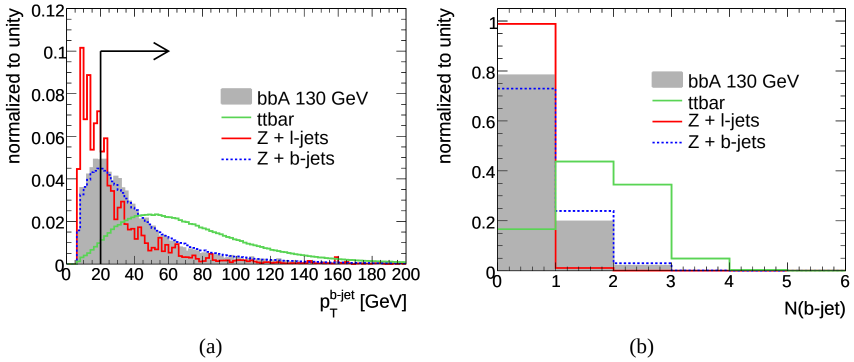

(a) (b)

Figure 4.6: Transverse momentum of the b-jets (a) and the number of reconstructed b-jets per event (b) for $b\bar{b}A,\ A \rightarrow \mu\mu$ events with $m_A = 130\,\text{GeV}$ as well as for the main backgrounds.

All b-tagging algorithms use the special characteristics of b-jets, described by variables like relatively large jet opening angle and a displaced b decay vertex due to the rather long lifetime of b hadrons. This information is then combined with a likelihood method giving the probability that a jet originates from a b-quark. Based on this likelihood estimator the b-tagging algorithm returns a weight parameter for every jet, the so-called b-tag weight.
In this thesis the default b-tagger IP3DSV1 [34] is chosen which uses information from the three-dimensional impact parameter and the secondary vertex. More detailed information on b-tagging in ATLAS is given in Reference [34]. The distribution of the b-tag weight for true b-, c- and light jets is shown in Figure 4.7 for $b\bar{b}A$ and $t\bar{t}$ events. For a fixed cut of b-weight > 1.8125 the identification efficiency of true b-jets is shown in Figure 4.8, while the rejection of c- and light jets is shown in Fig. 4.9. The overall b-tagging efficiency is 60% in the $b\bar{b}A$ sample with a light-jet rejection of ~ 31 and a c-jet rejection of ~ 5 in the $t\bar{t}$ sample. In the Z+jets sample a similar rejection against c-jets is obtained (~ 6), while the light jets can be rejected more efficiently than in $t\bar{t}$ (rejection factor of ~ 77). This can be explained by the lower jet multiplicity in Z+jets events.

Missing Transverse Energy The last important discriminating variable described in this section is the missing transverse energy E_T^{miss}. Reference [33] gives further information on E_T^{miss} reconstruction in ATLAS.
The principle of the E_T^{miss} measurement is the following: The transverse momentum of the two protons in the initial state is zero. Therefore, due to momentum conservation, the total transverse momentum in the final state has to be zero as well. If particles are created in p-p collisions that do not deposit energy in the detector (e.g. neutrinos) the transverse

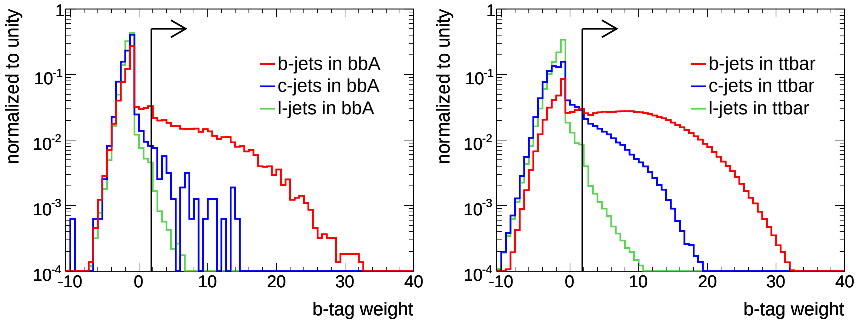

(a) (b)

Figure 4.7: b-tag weight for b-, c- and light jets for $b\bar{b}A$ signal events with $m_A = 130\,\text{GeV}$ and for $t\bar{t}$ events. The black line indicates the cut value 1.8125 for the b-jet selection.

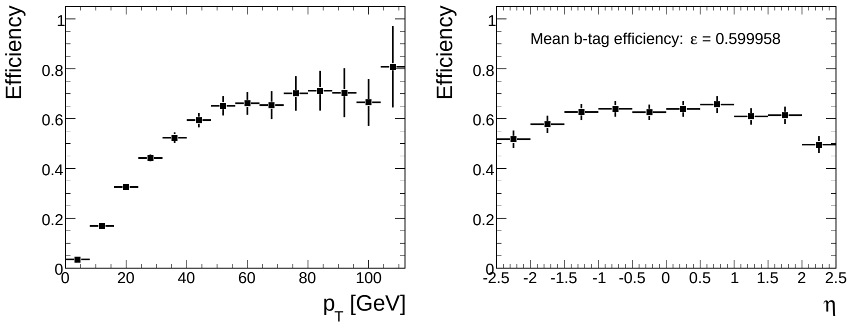

(a) (b)

Figure 4.8: b-tagging efficiency for $b\bar{b}A$ signal events with $m_A = 130\,\text{GeV}$.

energy balance is violated by the missing transverse energy which is equal to the negative sum of the transverse momenta of the remaining visible particles.
Since the $A \rightarrow \mu^+\mu^-$ decay can be fully reconstructed, the missing transverse energy in this process is close to zero, dominated by the finite experimental resolution. E_T^{miss} can be used to suppress the $t\bar{t}$ background which is characterized by a large fraction of E_T^{miss} due to the neutrinos from leptonic W decays which escape the detector without interaction. The E_T^{miss} distribution for the $b\bar{b}A$ signal and in the dominant background processes is shown in Fig. 4.10.

4.5 Event Selection

Two strategies are pursued in the search for the neutral MSSM Higgs bosons produced in association with b-quarks and decaying into two muons:

- Search for a dimuon final state without b-jets.
- Search for a dimuon final state with at least one b-jet.

The extremely high Z background, in particular the dominant Drell-Yan contribution, can be strongly reduced if at least one b-jet is required to be present in the final state. On the other hand, due to the rather low-p_T of the b-jets the b-tagging efficiency in the signal is relatively low. Therefore, in the analysis of the no b-jet final state the signal rate is significantly higher.

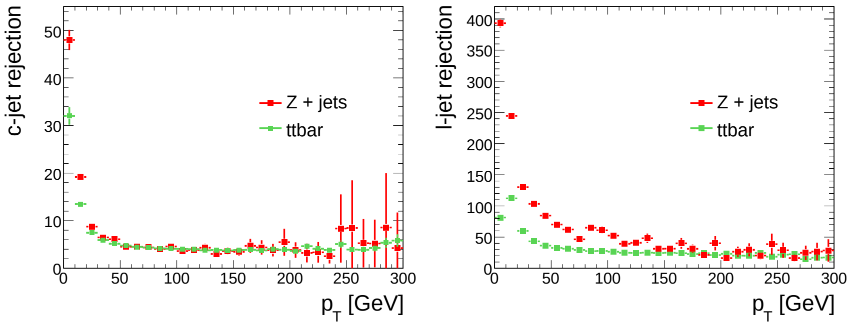

(a) (b)

Figure 4.9: Rejection of c-jets (a) and light jets (b) obtained by the b-tagging algorithm IP3DSV1 in $t\bar{t}$ and Z+jets events.

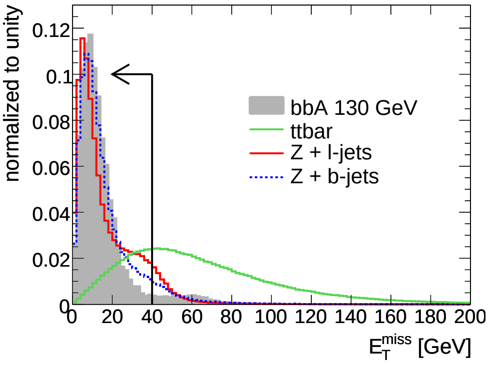

Figure 4.10: Missing transverse energy E_T^{miss} for the $b\bar{b}A$ signal and the dominant background processes. The black line indicated the cut value for the event selection.

In this section, the event selection for both analysis strategies is presented, starting with the selection of muons, electrons and jets, which is common for the two analysis modes. The signal is selected by additional requirements on the jets and the missing transverse energy. Electron selection is needed for the background estimation from control samples described in the next chapter.

4.5.1 Lepton and Jet Selection

The first step in the event selection is the selection of different analysis objects. Very loose cuts are applied here in order to allow for additional studies, like the study of the effects of final state radiation, presented in the Chapter 5.

Leptons

The basic selection for electrons and muons is performed by the subsequent application of the following cuts:

1. **Transverse momentum:** both, electrons and muons, are required to have a transverse momentum of $p_T > 5\,\text{GeV}$.
2. **Azimuthal angle:** the inner detector η-coverage defines the cut $|\eta| < 2.5$.
3. **Identification quality:** the identification quality requires *combined muons* and *medium electrons*.

4. **Isolation:** the leptons are required to be isolated. The isolation is defined through the transverse energy deposit in the calorimeter in a cone of $\Delta R = 0.4$ around the lepton $E_T^{cone:\,\Delta R=0.4}$. The isolation criterion $E_T^{cone:\,\Delta R=0.4}/p_T^{lepton} < 0.2$ rejects leptons from hadronic decays such as in $t\bar{t}$ (see Fig. 4.11). In particular electrons from misidentified jets are also suppressed by the isolation.

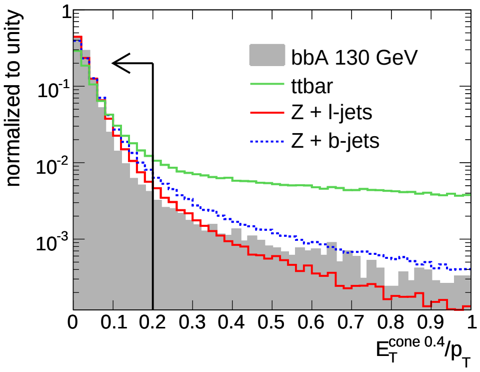

Figure 4.11: Muon isolation: Distribution of $E_T^{cone:\,\Delta R=0.4}/p_T^{lepton}$ for muons in the signal and dominant background samples. The arrow indicates the applied cut at 0.2.

Jets

For the basic jet selection the following set of cuts is applied:

1. **Jet algorithm:** As already mentioned the jets based on topolagical clusters (*Cone4TopoJets*) are used for this analysis.

2. **Transverse momentum:** To reduce the impact of the calorimeter noise the transverse momentum of the jets is required to be $p_T > 20\,\text{GeV}$.

3. **Azimuthal angle:** Since the ATLAS calorimeter system provides a nearly hermetic coverage up to the very forward region an azimuthal cut of $|\eta| < 4.8$ is chosen.

The IP3DSV1 b-tagging algorithm is applied on the jets selected by the above criteria, assigning the b-tag weight to each jet. A jet with a b-tag-weight higher than 1.8125 is assumed as a b-jet. Since the b-tagger uses information from the inner detector, b-jets can only be reconstructed inside $|\eta| < 2.5$.

Overlap Removal

Because of their quite similar reconstruction algorithms it is possible that electrons are misidentified as jets and vice versa, causing an overlap in ΔR between different objects. Also muons can be wrongly reconstructed as electrons or jets. To reduce the number of misidentified objects, the so-called overlap removal is performed, according to the following strategy:

- As muons can be reconstructed with the lowest fake rate, they are used as reference objects. Any other particle overlaping with a reconstructed muon will be considered as misidentified and will be removed.

- Thus, as a second step, all electron candidates inside a cone $\Delta R = 0.4$ around an isolated combined muon are removed. All remaining reconstructed electrons are considered to be real and are used for the analysis.

- Finally, all jets inside a cone $\Delta R = 0.4$ around a medium electron are deleted, since each real electron can also be falsely reconstructed as a jet.

4.5.2 Preselection

Before separating the analysis into two modes with and without b-jets in the final state, one can apply common selection criteria, based on the characteristic signature of the $A \rightarrow \mu^+\mu^-$ decay, requiring the presence of two isolated muons of opposite charge. From the muon p_T distribution in Fig. 4.12 one observes that the muons in the signal tend to have high transverse momenta compared to muons in the background events. However, with decreasing Higgs mass the muon p_T distribution shifts to lower values. To allow for a Higgs mass independent signal selection efficiency, the cut on the transverse muon momentum is chosen at a relatively low value of $p_T > 15\,\mathrm{GeV}$.

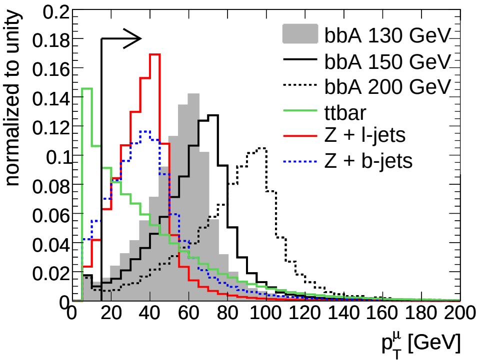

Figure 4.12: Distribution of the muon transverse momentum p_T^μ in the signal and background events. The black line indicated to selection cut.

Two further quality criteria are applied on the combined muons:

- The quality of the track fit is given by the variable χ^2_{fit} which is required to be less than 500.
- The χ^2_{match} value for the matching between the muon spectrometer and inner detector tracks is reqired to be less than 100.

The events passing the above selection are required to have a missing transverse energy lower than $40\,\mathrm{GeV}$. This cut efficiently reduces processes involving neutrinos like in $t\bar{t}$ events with leptonic W decays.

Higgs Mass Resolution The invariant mass distribution of preselected opposite charged muon pairs in $b\bar{b}A$ events is shown in Fig. 4.13 for different Higgs masses. The distributions are fitted with a Gaussian to determine the reconstructed Higgs mass and the mass resolution. The corresponding numbers are summarized in Table 4.2. The mass of the Higgs boson can be reconstructed very precise, the observable width of the resonance is limited by the experimental resolution.

4.5.3 Final State Selection

The last step in the selection chain is the reconstruction of the dimuon final state. At this point the final states are separated into two branches, with 0 reconstructed b-jets and with at least one reconstructed b-jet.

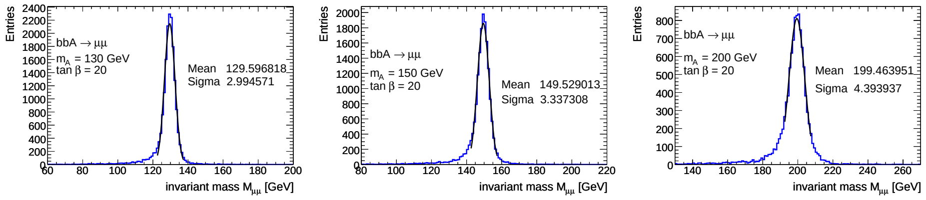

(a) (b) (c)

Figure 4.13: Dimuon mass distributions in the $b\bar{b}A$ signal for an A boson mass of 130 (a), 150 (b) and 200 GeV (c) at $\tan\beta = 20$. The distributions are fitted with a Gaussian within the mass range $m_A \pm 7.5\,\text{GeV}$.

	A boson mass [GeV]		
	130	150	200
Natural width	1.18	1.33	1.73
Observed width σ	2.99 ± 0.023	3.34 ± 0.27	4.39 ± 0.062
Reconstructed mass	129.597 ± 0.025	149.529 ± 0.029	199.464 ± 0.059

Table 4.2: The natural width of the A boson and the observed width and mean of the dimuon mass distribution from the $b\bar{b}A$, $A \rightarrow \mu^+\mu^-$ signal events for different A boson masses for $\tan\beta = 20$.

4.5.3.1 The 0 b-jet Final State

The advantage of the final state with 0 b-jets is the large number of signal events. The also very large background leading to a smooth invariant mass distribution is dominated by the Z production with subsequent decay into two muons. The Higgs signal sits on the trailing edge of the Z resonance in the dimuon mass distribution and the background is several orders of magnitude higher than the signal even for high Higgs masses far away from the Z peak.

The final state is reconstructed by the subsequent application of the following selection cuts:

1. The events are required to pass the preselection. This requirement selects events with the characteristic signature of a $b\bar{b}A \rightarrow \mu^+\mu^-$ decay.
2. To select the final state with 0 b-jets, the number of reconstructed and tagged b-jets with $p_T > 20\,\text{GeV}$ is required to be zero. This cut rejects to some extent the $t\bar{t}$ contribution while the dominant Z background remains almost unaffected.
3. Finally, the numbers of signal and background events are counted in a mass window defined by the width of the Higgs resonance (see Fig. 4.13 and Tab. 4.2): $\Delta m = m_A \pm 2\sigma$.

The numbers of signal and background events after each cut described above are summarized in Tables 4.3, 4.4 and 4.5. The overall signal selection efficiency in the 0 b-jet final state is approximately 53% for a Higgs mass of $m_A = 130\,\text{GeV}$ at $\tan\beta = 40$. The $Z + jets$ background inside the mass window around $M_A = 130\,\text{GeV}$ is two orders of magnitude higher than the signal. The invariant dimuon mass distribution obtained after the cuts is shown in Fig. 4.15(a).

One remark should be made on the Monte Carlo data samples used: The total Z background can either be composed from the ALPGEN Monte Carlo samples ($Z + b$-jets and $Z + l$-jets) or simply taken from the PYTHIA data samples. The advantage of the Z events simulated with PYTHIA is that they have been generated in the full invariant mass range ($M_{ll} > 60\,\text{GeV}$) with high statistics corresponding to $\sim 4\,\text{fb}^{-1}$. The disadvantage is that in PYTHIA the jets originate from the simulation of the parton fragmentation which in general leads to relatively low-energy jets. Jets with higher energy are not taken into account correctly.

The ALPGEN data samples show a more realistic jet environment, i.e. containing harder jets. On the other hand, these data have been produced with an invariant mass cut of $60\,\text{GeV} < M_{ll} < 200\,\text{GeV}$ and statistics corresponding to only $\sim 0.2\,\text{fb}^{-1}$. Therefore these data are not suitable for the background describtion for Higgs masses $m_A > 150\,\text{GeV}$.

For the above reasons, Z events are studied using both generators. Tables 4.4 and 4.5 show that both background describtions are in good agreement. In the following, the ALPGEN samples are used whenever possible while the PYTHIA samples are used only for the case of $m_A = 200\,\text{GeV}$ and when high statistics is needed.

Cut	$b\bar{b}A$ (130 GeV)	$b\bar{b}A$ (150 GeV)	$b\bar{b}A$ (200 GeV)
no cut	61.7	37.9	13.5
p_T, η	55.7[4]	34.3[2]	12.3[1]
ID quality	52.2[4]	32.0[2]	11.5[1]
isolation	49.0[3]	30.0[2]	10.8[1]
preselection	47.4[3]	29.2[2]	10.6[1]
E_T^{miss}	47.1[3]	28.9[2]	10.4[1]
b-jet veto	38.0[3]	22.8[2]	7.91[8]
Δm	32.9[3]	19.6[2]	6.59[8]

Table 4.3: *Cross-section* × *selection efficiency* for signal events with three different Higgs masses and $\tan\beta = 40$ in the 0 b-jet analysis after each selection cut, scaled to $1\,\text{fb}^{-1}$. The numbers in brackets represent the statistical error on the last digit.

Cut	$Z + l$-jets	$Z + b$-jets	Z *incl*	$t\bar{t}$
no cut	$1.20 \cdot 10^6$	$20.06 \cdot 10^3$	$1.144 \cdot 10^6$	$374 \cdot 10^3$
p_T, η	$573[1] \cdot 10^3$	$13.58[2] \cdot 10^3$	$575.8[4] \cdot 10^3$	$44.16[9] \cdot 10^3$
ID quality	$536[1] \cdot 10^3$	$12.73[2] \cdot 10^3$	$538.4[3] \cdot 10^3$	$39.99[8] \cdot 10^3$
isolation	$503[1] \cdot 10^3$	$11.28[2] \cdot 10^3$	$508.6[3] \cdot 10^3$	$6.85[4] \cdot 10^3$
preselection	$473[1] \cdot 10^3$	$9.96[2] \cdot 10^3$	$477.2[3] \cdot 10^3$	$5.42[3] \cdot 10^3$
E_T^{miss}	$472[1] \cdot 10^3$	$9.89[2] \cdot 10^3$	$476.8[3] \cdot 10^3$	$1.28[2] \cdot 10^3$
b-jet veto	$467[1] \cdot 10^3$	$7.31[2] \cdot 10^3$	$469.7[3] \cdot 10^3$	219[6]
Δm (130 GeV)	$1.7[1] \cdot 10^3$	19.41[4]	–	12[1]
Δm (150 GeV)	$8.9[9] \cdot 10^2$	9.88[4]	$8.6[1] \cdot 10^2$	13[2]
Δm (200 GeV)	–	3.11[2]	$2.90[8] \cdot 10^2$	7[1]

Table 4.4: *Cross-section* × *selection efficiency* for the dominant background processes in the 0 b-jet analysis after each selection cut, scaled to $1\,\text{fb}^{-1}$. The numbers in brackets represent the statistical error on the last digit. The Z+jets events have been simulated with ALPGEN, the inclusive Z samples with PYTHIA.

4.5.3.2 The > 0 b-jet Final State

By requiring at least one reconstructed b-jet in the final state one can strongly reject the dominant Z background. Due to the efficient Z suppression the $t\bar{t}$ background is no longer negigible. It can be further suppressed by the following additional cuts:

Cut	$Z \to \tau\tau + l$-jets	$Z \to \tau\tau + b$-jets	$Z \to \tau\tau$ *incl*
no cut	$1.21 \cdot 10^6$	$20.2 \cdot 10^3$	$1.14 \cdot 10^6$
p_T, η	$12.2[2] \cdot 10^3$	$509[5]$	$11.4[1] \cdot 10^3$
ID quality	$11.2[2] \cdot 10^3$	$459[5]$	$10.5[1] \cdot 10^3$
isolation	$7.9[1] \cdot 10^3$	$170[3]$	$7.4[1] \cdot 10^3$
preselection	$2.38[8] \cdot 10^3$	$49[1]$	$2.50[7] \cdot 10^3$
E_T^{miss}	$2.28[8] \cdot 10^3$	$41[1]$	$2.40[7] \cdot 10^3$
b-jet veto	$2.26[8] \cdot 10^3$	$32[1]$	$2.37[6] \cdot 10^3$
Δm (130 GeV)	0	0	0
Δm (150 GeV)	0	0	0
Δm (200 GeV)	0	0	0

Table 4.5: *Cross-section* $\times$ *selection efficiency* for additional background processes in the 0 b-jet analysis after each selection cut, scaled to 1 fb^{-1}. The numbers in brackets represent the statistical error on the last digit. The Z+jets events have been simulated with ALPGEN, the inclusive Z samples with PYTHIA.

- **Acoplanarity:** In two-body decays the momenta of the decay particles are strongly correlated. In particular, if the mother particle has little transverse momentum the muons are emitted back-to-back in the transverse plane. If the muons originate from two different particles as in the case of the $t\bar{t}$ decay, their angular distribution shows no correlation. Therefore a cut $\cos \Delta\phi_{\mu\mu} < 0.65$ is applied on the angle $\Delta\phi_{\mu\mu}$ between the two muons (see Fig. 4.14(a)).
- **Sum of the transverse momenta of all jets:** One characteristic signature of $t\bar{t}$ events is a high hadronic activity, i.e. a large number of hard jets. This can be used to further discriminate against this background. For this purpose, an additional cut is applied on the sum of the transverse momenta of all jets in the event: $\sum p_T^{jet} < 90$ GeV. The distribution of this variable is shown in Fig. 4.14(b).

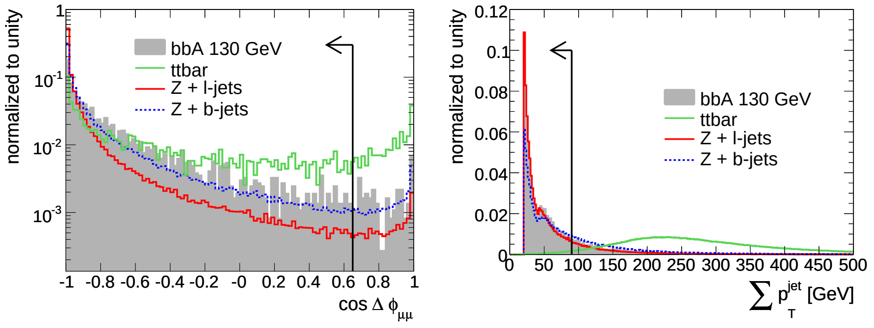

(a) (b)

Figure 4.14: Acoplanarity (a) and sum of the jet transverse momenta (b) for the signal and the dominant background processes. The black line indicates the selection cut.

After the above cuts the events are counted within a mass window according to the width of the Higgs resonance obtained from Table 4.2, i.e. $\Delta m = m_A \pm 2\sigma$. The signal and background rates after each cut applied in the b-jet final state is shown in Tables 4.6, 4.7 and 4.8. The overall selection efficiency for the $b\bar{b}A$ signal with $m_A = 130$ GeV is approximately 9 %. After the additional $t\bar{t}$ rejection both backgrounds, Z and $t\bar{t}$, are of the same order of magnitude. The invariant dimuon mass distribution obtained for this channel is shown in Fig. 4.15(b).

Cut	$b\bar{b}A\,(130\,\mathrm{GeV})$	$b\bar{b}A\,(150\,\mathrm{GeV})$	$b\bar{b}A\,(200\,\mathrm{GeV})$
no cut	61.7	37.9	13.5
p_T, η	55.7[4]	34.2[2]	12.3[1]
ID quality	52.2[4]	32.0[2]	11.5[1]
isolation	49.0[3]	30.0[2]	10.8[1]
preselection	47.4[3]	29.2[2]	10.6[1]
E_T^{miss}	47.1[3]	28.9[2]	10.4[1]
b-jet requirement	9.1[1]	6.1[1]	2.49[5]
$\cos\Delta\phi_{\mu\mu}$	8.8[1]	5.92[9]	2.44[5]
$\sum p_T^{jet}$	6.4[1]	4.10[7]	1.55[4]
Δm	5.6[1]	3.56[7]	1.34[3]

Table 4.6: *Cross-section* × *selection efficiency* for signal events with three different Higgs masses and $\tan\beta = 40$ in the > 0 b-jet analysis after each selection cut, scaled to $1\,\mathrm{fb}^{-1}$. The numbers in brackets represent the statistical error on the last digit.

Cut	$Z + l$-jets	$Z + b$-jets	Z *incl*	$t\bar{t}$
no cut	$1.20 \cdot 10^6$	$20.06 \cdot 10^3$	$1.144 \cdot 10^6$	$374 \cdot 10^3$
p_T, η	$573[1] \cdot 10^3$	$13.58[2] \cdot 10^3$	$575.8[4] \cdot 10^3$	$44.16[9] \cdot 10^3$
ID quality	$536[1] \cdot 10^3$	$12.73[2] \cdot 10^3$	$538.4[3] \cdot 10^3$	$39.99[8] \cdot 10^3$
isolation	$503[1] \cdot 10^3$	$11.30[2] \cdot 10^3$	$508.6[3] \cdot 10^3$	$6.85[4] \cdot 10^3$
preselection	$473[1] \cdot 10^3$	$9.96[2] \cdot 10^3$	$477.2[3] \cdot 10^3$	$5.42[3] \cdot 10^3$
E_T^{miss}	$472[1] \cdot 10^3$	$9.88[2] \cdot 10^3$	$476.8[3] \cdot 10^3$	$1.28[2] \cdot 10^3$
b-jet requirement	$4.93[8] \cdot 10^3$	$2.57[1] \cdot 10^3$	$7.06[4] \cdot 10^3$	$1.06[1] \cdot 10^3$
$\cos\Delta\phi_{\mu\mu}$	$4.55[8] \cdot 10^3$	$2.36[1] \cdot 10^3$	$6.59[4] \cdot 10^3$	$8.7[1] \cdot 10^2$
$\sum p_T^{jet}$	$2.95[7] \cdot 10^3$	$1.423[7] \cdot 10^3$	$5.16[3] \cdot 10^3$	125[5]
$\Delta m\,(130\,\mathrm{GeV})$	$2[1] \cdot 10^1$	4.68[2]	–	12[1]
$\Delta m\,(150\,\mathrm{GeV})$	2.7[2]	1.68[1]	12[2]	9[1]
$\Delta m\,(200\,\mathrm{GeV})$	–	0.446[[5]	2.3[7]	3.4[8]

Table 4.7: *Cross-section* × *selection efficiency* for the dominant background processes in the > 0 b-jet analysis after each selection cut, scaled to $1\,\mathrm{fb}^{-1}$. The numbers in brackets represent the statistical error on the last digit. The Z+jets events have been simulated with ALPGEN, the inclusive Z samples with PYTHIA.

Cut	$Z\tau\tau + l$-jets	$Z\tau\tau + b$-jets	$Z\tau\tau\ incl$
no cut	$1.21 \cdot 10^6$	$20.2 \cdot 10^3$	$1.13 \cdot 10^6$
p_T, η	$12.2[2] \cdot 10^3$	$509[5]$	$11.4[1] \cdot 10^3$
ID quality	$11.2[2] \cdot 10^3$	$459[5]$	$10.5[1] \cdot 10^3$
isolation	$7.9[2] \cdot 10^3$	$170[3]$	$7.4[1] \cdot 10^3$
preselection	$2.39[8] \cdot 10^3$	$49[1]$	$2.50[7] \cdot 10^3$
E_T^{miss}	$2.28[8] \cdot 10^3$	$41[1]$	$2.40[7] \cdot 10^3$
b-jet requirement	$21[6]$	$8.8[6]$	$25[7]$
cos $\Delta\phi_{\mu\mu}$	$20[6]$	$8.5[6]$	$25[7]$
$\sum p_T^{jet}$	$17[6]$	$5.6[5]$	$15[5]$
Δm (130 GeV)	0	0	0
Δm (150 GeV)	0	0	0
Δm (200 GeV)	0	0	0

Table 4.8: *Cross-section* × *selection efficiency* for additional background processes in the > 0 b-jet analysis after each selection cut, scaled to $1\,\text{fb}^{-1}$. The numbers in brackets represent the statistical error on the last digit. The Z+jets events have been simulated with ALPGEN, the inclusive Z samples with PYTHIA.

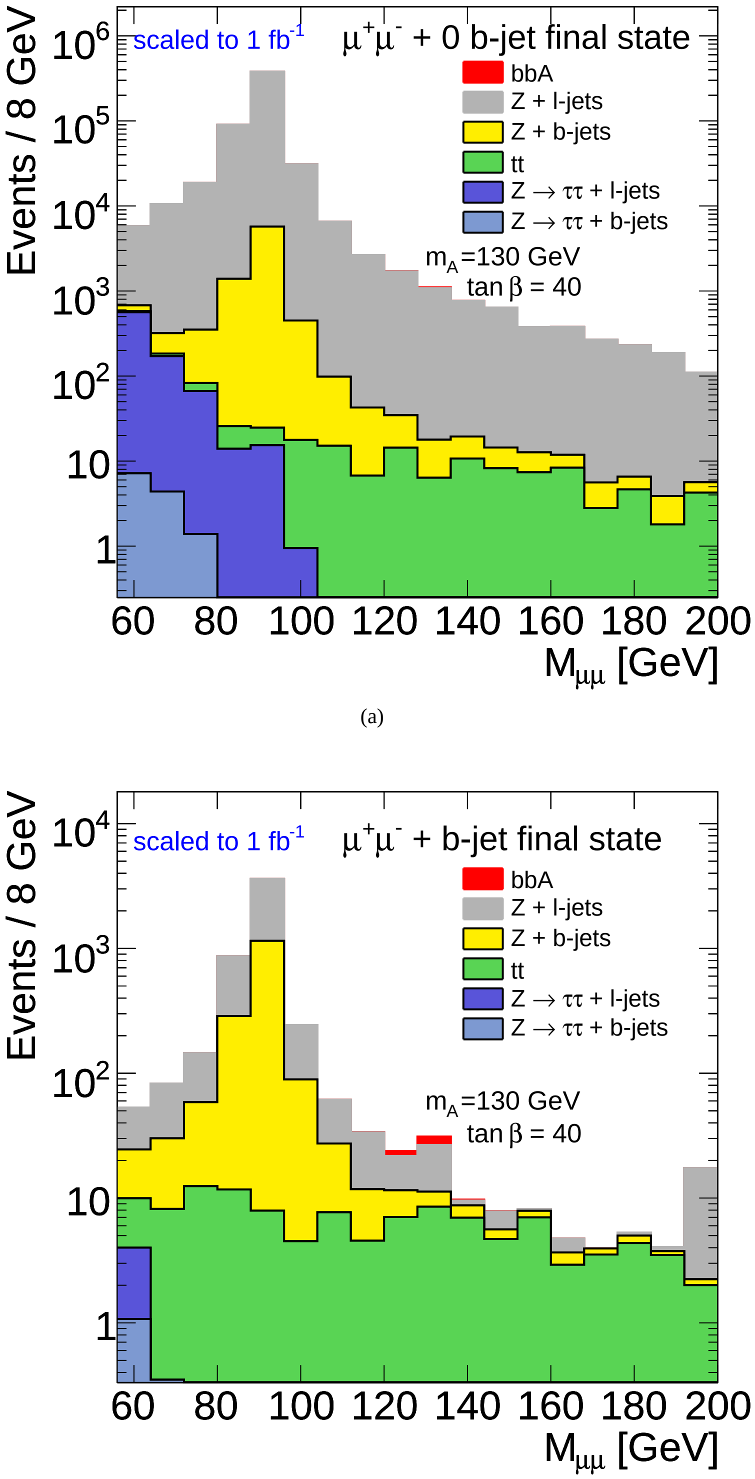

(a)

(b)

Figure 4.15: Dimuon invariant mass distribution for signal and background processes at an integrated luminosity of $1\,\text{fb}^{-1}$ after all analysis cuts for the 0 b-jet (a) and for the > 0 b-jet final state (b).

Chapter 5

Background Estimation from Control Data Samples

In this chapter a data-driven method for the background estimation from measured signal-free control data is presented. This method is based on a proposal in [35]. Control samples with ee and $e\mu$ final states are used to estimate the $\mu\mu$ background. Effects are studied which can spoil the equivalence between the different lepton flavour final states. The accuracy of the background estimation method is evaluated in the 0 b-jet and > 0 b-jet analysis channel for three different integrated luminosities of $4\,\text{fb}^{-1}$, $1\,\text{fb}^{-1}$ and $200\,\text{pb}^{-1}$.

5.1 The Method

In the previous chapter, the overwhelming background contribution on the $h/H/A \to \mu^+\mu^-$ signal was shown. The discovery potential in this channel depends critically on the systematic uncertainties in the expected background and a reliable background estimation is essential. The estimation of the background contribution from Monte Carlo predictions suffers from relatively large theoretical uncertainties on the production cross sections at the TeV scale as well as from the detector related systematic uncertainties (see Chapter 6). It is therefore preferable not to rely on background estimations from Monte Carlo. By evaluating the background from measured collision data sensitivity to theoretical uncertainties can be avoided and systematic uncertainties in the detector performance are cancelled out to a large extent.

A strategy to estimate the background from measured collision data is described in this chapter. The goal is to define control data samples which do not contain a signal contribution. The introduced background estimation method is based on three assumptions valid on particle level:

First, the $A \to e^+e^-$ decay is very unlikely and can be neglected compared to the signal process $A \to \mu^+\mu^-$ since it is suppressed by a factor of $m_\mu^2/m_e^2 \approx 40000$.

Secondly, because of the universality of the weak interaction the couplings of the electrons and muons to the Z boson are equal. Thus the branching ratios of the decays $Z \to \mu^+\mu^-$ and $Z \to e^+e^-$ are the same and since the electron and muon masses are negigible compared to the Z boson mass also the kinematic properties of both decays are equal. Therefore at particle level in the lowest order of the SM, the ee and $\mu\mu$ invariant mass distributions are identical. This argumentation is also valid for the other background processes such that the total $\mu\mu$ background contribution is at particle level equal to the contribution in the ee final state.

Finally since neither the Z nor the A boson decays into $e\mu$, this final state can be used to estimate the $t\bar{t}$ background. This is particularly usefull for the analysis with > 0 b-

jets where the $t\bar{t}$ background is no longer negligible but of similar magnitude as the Z background. For combinatorial reasons the decay $t\bar{t} \rightarrow e\mu + X$ is twice as frequently as $t\bar{t}$ decays into two electrons or two muons. Therefore, the $e\mu$ invariant mass distribution has to be scaled by a factor of 0.5 to correspond to the $\mu\mu$ final state.

By applying the same analysis cuts (see Section 4.5) to the three different final states ee, $e\mu$ and $\mu\mu$ one should be able to estimate the total $\mu\mu$ background from signal-free ee and $e\mu$ final states. This is however in general only correct at particle level. At reconstruction level several effects can lead to differences in the shape and the normalization of the invariant mass distribtions.

The analysis cuts applied in the event selection can cause such differences if the cut variables have different distributions for electrons and muons. To study the impact of the analysis cuts on ee and $\mu\mu$ final states, the distributions of the cut variables are compared for the inclusive Z and $t\bar{t}$ samples in the following.

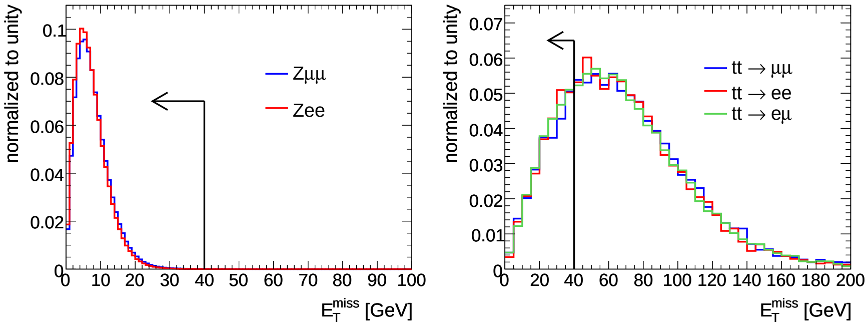

(a) (b)

Figure 5.1: Distribution of the missing transverse energy for events passing the preselection in inclusive Z (a) and $t\bar{t}$ events (b). The black line indicates the selection cuts.

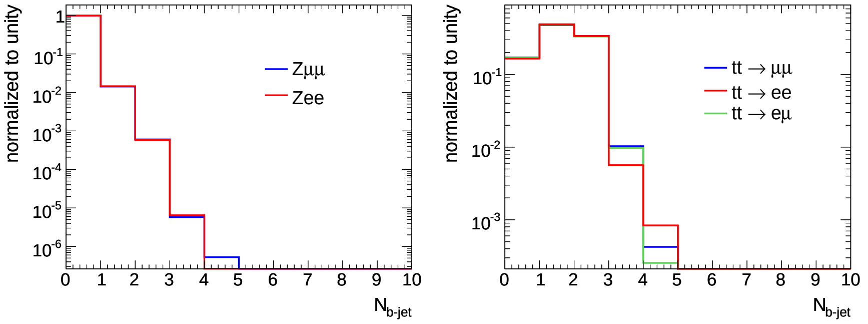

(a) (b)

Figure 5.2: The number of tagged b-jets per event after the preselection in inclusive Z (a) and $t\bar{t}$ events (b).

- The first cut applied after the preselection is the upper bound on the missing transverse energy. The E_T^{miss} distributions for inclusive Z and $t\bar{t}$ events that passed the preselection are shown in Fig. 5.1. The distributions for the different leptonic final states have identical shapes and therefore the E_T^{miss} cut causes no systematic degradation of the background estimation.

- In the next step, the analysis is divided into two branches according to the number of tagged b-jets. Fig. 5.2 shown that the numbers of b-jets per event after the preselection are in an excellent agreement between the different final states.

- Finally, two cuts are applied in the > 0 b-jet analysis which reduce mainly the $t\bar{t}$ contribution: the cuts on $\sum p_T^{jet}$ and $\Delta\phi_{ll}$. Also here, the distributions after the preselection are in excellent agreement as shown in Figs. 5.3 and 5.4.

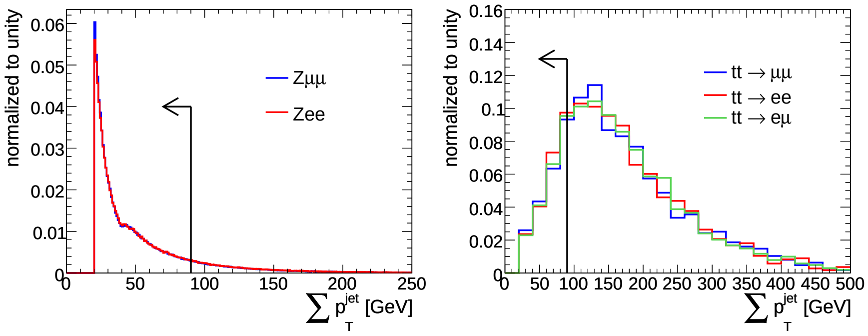

(a) (b)

Figure 5.3: Distribution of the sum over all jet transverse momenta after the preselection in inclusive Z (a) and $t\bar{t}$ events (b). The black lines indicate the selection cuts.

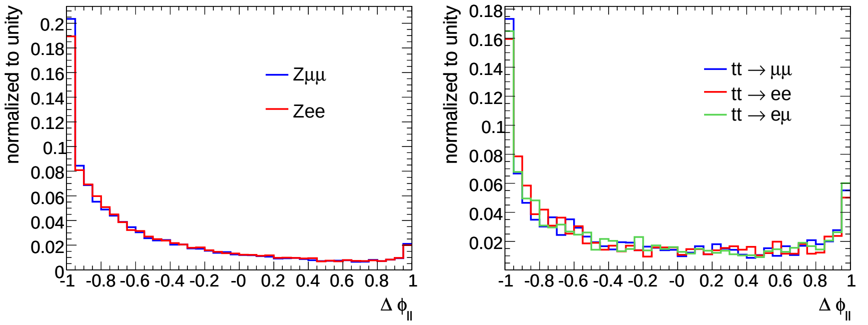

(a) (b)

Figure 5.4: Distribution of angle $\Delta\phi_{ll}$ between the two leptons after the preselection in inclusive Z (a) and $t\bar{t}$ events (b).

To conclude, the event selection as it is introduced in Section 4.5 performes equally for electron and muon final states. The only difference expected is due to differences in the reconstruction of electrons and muons. This will be studied in more detail in the following. Electron and muon events show different properties at the reconstruction level due to the following effects:

- Different momentum resolution for electrons and muons.

- Lower reconstruction efficiency for electrons than for muons.

- Higher energy losses of electrons due to higher probability of final state radiation and Bremsstrahlung.

These effects grouped into detector-related and intrinsic sources are studied in detail in the following. The purely detector-related effects are the momentum resolution and the reconstruction efficiency. These effects will be discussed in Section 5.3. The intrinsic effect is final state radiation which is discussed in the following section. In addition, the electrons and muons emit Bremsstrahlung due to the interaction of the charged particles with the detector material and the magnetic field of the tracking detectors. Since at reconstruction level one cannot distinguish between final state radiation and Bremsstrahlung these two effects are treated together in Section 5.2.2.

5.2 Impact of the Final State Radiation and Bremsstrahlung

In this section the effects of final state radiation (FSR) are discussed. FSR is the emission of a photon nearby the decay vertex (see Fig. 5.5) caused by higher order QED corrections. Such photons carry a fraction of the four-momentum of its mother lepton and therefore lower the reconstructed dilepton mass M_{ll}. This effect is particularly important for the Z background estimation, since the shape of the Z resonance can change significantly. The continuous dilepton distribution in the $t\bar{t}$ decays on the other hand remains rather unaffected. As an example the dielectron invariant mass distributions in $t\bar{t}$ and inclusive Z events are shown in Fig. 5.6 before and after the emission of FSR. According to this observation the study of FSR effects is in the following performed only for the $Z \to e^+e^-$ and $Z \to \mu^+\mu^-$ processes.

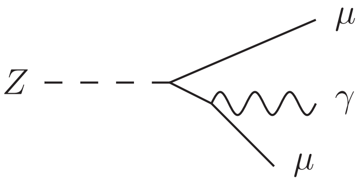

Figure 5.5: Feynman diagram for photon final state radiation in the $Z \to \mu^+\mu^-$ decay.

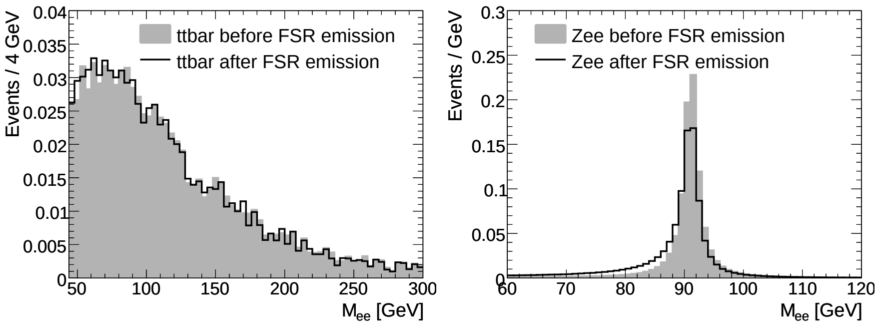

(a) (b)

Figure 5.6: Impact of final state radiation on the invariant dielectron mass distributions M_{ee} for the $t\bar{t}$ process (a) and for the inclusive $Z \to ee$ process (b).

Since for the reconstructed dilepton masses one cannot separate the FSR effects from Bremsstrahlung effects, we first study the FSR effects on the generator level, using the Monte Carlo truth information.

5.2.1 Final State Radiation at the Generator Level

As already mentioned, final state radiation is the emission of one or more photons (γ_{FSR}) close to the $Z \rightarrow l^+l^-$ vertex. Due to the difference between the electron and the muon mass, an electron will emit a photon with higher probability than a muon. Therefore one expects to have more FSR photons in the $Z \rightarrow ee$ process than in $Z \rightarrow \mu\mu$. Fig. 5.7 shows the distribution of the number of emitted photons per event in both data samples, as well as their transverse momentum distributions. The corresponding numbers of events with a given multiplicity of FSR photons are listed in Table 5.1. One observes that there are nearly twice as many events with at least one FSR photon in the $Z \rightarrow ee$ sample than in the $Z \rightarrow \mu\mu$ data.

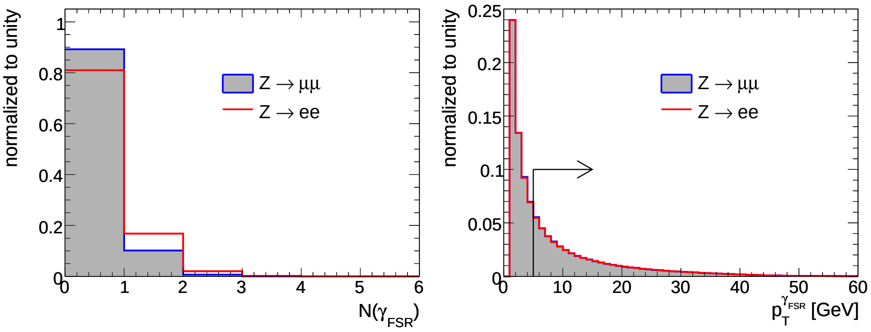

(a) (b)

Figure 5.7: Number of FSR photons (γ_{FSR}) in inclusive $Z \rightarrow ee$ and $Z \rightarrow \mu\mu$ events (a) and their p_T distributions (b).

	$Z \rightarrow e^+e^-$		$Z \rightarrow \mu^+\mu^-$	
	absolute	*relative*	*absolute*	*relative*
N_{total}	4547602	1.0	4547602	1.0
$N_\gamma = 0$	3683440	0.81	4056220	0.89
$N_\gamma = 1$	763699	0.17	460509	0.10
$N_\gamma = 2$	92232	0.020	29529	0.0065
$N_\gamma = 3$	7684	0.0017	1299	0.00029
$N_\gamma = 4$	526	0.00012	39	0.0000086
$N_\gamma > 4$	71	0.000016	6	0.0000013

Table 5.1: Number of $Z \rightarrow e^+e^-$ and $Z \rightarrow \mu^+\mu^-$ events with different FSR photons multiplicities on the generator level.

This leads to a clear difference between the invariant dilepton mass distributions in both cases. If the Z boson mass is determined from the lepton four-momenta before the emission of final state radiation their invariant mass distibutions are in excellent agreement, as shown in Fig. 5.8(a). This is not the case if the four-momenta after FSR emission are used for the Z mass calculation (see Fig. 5.8(b)). In the latter case the $Z \rightarrow e^+e^-$ peak is shifted to lower masses compared to the $Z \rightarrow \mu^+\mu^-$ peak.

The four-momenta of the FSR photons can be used to correct the dilepton invariant mass. As for the reconstructed leptons, also at generator level the leptons are required to pass a certain p_T-threshold. The p_T-cut has to be applied after the correction of the lepton four-momentum for the potential FSR photon emission. Otherwise the p_T-cut will introduce differences in the numbers of selected $Z \rightarrow ee$ and $Z \rightarrow \mu\mu$ events.

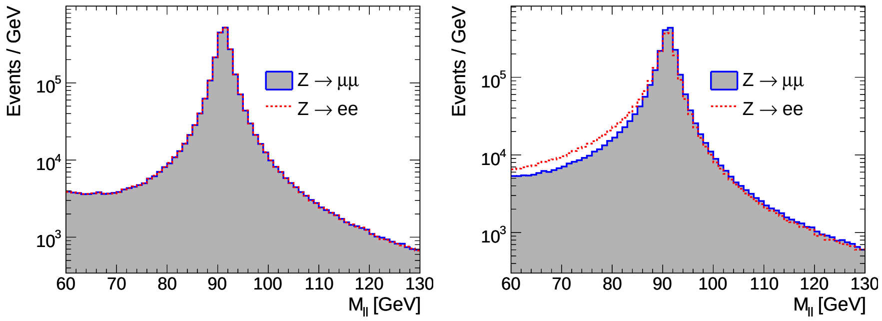

(a) (b)

Figure 5.8: Invariant dilepton mass distribution in $Z \to \mu\mu$ and $Z \to ee$ events obtained from lepton four-momenta at generator level before (a) and after (b) the potential emission of FSR photons.

A lepton originally passing the p_T-cut, may be rejected after the emission of a photon and thus the event would not be selected for the Z mass reconstruction. Since this would happen more frequently for electrons than for muons, the number of selected $Z \to ee$ events would be systematically lower than the number of $Z \to \mu\mu$ events. In oder to avoid this bias, the following strategy was chosen:

- A very loose p_T-cut of $5\,\text{GeV}$ is applied on the truth electrons and muons (see also 4.5.1) to minimize the bias on the p_T-cut selection efficiency due the FSR photon emission.
- The four-momentum correction is applied before the final state selection[1]. The momentum of the FSR photon is added to the momentum of the lepton from which it originated and the Z mass reconstruction is finally performed using leptons with corrected momenta.

The Monte Carlo truth information is not sufficient to identify the mother lepton of a FSR photon. One can only identify a given photon as a FSR photon originating from a particular $Z \to l^+l^-$ decay. Therefore an additional feature of final state radiation is used for the assignment to the mother lepton: FSR photons are emitted preferentially tangential to the trajectories of the leptons from which they originate. Thus the angluar distance ΔR between lepton and corresponding photon tends to be very small. Fig. 5.9(a) shows the ΔR distribution between a FSR photon and its nearest lepton. This motivates the choice of a ΔR cut for the identification of the mother lepton for a FSR photon. At Monte Carlo truth level a cut of $\Delta R(l, \gamma) < 0.5$ was chosen. The rate of misidentified mother leptons defined by this criterion is expected to be very low due to the fact that leptons from a Z decay tend to be emitted back-to-back (see Fig. 5.9(b)), i.e. they are well separated such that ambiguities in the photon assignment are small.

The FSR-corrected Z mass calculation is performed according to the above procedure. For the validation of the correction procedure it is useful to concentrate first on Z events in which at least one FSR photon was emitted (Fig 5.10 in contrast to Fig. 5.8 where all Z decays are indicated). Fig. 5.10 demonstrates an excellent performance of the FSR correction: the original shift to lower invariant masses is perfectly compensated resulting in a narrow Z resonance.

---

[1] The final state is selected at generator level by requiring two truth leptons with opposite charge and $p_T > 15\,\text{GeV}$, originating from a Z boson.

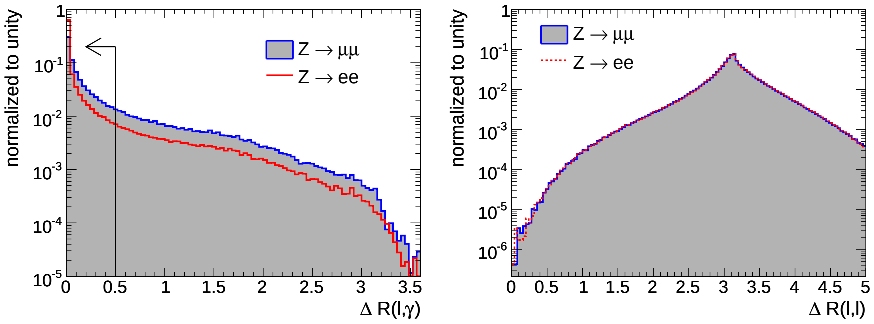

(a) (b)

Figure 5.9: Distributions of the angular distance ΔR between a FSR photon and the nearest lepton (a) and between the two leptons (b) originating from a Z boson decay.

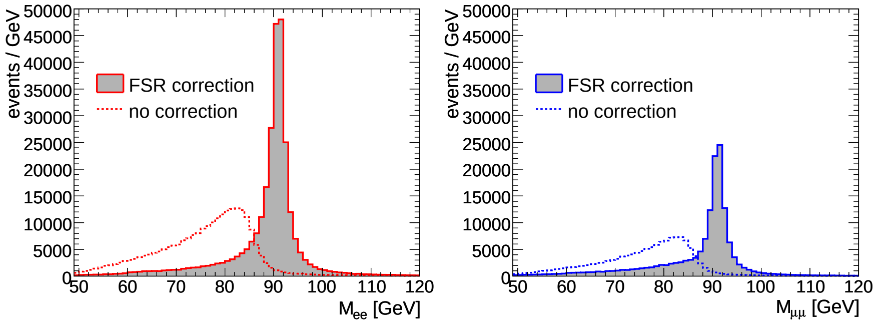

(a) (b)

Figure 5.10: Invariant mass distributions in $Z \rightarrow ee$ (a) and $Z \rightarrow \mu\mu$ events (b) with at least one FSR photon. The dashed lines correspond to the uncorrected masses, the full lines to the same masses after the FSR correction. The correction has been applied for FSR photons with $p_T > 5\,\text{GeV}$.

Effect of he p_T-cut on FSR Photons One aspect which should be mentioned here is the dependence of the performance of the FSR correction on the p_T-cut applied on the FSR photons. The transverse momentum distribution of FSR photons (Fig. 5.7) shows that the emitted photons tend to have a low p_T. However, the lowest energy for a photon cluster which can be reconstructed in the ATLAS calorimeter is $\sim 5\,\text{GeV}$. To evaluate the FSR correction in a realistic scenario, a cut of $p_T^\gamma > 5\,\text{GeV}$ is applied also at generator level. This on the other hand implies that already by applying this relatively low cut a large fraction of FSR photons is not taken into account which consequently degrades the quality of the correction. To test the impact of the photon p_T cut, the FSR correction using the photons with $p_T^\gamma > 5\,\text{GeV}$ is compared to the correction using all photons included in the generator output having an intrinsic cut fo $p_T^\gamma > 1\,\text{GeV}$. In Fig. 5.11 the corrected invariant mass distributions with the two different p_T^γ cuts ($1\,\text{GeV}$ and $5\,\text{GeV}$) are compared to the distributions without correction and to the distributions obtained from the lepton four-momenta before the emission of FSR.

Closing the studies of FSR correction on generator level the results for $Z \rightarrow e^+e^-$ and $Z \rightarrow \mu^+\mu^-$ are compared quantitatively in Fig. 5.12. Fig. 5.12(a) shows the ratio of the dielectron and dimuon invariant mass distributions before FSR emission. Figs. 5.12(b), 5.12(d) and 5.12(c) show the same ratio after FSR emission, without FSR correction and

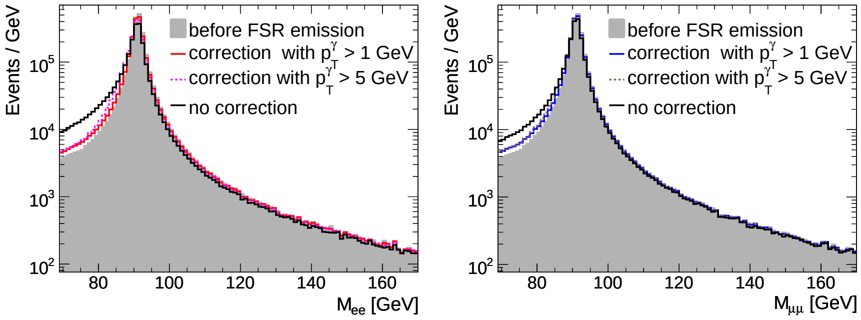

(a) (b)

Figure 5.11: Effect of the photon transverse momentum cut on the FSR correction for $Z \to ee$ (a) and $Z \to \mu\mu$ dilepton mass distributions (b).

with FSR correction for the different p_T^γ cuts. Fig. 5.12(a) shows perfect agreement between the ee and $\mu\mu$ distributions in the absence of final state radiation. Two effects are visible in Fig. 5.12(b): The emission of photons distortes the ratio most notably in the mass region around the Z resonance and also shiftes the ratio to lower values in the high invariant mass region. This shift is already corrected for if FSR photons with $p_T^\gamma > 5\,\text{GeV}$ are taken into account (see Fig. 5.12(c)). By including all FSR photons with $p_T^\gamma > 1\,\text{GeV}$ in the correction (Fig. 5.12(d)) also the remaining distortion around the Z resonance can be corrected with high accuracy.

5.2.2 FSR and Bremsstrahlung on the Reconstruction Level

After the tests on the generator level, we now consider the more realistic case after event reconstruction in the detector. At reconstruction level one cannot distinguish between photons emitted as final state radiation or as Bremsstrahlung due to interactions with the detector material. This does not cause a problem since the two effects have the same consequences: in both cases the invariant mass of the reconstructed lepton pair is shifted to lower values.

As reminder, the identification of final state radiation photons at the Monte Carlo truth level was performed in two steps: First a FSR photon was identified as a photon originating from a Z boson based on the Monte Carlo truth information. Subsequently, this photon was linked to its mother lepton by requiring a small angular distance ΔR between photon and lepton.

Since both final state radiation and Bremsstrahlung photons are expected to be close to the mother lepton, the selection with a ΔR cut can also be performed at reconstruction level. A tighter ΔR cut value, however, is chosen here in order to reduce the contribution of background photons which are additional reconstructed photons not originating from the leptons in the Z decay. At the reconstruction level a photon is identified as FSR/Bremsstrahlung photon if its angular distance to a lepton is $\Delta R < 0.25$.

Prior to the tests of the FSR photon selection at the reconstruction level, some attention has to be payed to photon reconstruction in the ATLAS detector. In Fig. 5.13 the transverse momentum distribution of all reconstructed photons is shown in comparision to the one of all truth photons leading to two observations: Firstly, the total number of reconstructed photons is much lower than the number of truth photons, in particular for low transverse momenta. Secondly, since no quality cuts on the photon reconstruction have been applied here, there is a large contribution of fake photons in the $Z \to ee$ events arising from electrons misidentified as photons. Since in general very few photons are reconstucted, a

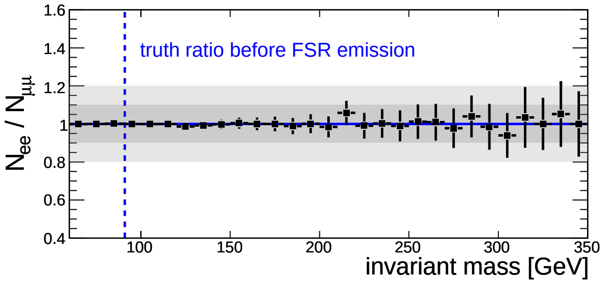

(a) Ratio before FSR emission.

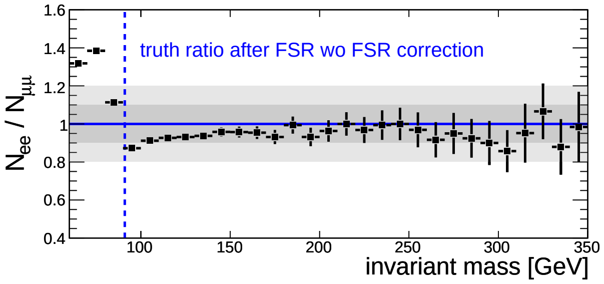

(b) Uncorrected ratio after FSR emission.

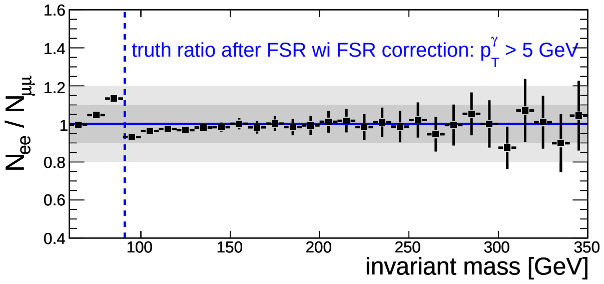

(c) FSR corrected ratio using $p_T^{\gamma} > 5\,\mathrm{GeV}$.

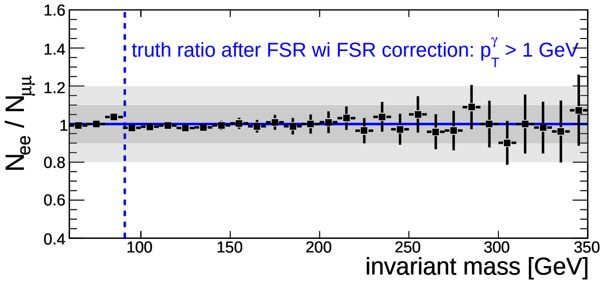

(d) FSR corrected ratio using $p_T^{\gamma} > 1\,\mathrm{GeV}$.

Figure 5.12: Ratio of the $Z \rightarrow ee$ and $Z \rightarrow \mu\mu$ invariant mass distributions at the generator level. The location of the Z resonance is indicated by the dashed line. The grey bands indicate $10\,\%$ and $20\,\%$ variations of the ratio around 1.

photon quality requirement has not been applied in the following.

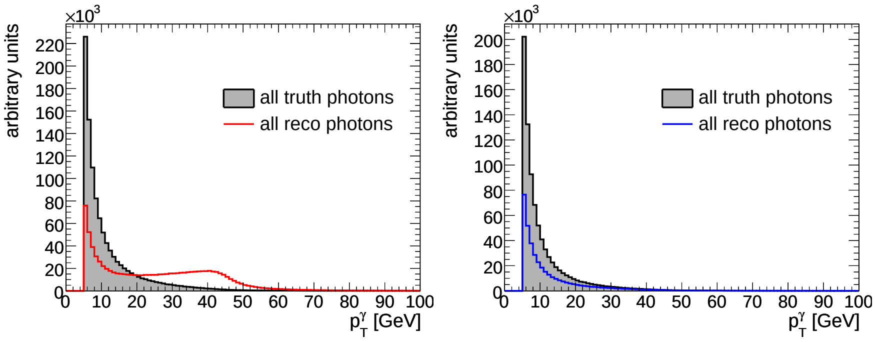

(a) (b)

Figure 5.13: Distributions of the transverse momenta of all photons at truth and at reconstruction level in $Z \to ee$ (a) and $Z \to \mu\mu$ (b) events.

To illustrate the impact of the (in total low number of) reconstructed photons on the performance of the FSR selection, the ΔR distributions of all truth photons, truth FSR photons and reconstructed photons are shown in Fig. 5.14. In the $Z \to \mu\mu$ events, the number of reconstructed photons close to a muon is roughly one order of magnitude lower compared to the truth. This is even worse in the $Z \to ee$ sample were for $\Delta R < 0.15$ almost no photons are reconstructed. A possible explanation is if electron and photon are very close their showers in the electromagnetic calorimeter are overlapping and cannot be separated. Due to the presence of a track in the inner detector an electron is reconstructed but its energy is measured without adding the complete photon cluster to the electron cluster. This is not the case in the region $\Delta R > 0.15$, thus the distribution is similar to the one for $Z\mu\mu$ events. The multiplicity of reconstructed photons selected as radiation from leptons is shown in Table 5.2.

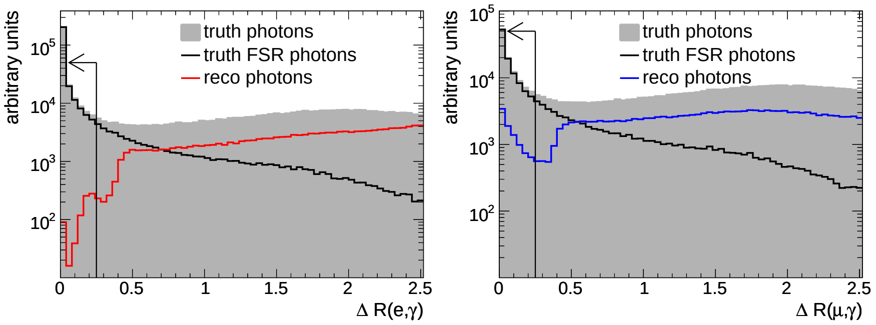

(a) (b)

Figure 5.14: Distibution of the angular distance ΔR between photons and the closest lepton at truth and reconstruction level in $Z \to ee$ (a) and $Z \to \mu\mu$ events (b).

In spite of the low reconstruction efficiency, the photons can be used to probe the FSR/Bremsstrahlung correction at reconstruction level. To validate the correction procedure, only the small fraction of events with at least one reconstructed FSR photon are taken into account. The resulting dilepton mass distributions before and after corrections are shown in Fig. 5.15 demonstrating a significant improvement of the dilepton mass due to the correction. The correction is more accurate for $Z \to \mu\mu$ events due to higher statistics available and because of the lower fake photon contribution compared to $Z \to ee$ events.

	$Z \to e^+e^-$	$Z \to \mu^+\mu^-$
N_{total}	4547602	4547602
$N_\gamma = 0$	4546761	4538465
$N_\gamma = 1$	827	9066
$N_\gamma = 2$	14	70
$N_\gamma = 3$	0	1

Table 5.2: Number of FSR photons at reconstruction level, i.e. defined with $\Delta R(l, \gamma) < 0.25$.

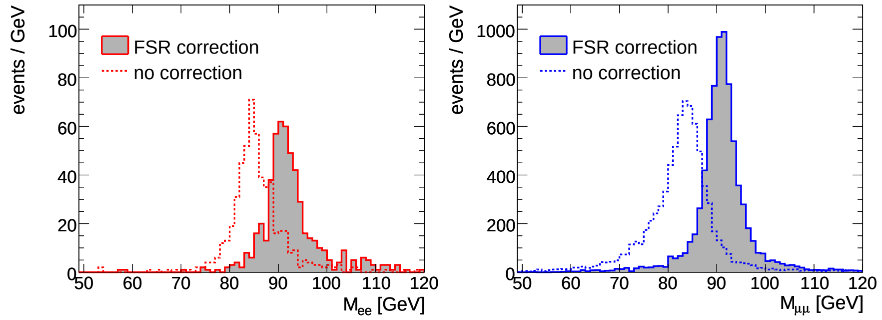

(a) (b)

Figure 5.15: Dilepton invariant mass distributions for $Z \to ee$ (a) and $Z \to \mu\mu$ (b) events with at least one reconstructed FSR photon identified with $\Delta R(l, \gamma) < 0.25$. The dashed lines represent the mass distributions before FSR correction, the full lines show the same events after the FSR correction.

In conclusion, the method for correcting the FSR/Bremsstrahlung effects performes well also on the reconstruction level. However, the correction procedure does not help to improve the Z mass reconstruction because of the low reconstruction efficiency of photons close to leptons.

5.3 Detector-Related Effects on the Lepton Reconstruction

In this section two further effects expected to degrade the invariant mass distributions and therefore the achievable accuracy of the background estimation are discussed. Both effects appear due to the different detector response and reconstruction performance for electrons and muons.

5.3.1 Lepton Momentum Resolution

The performance of the ATLAS detector in terms of the momentum resolution for electrons and muons has already been discussed in Section 4.4. Since electron and muon momentum resolution show different p_T-dependence, a distortion of the $^{N_{ee}}/_{N_{\mu\mu}}$ ratio is expected. The limited momentum resolution in general smears the invariant mass distribution. Related to the main backgrounds for the $h/H/A \to \mu^+\mu^-$ channel, the impact of the limited resolution affects the Z background to a much larger extent than the flat mass distribution of the $t\bar{t}$ background. Therefore, the inclusive $Z \to ee$ and $Z \to \mu\mu$ events are used to study this effect.

The reconstructed ${}^{N_{ee}}/_{N_{\mu\mu}}$ ratio cannot be easily corrected for the difference in the momentum resolution. Therefore, we first study this effect on the Monte Carlo truth level by smearing the truth lepton momenta according to the resolution curves in Fig. 4.5.

The truth four-momenta of the electrons and muons are smeared randomly according to a Gaussian probability distribution with the width given by the observed resolution. This procedure is performed in bins of p_T since the resolutions strongly depend on this variable. To validate the smearing procedure, the resolution is calculated for the smeared truth momenta and compared to the resolution for reconstructed leptons. Fig. 5.16 shows an excellent agreement between the accual observed resolution curves and the resolution obtaind from the smeared momenta.

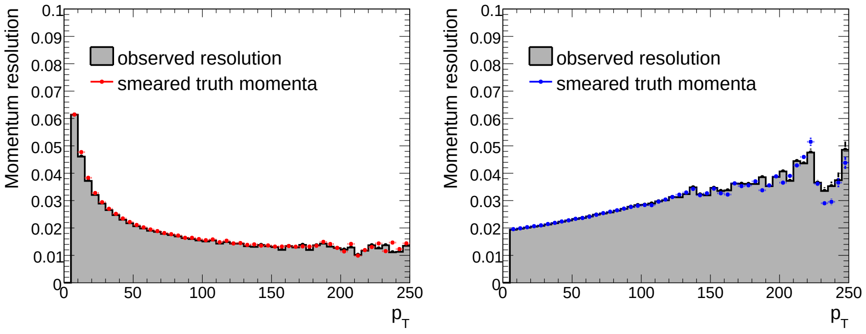

(a) (b)

Figure 5.16: Electron (a) and muon (b) momentum resolutions obtained from the smeared truth four-momenta in comparison with the observed momentum resolutions.

Finally, the Z boson mass is reconstructed from the smeared truth momenta. In Fig. 5.17 the ratios of the ee and $\mu\mu$ invariant mass distributions are shown as obtained from the accual truth lepton momenta (black dots) and for smeared truth lepton momenta (red dots). No FSR correction was applied. Very good agreement is observed between both ratios. A very small deviation is observed only at the Z peak.

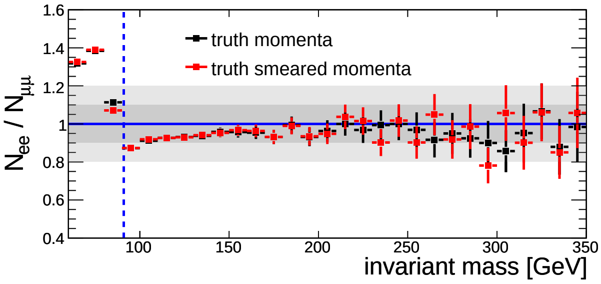

Figure 5.17: ${}^{N_{ee}}/_{N_{\mu\mu}}$ ratios of the ee and $\mu\mu$ invariant mass distributions determined for truth lepton four-momenta (black marks) and truth lepton four-momenta smeared with the observed resolution (red marks).

Due to the vanishing impact of the different momentum resolutions for electrons and muons in particular at high invariant masses the effect of the resolution on the quality of the background estimation can be neglected. Thus this effect is not taken into account for further studies.

5.3.2 Reconstruction Efficiencies

The last effect which is discussed in the context of changes on the dilepton invariant mass distribution is caused by different reconstruction efficiencies for electrons and muons. As shown in Fig. 4.3 the overall reconstruction efficiency of electrons is roughly $20\,\%$ lower than the muon efficiency. This needs to be taken into account in the normalization of the ee and $\mu\mu$ mass distributions.

The event selection for the $h/H/A \rightarrow \mu^+\mu^-$ analysis introduced in Section 4.5 requires that the leptons pass isolation criteria. Since the isolation variables for electrons and muons are in general not equal, also the efficiency of the isolation requirement has to be taken into account. The relevant reconstruction efficiency for this case is given by

$$\begin{aligned} \varepsilon_{muon} &= \frac{N^{matched}_{comb,\,iso\,muon}}{N^{truth}_{muon}}, \\ \varepsilon_{elec} &= \frac{N^{matched}_{medium,\,iso\,elec}}{N^{truth}_{elec}}, \end{aligned} \tag{5.1}$$

where *combined isolated* muons and *medium isolated* electrons have been matched to truth muons and electrons according to the procedure described in Section 4.4. The reconstruction efficiency defined in this way can be measured with collision data in inclusive Z events, using the so-called tag-and-probe method without the need to rely on Monte Carlo simulation [20]. The reconstruction efficiencies are used to weight the reconstructed masses of the dilepton pairs. In this way the invariant mass distributions are corrected for the different detector acceptances $\mathcal{A}$ which relate the number of generated events $N_{generated}$ with the number of measured events $N_{measured}$ via:

$$N_{measured} = \mathcal{L} \cdot \sigma \cdot \mathcal{A} = N_{generated} \cdot \mathcal{A}, \tag{5.2}$$

where $\mathcal{L}$ is the integrated luminosity and σ is the cross section for the signal process.
Fig. 4.3 shows a very uniform distribution of efficiencies in bins of ϕ while they strongly depend on η and p_T. Therefore the efficiencies used for the re-scaling procedure are parametrized in two-dimensonal (p_T, η) bins (see Fig. 5.18). Using this parametrization, every reconstructed lepton pair $(l_1(p_{T1}, \eta_1),\, l_2(p_{T2}, \eta_2))$ which passes the event selection is weighted with the inverse detector acceptance, given by

$$\frac{1}{\mathcal{A}} = \frac{1}{\varepsilon_1(p_{T1}, \eta_1)} \times \frac{1}{\varepsilon_2(p_{T2}, \eta_2)}. \tag{5.3}$$

If the lepton momentum is larger than $110\,\mathrm{GeV}$, the last p_T-bin is used for the weighting since there is not enough statistics available for measuring the efficiency of high-p_T leptons. The ${}^{N_{ee}}\!/_{N_{\mu\mu}}$ ratios for the invariant mass distributions in the inclusive Z events before and after the re-scaling for the efficiency are shown in Fig. 5.19. The correction clearly improves the agreement in the relative normalization of the two mass distributions. Thus, the results of all further studies at reconstruction level shown in the following are scaled according to the described efficiency correction.

5.4 Background Estimation on the Monte Carlo Truth Level

This and the following section deal with the performance of the background estimation for the $h/H/A \rightarrow \mu^+\mu^-$ analysis by means of signal-free control data samples consisting of ee and $e\mu$ final states. As already mentioned the two dominant backgrounds, Z and $t\bar{t}$ production, are considered for this study. In this section the background estimation

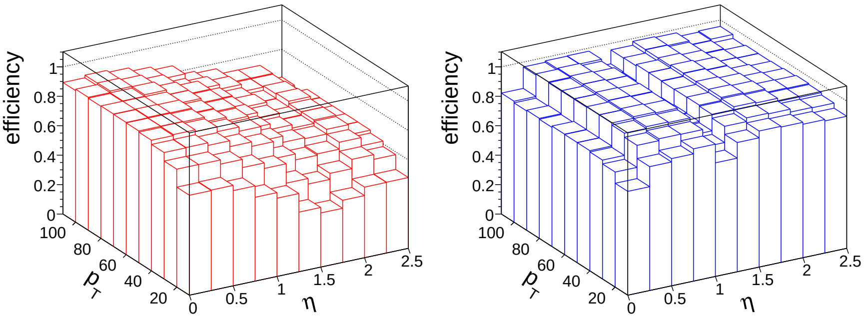

(a) (b)

Figure 5.18: Electron (a) and muon (b) reconstruction efficiencies for medium isolated electrons and combined isolated muons parametrized in bins of (p_T, η).

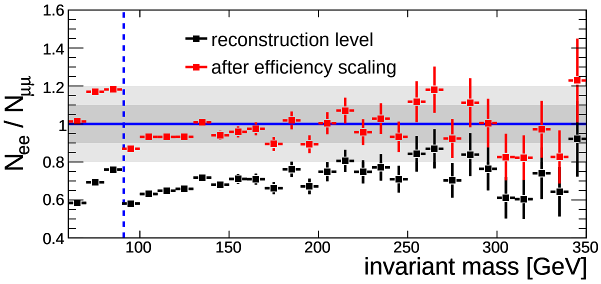

Figure 5.19: $N_{ee}/N_{\mu\mu}$ ratios of the invariant mass distributions for reconstructed dilepton pairs before (black marks) and after (red marks) the correction for the electron and muon reconstruction efficiencies.

is performed with the maximal available Monte Carlo statistics at the Monte Carlo truth level, in order to evaluate the highest achievable accuracy of the method. The Z+jets data samples generated with ALPGEN correspond to only $\sim 200\,\text{pb}^{-1}$. Therefore, the inclusive Z data samples generated with PYTHIA corrsponding to $\sim 4\,\text{fb}^{-1}$ of integrated luminosity are used.

As shown in Fig. 5.12(a) the ee and $\mu\mu$ invariant mass distributions obtained after preselection cuts are in perfect agreement at particle level. This is not the case at reconstruction level due to the effects described in Section 5.1. At the truth level, the only effect which degrades the agreement between the invariant mass distributions is the final state radiation. Although this can be corrected for at the truth level, such correction cannot be applied at reconstruction level. Therefore the FSR effects are not corrected in this section.

In the following, the total $\mu\mu$ background after all analysis cuts is estimated from the ee control samples and for the b-jet final state additionally the $t\bar{t}$ background is estimated from the $e\mu$ control sample. For comparison of the invariant mass distributions their ratios $N_{ee}/N_{\mu\mu}$ and $N_{e\mu}/N_{\mu\mu}$ are used. The accuracy of the method is evaluated by fitting a constant function (p_0) in the invariant mass range between $120 - 200\,\text{GeV}$ to the ratios. The accuracy on the background normalization is then given by $1 - p_0$ and the describtion of the background shape is evaluated by the relative error σ_{p_0}/p_0 from the fit.

At reconstruction level, the division to two different final states with zero and at least one reconstructed b-jet are discriminated with the b-tagging algorithm in combination with the event preselection which requires two reconstructed leptons in the final state. For the studies at truth level, we still use the reconstructed b-jets to distinguish the two final states. Only the leptons are taken from the truth level. The use of true b-jets for the separation of the two

final states is not comparable to the reconstrution level since it does not take into account the contribution of light jets misidentified as b-jets. In order to avoid the contribution of fake b-jets originating from electrons, all b-jets overlapping with a truth electron have been removed.
Finally the cuts for $t\bar{t}$ rejection, i.e. the lepton opening angle and the sum of all jet transverse momenta have not been applied at the truth level.

5.4.1 The 0 b-jet Analysis

The analysis mode without reconstructed b-jets in the final state is characterized by the dominant contribution of the irreducible Z background which cannot be rejected by any selection criterion. This leads to a large number of events in both the $\mu\mu$ background distribution and the ee control sample and therefore small statistical uncertainty.
The quality of the control sample is shown in Fig. 5.20. For an integrated luminosity of $4\,\text{fb}^{-1}$ the normalization of the total background can be predicted with an accuracy of $5.5\,\%$ at truth level and the shape can be estimated with an accuracy of better than $1\,\%$. This high accuracy can be achieved because of the high statistics of the Z background events in this final state as can be seen from the $^{N_{ee}}/_{N_{\mu\mu}}$ ratio for the Z background alone.

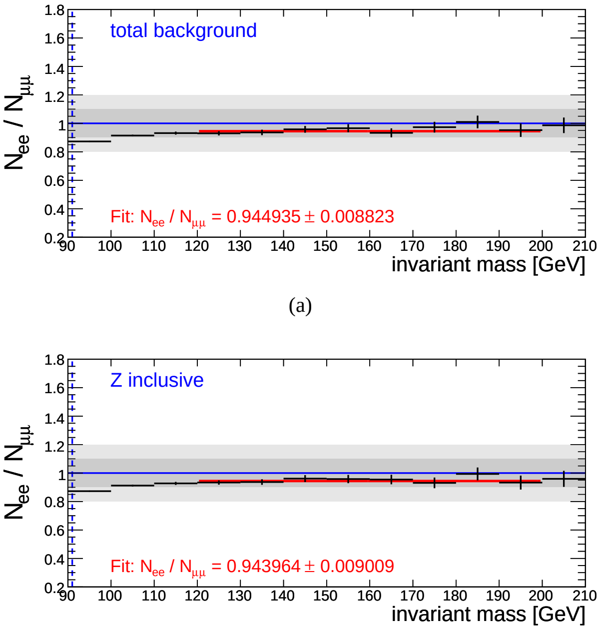

(a)

(b)

Figure 5.20: $^{N_{ee}}/_{N_{\mu\mu}}$ ratios for the total background (a) and the Z background alone (b) for the 0 b-jet final state at the Monte Carlo truth level for $4\,\text{fb}^{-1}$.

5.4.2 The b-jet Analysis

In the analysis mode were at least one reconstructed b-jet is required in the final state the $t\bar{t}$ background dominates if no cuts on the lepton opening angle and jet activity are applied. In this case two control samples are relevant, the ee control sample for the estimation of the total background and the $e\mu$ control sample for the estimation of the $t\bar{t}$ contribution alone. The comparison of the control samples to the $\mu\mu$ background is shown in Fig. 5.21. With $4\,\text{fb}^{-1}$ the total background can be estimated at truth level with an accuracy of $\sim 9\,\%$ on the normalization and less than $2.5\,\%$ on the background shape.

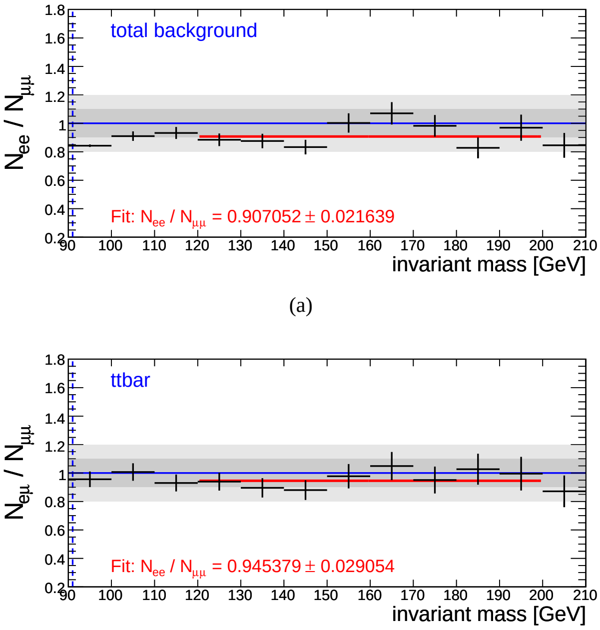

(a)

(b)

Figure 5.21: ${}^{N_{ee}}/_{N_{\mu\mu}}$ ratios for the total background (a) and the ${}^{N_{e\mu}}/_{N_{\mu\mu}}$ ratio for the $t\bar{t}$ background (b) for the b-jet final state at the Monte Carlo truth level for $4\,\text{fb}^{-1}$.

Additionally the normalization of the $t\bar{t}$ background can be estimated with $5.5\,\%$ and the shape with a $\sim 3\,\%$ accuracy.

5.5 Background Estimation on Reconstruction Level

At the Mone Carlo truth level the background can be estimated from control samples with high accuracy. Therefore, this method is expected to perform well also on the reconstruction level. Nevertheless, there are several detector effects which degrade the accuracy of the background estimation:

- Although the correction for the different lepton efficiencies introduced in Section 5.3 improves the agreement between the ee and $\mu\mu$ mass distributions, the accuracy of the corrections is limited by the accuracy for the measurement of the lepton efficiencies. This will be demonstrated in Section 5.6.

- Furthermore, the energy losses due to FSR and Bremsstrahlung which are larger for electrons than for muons cannot be corrected at reconstruction level. This is expected to cause a major degradation of the accuracy of the background estimation, which can be estimated from the difference between Figures 5.12(a) and 5.12(b). At reconstruction level, the observable effect is expected to be enhanced by the additional emission of Bremsstrahlung in the detector material.

- Some of the cut selection criteria have a significant impact on the quality of the background estimation. In the final state with > 0 b-jets three cuts are applied which strongly reject the $t\bar{t}$ contribution: the E_T^{miss}, $\sum p_T^{jet}$ and $\Delta\Phi_{ll}$ cuts. As shown in Table 4.6, the $t\bar{t}$ background is dominant for the > 0 b-jet final state selection before the three cuts. After these cuts $t\bar{t}$ is suppressed to the level of Z background.

The selection of the $\mu\mu$, the ee and the $e\mu$ final states has been introduced in Section 4.5. The invariant mass distribtutions in both analysis branches are shown in Figs. 5.22 and 5.23 obtained from the total available Monte Carlo statistics and scaled to an integrated luminosity of $1\,\mathrm{fb}^{-1}$.

The performance of the background estimation from control samples is evaluated for three data subsamples corresponding to integrated luminosities of 4, 1 and $0.2\,\mathrm{fb}^{-1}$. The first case probes the accuracy of the method with full available Monte Carlo statistics. The latter two subsamples of $1\,\mathrm{fb}^{-1}$ and $200\,\mathrm{pb}^{-1}$ give information about the performance in early data. $Z \to l^+l^-$ data for $4\,\mathrm{fb}^{-1}$ and $1\,\mathrm{fb}^{-1}$ are only available in the inclusive PYTHIA Z samples. For $200\,\mathrm{pb}^{-1}$ the Z background is represented by the ALPGEN $Z+l$-jets and $Z+b$-jets samples which contain a more realistic jet environment.

5.5.1 Accuracy with $4\,\mathrm{fb}^{-1}$ Integrated Luminosity

For the 0 b-jet final state enough data is available to achieve an accurate background estimation for $4\,\mathrm{fb}^{-1}$. As shown in Fig. 5.24 the normalization and the shape of the $\mu\mu$ background can be estimated with accuracies of $\sim 5\,\%$ and less than $1\,\%$, respectively. This is very close to the accuracy obtained on the truth level.
In the b-jet analysis already for $4\,\mathrm{fb}^{-1}$ a clear degradation with respect to the truth results occurs due to the lower statistics after the cuts on $\sum p_T^{jet}$ and $\Delta\phi_{ll}$. An accuracy of $15\,\%$ on the normalization and of $7\,\%$ on the shape of the total background can be achieved. The $t\bar{t}$ background can be estimated from the $e\mu$ control sample with an accuracy of $16\,\%$ on the normalization and only $17\,\%$ on the shape.

5.5.2 Accuracy with $1\,\mathrm{fb}^{-1}$

For an integrated luminosity of $1\,\mathrm{fb}^{-1}$, the Z background is still large enough to provide good statistics in the 0 b-jet final state (see Fig. 5.26). Therefore the normalization of the total background in this analysis mode can be estimated with an accuracy of $\sim 6\,\%$. For the background shape an accuracy of better than $2\,\%$ can be achieved.
In the b-jet analysis, as shown in Fig. 5.27, statistical limitations become more critical than for $4\,\mathrm{fb}^{-1}$. The normalization of the ee control sample is within $16\,\%$ in agreement with the total $\mu\mu$ background whereas the shape can only be estimated with $\sim 19\,\%$ accuracy. The $t\bar{t}$ background normalization can be estimated from the $e\mu$ control sample with only $45\,\%$ and the shape with only $\sim 50\,\%$ accuracy. Thus, the evaluated accuracy for the control samples for the > 0 b-jet analysis is not reliable for integrated luminosities below $1\,\mathrm{fb}^{-1}$ if all analysis cuts described in section 4.5 are applied.

5.5.3 Accuracy with $200\,\mathrm{pb}^{-1}$

The results for the agreement of the ee control sample with the total muon background for $200\,\mathrm{pb}^{-1}$ are shown in Fig 5.28. In the 0 b-jet final state the normalization of the background can be estimated with $\sim 7\,\%$ and the shape with better than $5\,\%$ accuracy. For the b-jet final state it is not reasonable to specify a result since the statistical fluctuations are dominating the ${}^{N_{ee}}/_{N_{\mu\mu}}$ ratio and a stable fit is not possible.

In conclusion, the background estimation from control samples achieves very promising results for the 0 b-jet analysis. Even at low integrated luminosities of $200\,\mathrm{pb}^{-1}$ accurate and stable results are achieved in the estimation of the total muon background due to the large number of Z events remaining after the event selection criteria.
The final state with at least one b-jet is more difficult. The $t\bar{t}$ background would be dominant in this analysis mode if no cuts on $\sum p_T^{jet}$ and $\Delta\phi_{ll}$ would be applied. These cuts significantly reduce a large fraction of the $t\bar{t}$ contribution. This results in a ~ 100 times

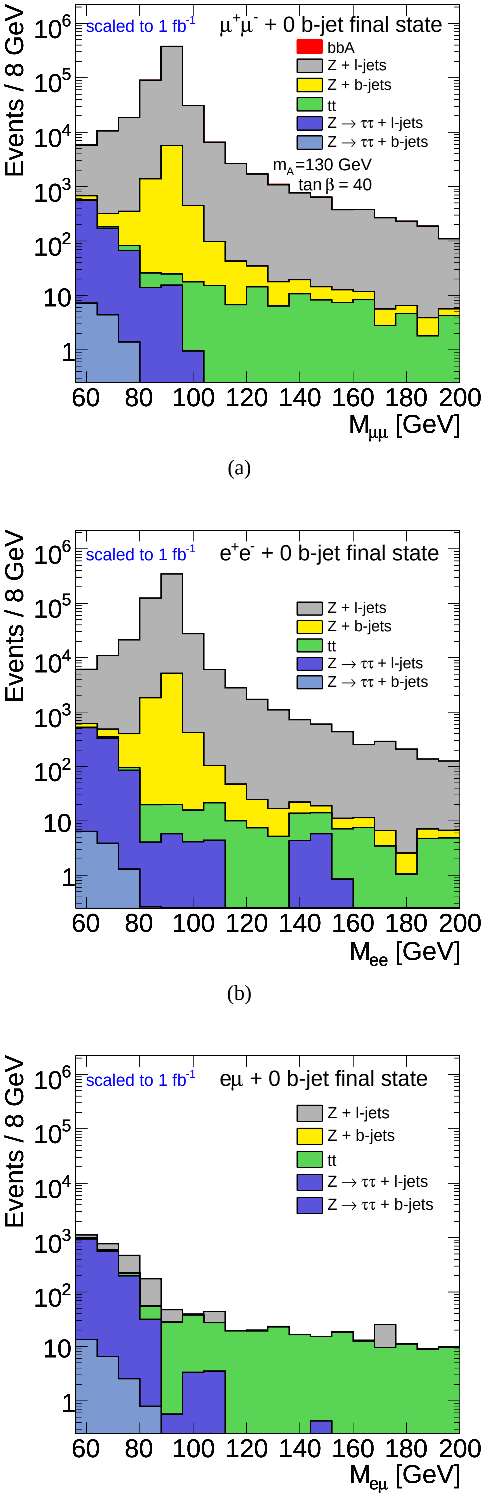

(a)

(b)

(c)

Figure 5.22: Reconstructed dilepton invariant mass distributions for the $\mu\mu$ (a), ee (b) and $e\mu$ (c) final states, obtained after the selection criteria of the 0 b-jet analysis.

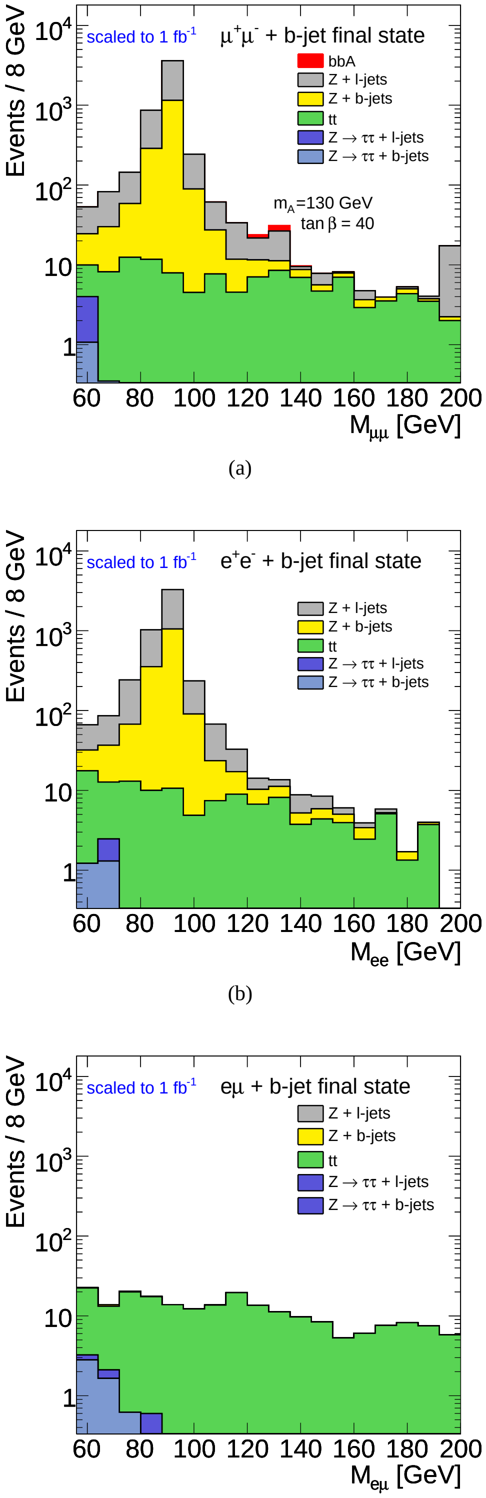

(a)

(b)

(c)

Figure 5.23: Reconstructed dilepton invariant mass distributions in the $\mu\mu$ (a), ee (b) and $e\mu$ (c) final state, obtained after the selection criteria of the > 0 b-jet analysis.

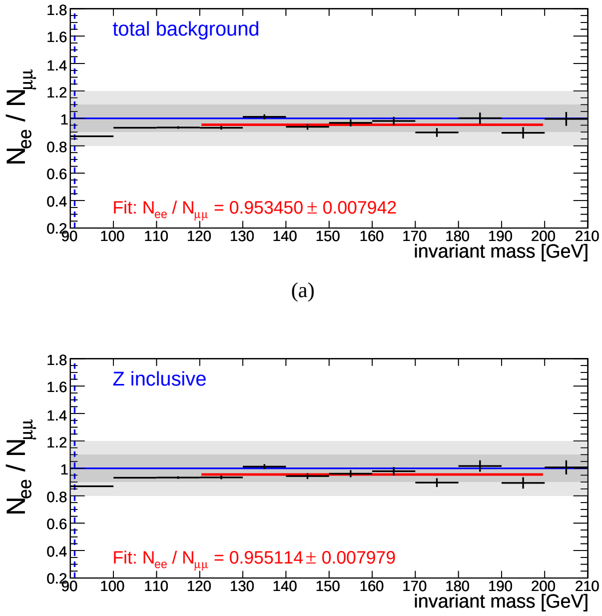

(a)

(b)

Figure 5.24: Ratio of the dilepton invariant mass distributions for the ee control sample and the total $\mu\mu$ background (a) obtained in the 0 b-jet final state at $4\,\mathrm{fb}^{-1}$. For comparison the dominant contribution from the Z sample (b) is shown in addition.

lower statistics compared to the 0 b-jet analysis which makes it difficult to establish reliable control data samples for the background estimation, even with an integrated luminosity of $4\,\mathrm{fb}^{-1}$.

Nevertheless the study on the Monte Carlo truth level without the $\sum p_T^{jet}$ and $\Delta\phi_{ll}$ cuts showed also a very promising result for this analysis branch and therefore alternative control samples are tested in Section 5.6 for a > 0 b-jet analysis without the cut on the sum of the jet transverse momenta $\sum p_T^{jet}$.

An overview of all obtained results on the accuracy of the background estimation from control samples in this section is given in Table 5.4 at the end of this chapter.

5.6 Background Estimation with Modified Event Selection

As mentioned above, the $t\bar{t}$ background would be the dominating contribution in the b-jet analysis. Therefore two additional cuts are applied in this analysis branch which reject this background very efficiently. Table 4.6 shows the cut evolution in the b-jet analysis. The $t\bar{t}$ selection efficiency of the $\cos\Delta\phi_{ll}$ cut is $82\,\%$ and only $14\,\%$ for the $\sum p_T^{jet}$ cut.

The previous section showed that the b-jet analysis branch suffers from very low statistics ($\sim {}^{1}\!/_{100}$ compared to the 0 b-jet branch) which makes it difficult to obtain a reliable control sample for the background estimation. Therefore, the analysis is performed without the $\sum p_T^{jet}$ cut for an integrated luminosity of $4\,\mathrm{fb}^{-1}$. The corresponding numbers of events after each analysis cut are shown in Table 5.3. The ratio of the dilepton mass distribution for the ee control sample and the total $\mu\mu$ background as well as the for the $e\mu$ control sample and the $t\bar{t} \rightarrow \mu\mu + X$ background are shown in Fig. 5.29.

With this looser event selection one gains approximately 7 times more statistics which clearly improves the accuracy of the background estimation. The total background in this

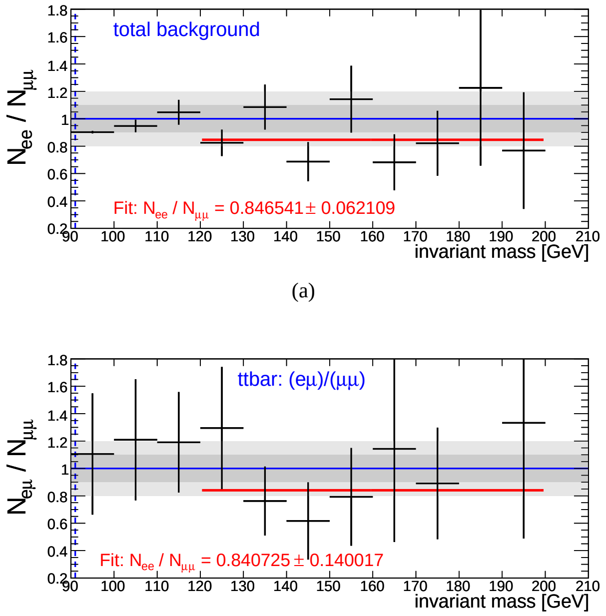

(a)

(b)

Figure 5.25: Ratio of the dilepton invariant mass distributions for the ee control sample and the total $\mu\mu$ background (a) and for the $e\mu$ control sample and the $t\bar{t} \rightarrow \mu\mu + X$ background (b) obtained in the > 0 b-jet final state at $4\,\mathrm{fb}^{-1}$.

case can be estimated with an accuracy of $9\,\%$ on the normalization and with better than $4\,\%$ on the shape. The normalization accuracy agrees well with the intrisic accuracy observed with the Monte Carlo truth. The estimate of the $t\bar{t}$ background from the $e\mu$ control sample achieves an accuracy of $15\,\%$ on the normalization and better than $6\,\%$ on the shape of the dilepton distribution.

This demonstrates that the looser selection criteria allow for a significant improvement of the background estimation, in particular related to the shape of the invariant mass distribution.

The $t\bar{t}$ background estimation from $e\mu$ control samples shows a lower normalization accuracy of $15\,\%$, compared to $\sim 6\,\%$ on the truth level. This may be explained by a systematic shift introduced by the rescaling of the dilepton invariant mass distributions which corrects for different electron and muon reconstruction efficiencies.

The lepton efficiencies used for the rescaling are determined from inclusive Z events, as this will be the data sample used for efficiency measurements with real collision data (using so-called tag-and-probe methods). On the other hand, as Fig. 5.30 shows, the reconstruction efficiencies, in particular for isolated electrons, are different in Z and $t\bar{t}$ events. This results in an underestimation of the correction for ee and $e\mu$ final states with respect to $\mu\mu$ final states in $t\bar{t}$, leading to a shift of the ${}^{N_{ee}}/{}_{N_{\mu\mu}}$ ratio. In the next chapter, this effect will be discussed more detailed in the context of systematic errors on the jet reconstruction.

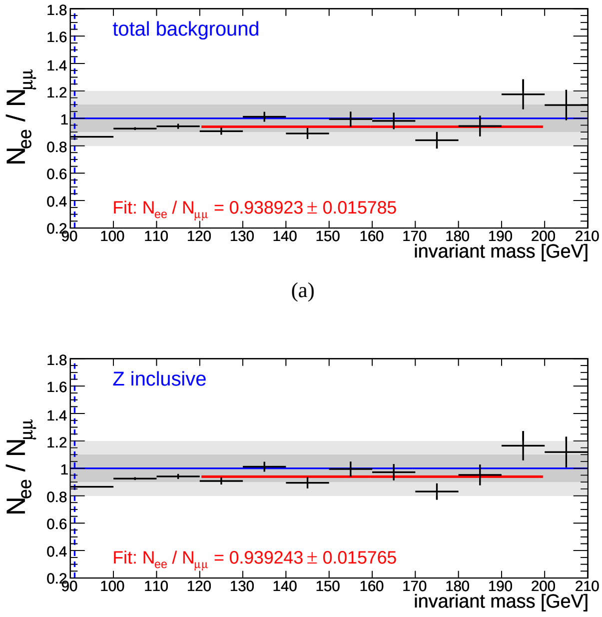

(a)

(b)

Figure 5.26: Ratio of the dilepton invariant mass distributions for the ee control sample and the total $\mu\mu$ background (a) obtained in the 0 b-jet final state at $1\ \mathrm{fb}^{-1}$. For comparison the dominant contribution from the Z sample (b) is shown in addition.

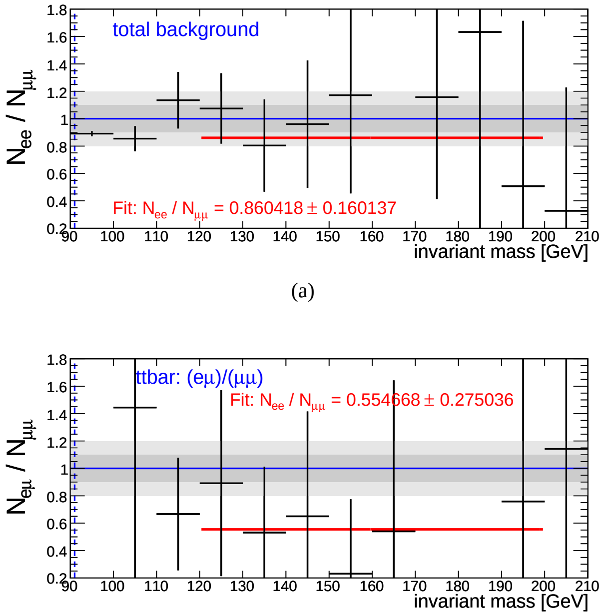

(a)

(b)

Figure 5.27: Ratio of the dilepton invariant mass distributions for the ee control sample and the total $\mu\mu$ background (a) and for the $e\mu$ control sample and the $t\bar{t} \rightarrow \mu\mu + X$ background (b) obtained in the > 0 b-jet final state at $1\ \mathrm{fb}^{-1}$.

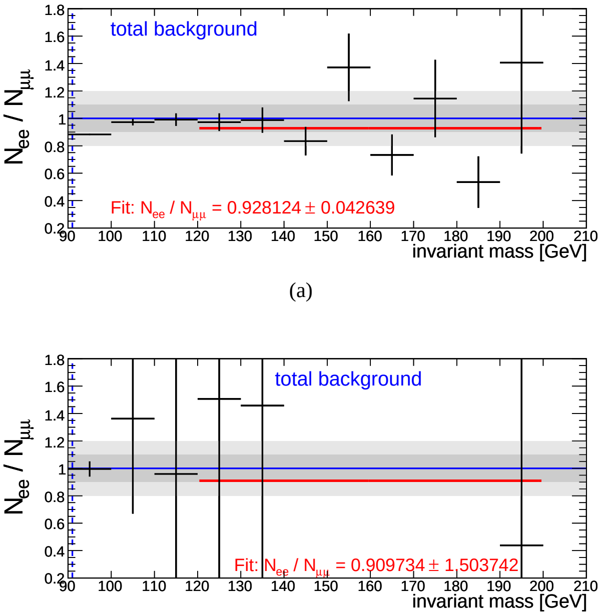

(a)

(b)

Figure 5.28: Ratio of the dilepton invariant mass distributions for the ee control sample and the total $\mu\mu$ background in the 0 b-jet analysis (a) and the b-jet analysis (b) at 200 pb^{-1} integrated luminosity.

Cut	$b\bar{b}A$ 130 GeV	$b\bar{b}A$ 150 GeV	$b\bar{b}A$ 200 GeV	Z *incl*	$t\bar{t}$
no cut	61.7	37.9	13.5	$1.144 \cdot 10^6$	$374 \cdot 10^3$
p_T, η	55.7[4]	34.2[2]	12.3[1]	$575.8[4] \cdot 10^3$	$44.16[9] \cdot 10^3$
ID quality	52.2[4]	32.0[2]	11.5[1]	$538.4[3] \cdot 10^3$	$39.99[8] \cdot 10^3$
isolation	49.0[3]	30.0[2]	10.8[1]	$508.6[3] \cdot 10^3$	$6.85[4] \cdot 10^3$
preselection	47.4[3]	29.2[2]	10.6[1]	$477.2[3] \cdot 10^3$	$5.42[3] \cdot 10^3$
E_T^{miss}	47.1[3]	28.9[2]	10.4[1]	$476.8[3] \cdot 10^3$	$1.28[2] \cdot 10^3$
b-jet requirement	9.1[1]	6.1[1]	2.49[5]	$7.06[4] \cdot 10^3$	$1.06[1] \cdot 10^3$
cos $\Delta\phi_{\mu\mu}$	8.8[1]	5.92[9]	2.44[5]	$6.59[4] \cdot 10^3$	$8.7[1] \cdot 10^2$
Δm (130 GeV)	7.6[1]			30[3]	63[5]
Δm (150 GeV)		5.09[9]		18[2]	55[4]
Δm (200 GeV)			2.04[4]	5[1]	30[3]

Table 5.3: *Cross section* × *selection efficiency* for the signal and the dominant background processes in the > 0 b-jet analysis with looser event selection (no $\sum p_T^{jet}$ cut) scaled to 1 fb^{-1}.

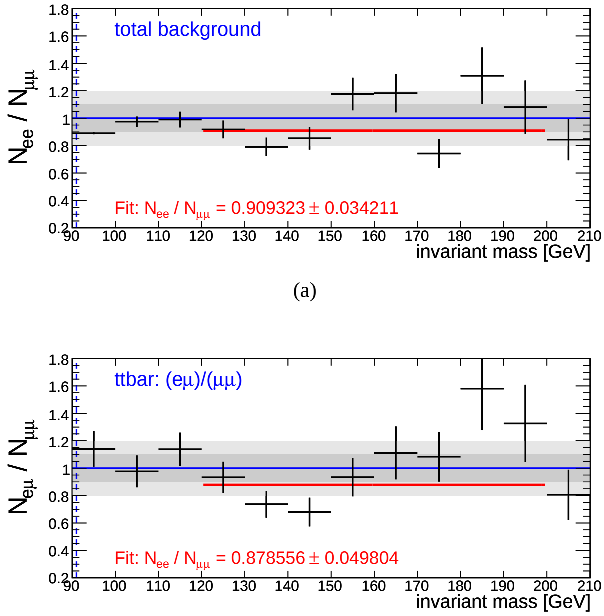

(a)

(b)

Figure 5.29: Ratio of the dilepton invariant mass distribution for the ee control sample and the total $\mu\mu$ background (a) and for the $e\mu$ control sample and the $t\bar{t} \rightarrow \mu\mu{+}X$ background (b) obtained in the > 0 b-jet final state at $4\,\text{fb}^{-1}$ without the $t\bar{t}$ rejection cut on $\sum p_T^{jet}$.

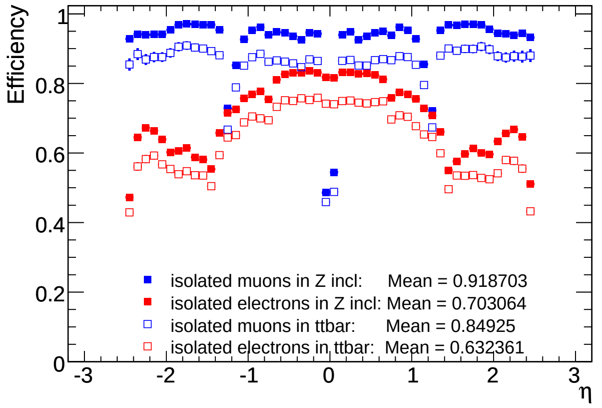

Figure 5.30: Reconstruction efficiencies for electrons and muons in bins of η in inclusive Z and $t\bar{t}$ events.

	0 b-jet		b-jet			
	total background		total background		$t\bar{t}$ background	
	norm.	shape	norm.	shape	norm.	shape
truth @ $4\,\mathrm{fb}^{-1}$	$< 6\,\%$	$< 1\,\%$	$9\,\%$	$< 2.5\,\%$	$5.5\,\%$	$3\,\%$
reco @ $4\,\mathrm{fb}^{-1}$	$< 6\,\%$	$< 1\,\%$	$15\,\%$	$7\,\%$	$16\,\%$	$17\,\%$
reco @ $1\,\mathrm{fb}^{-1}$	$6\,\%$	$2\,\%$	$16\,\%$	$19\,\%$	$45\,\%$	$50\,\%$
reco @ $200\,\mathrm{pb}^{-1}$	$7\,\%$	$< 5\,\%$	-	-	-	-
no $\sum p_T^{jet}$ cut @ $4\,\mathrm{fb}^{-1}$	-	-	$9\,\%$	$< 4\,\%$	$15\,\%$	$< 6\,\%$

Table 5.4: Overview of the achievable accuracies of the background estimation from signal-free control samples: for the 0 b-jet final state the total background can be estimated from the ee control sample, in the b-jet final state additionally the $t\bar{t}$ contribution can be estimated with the $e\mu$ control sample.

Chapter 6

Systematic Uncertainties

The impact of detector-related systematic uncertainties on the analysis results are evaluated in this chapter. The uncertainties concern the reconstruction of muons, electrons and jets, as well as the the b-tagging performance (Section 6.1). Two different scenarios are studied, one assuming uncertainties corresponding to an integrated luminosity of approximately $1\,\mathrm{fb}^{-1}$, and the other assuming larger uncertainties which correspond to $\sim 100\,\mathrm{pb}^{-1}$. Every systematic effect described in Section 6.1 was studied individually. The impact of the systematic uncertainties on the event selection efficiency and on the quality of the background estimation are studied in Section 6.2.

6.1 Sources of Systematic Uncertainties

Lepton Reconstruction Efficiency The lepton reconstruction and identification efficiencies will be measured with collision data [20], with a precision depending on the available integrated luminosity. To account for the uncertainties in the measured efficiencies, a certain number of reconstructed leptons is randomly removed from the Monte Carlo data sample in the analysis. The expected uncertainties for the different objects are listed in Table 6.1 for the two scenarios with integrated luminosities of $1\,\mathrm{fb}^{-1}$ and $0.1\,\mathrm{fb}^{-1}$.

	Efficiency degradation for	
	$\approx 1\,\mathrm{fb}^{-1}$	$\approx 0.1\,\mathrm{fb}^{-1}$
Muons	$-0.3\,\%$	$-1\,\%$
Electrons	$-0.5\,\%$	$-1\,\%$

Table 6.1: Expected systematic uncertainties on the measured reconstruction efficiency of muons and electrons.

Transverse Momentum and Energy Scale Systematic errors in the determination of the momentum and energy scales of the tracking detectors and the calorimeters, respectively, are, for example, caused by an imperfect knowledge of the magnetic field or deficiencies in the jet calibration. These effects can cause shifts either to higher or lower values of the momentum or energy. Both possibilities are treated separately. The assumed shift values are shown in Table 6.2.

Momentum Resolution Even though the studies in this thesis are performed using a detailed detector simulation, the distribution of the material in the detector is still not perfectly described. Uncertainties in the material distribution, as well as residual misalignment

	Momentum / Energy scale for	
	$\approx 1\,\text{fb}^{-1}$	$\approx 0.1\,\text{fb}^{-1}$
Muons	$\pm 0.3\,\%$	$\pm 1\,\%$
Electrons	$\pm 0.1\,\%$	$\pm 1\,\%$
Jets ($\lvert\eta\rvert < 3.2$)	$\pm 7\,\%$	$\pm 7\,\%$
Jets ($\lvert\eta\rvert > 3.2$)	$\pm 15\,\%$	$\pm 15\,\%$

Table 6.2: Expected systematic uncertainty on the lepton transverse momenta and on the jet energies.

of the detector components can degrade the momentum resolution of the leptons and the energy resolution of jets. Therefore additional smearing of the particle momenta is applied according to the values in Table 6.3.

	Resolution degradation for	
	$\approx 1\,\text{fb}^{-1}$	$\approx 0.1\,\text{fb}^{-1}$
Muons $\sigma\left(\frac{1}{p_T}\right)$	$\frac{0.011}{p_T} \oplus 0.00017$	$\frac{0.011}{p_T} \oplus 0.00017$
Electrons $\sigma(E_T)$	$0.0106 \cdot E_T$	$0.0106 \cdot E_T$
Jets ($\lvert\eta\rvert < 3.2$) $\sigma(E)$	$0.45\sqrt{E}$	$0.45\sqrt{E}$
Jets ($\lvert\eta\rvert > 3.2$) $\sigma(E)$	$0.63\sqrt{E}$	$0.63\sqrt{E}$

Table 6.3: Systematic uncertainties on the transverse momentum (energy) resolution of muons and electrons (jets).

b-Tagging Performance The efficiency of the b-jet identification and the corresponding rejection against light jets have important impact on the analysis. In the early phase of data taking, the performance of the b-tagging algorithms is expected to have large uncertainties since the algorithms rely on precise tracking and on details of the jet reconstruction. Therefore both the b-tagging efficiency and the rejection against light jets are varied separately according to the values in Table 6.4.

	b-tagging uncertainties for	
	$\approx 1\,\text{fb}^{-1}$	$\approx 0.1\,\text{fb}^{-1}$
Efficiency	$\pm 6\,\%$	$\pm 6\,\%$
Rejection	$\pm 10\,\%$	$\pm 10\,\%$

Table 6.4: Expected systematic uncertainties in the performance of the IP3DSV1 b-tagging algorithm, for the b-tagging efficiency and for the light jet rejection.

6.2 Impact of the Systematic Uncertainties on the Analysis

The previously described systematic uncertainties are implemented separately into the analysis. Their effects on the event selection and on the performance of the background estimation from control data are discussed in the following.

6.2.1 Event Selection in the Presence of Systematic Uncertainties

The systematic uncertainties described above can affect the total yields of both signal and background events after the selection criteria. The impact of the systematic effects is evaluated by separately taking into account the different error sources in the analysis. A conservative scenario with the larger uncertainties corresponding to an integrated luminosity of $\sim 0.1\,\text{fb}^{-1}$ was chosen for this study. A Higgs mass of $m_A = 130\,\text{GeV}$ was assumend and a mass window of $\delta m = m_A \pm 6\,\text{GeV}$ applied. Tables 6.5 and 6.6 show the relative change in the number of signal and background events in the mass window around the A boson mass for the 0 b-jet and the b-jet analysis branch:

$$\Delta = \frac{N_{with\ syst} - N_{without\ syst}}{N_{without\ syst}}. \tag{6.1}$$

Table 6.7 shows the relative change in the number of signal and background events in a mass window around the A boson mass for the b-jet analysis branch with looser event selection (no $\sum p_T^{jet}$ cut). Only the dominant systematic uncertainty on the jet energy scale is considered here and only the relevant data samples for the analysis for an integrated luminosity of $4\,\text{fb}^{-1}$ (inclusive Z and $t\bar{t}$) have been taken into account.
The $t\bar{t}$ sample seems to be most sensitive to systematic uncertainties, which can be explained by a high jet activity in these events. On the other hand, the statistical Monte Carlo uncertainty in the number of these events after all selection cuts is quite high ($\sim 12\,\%$).

systematic source	Signal	$t\bar{t}$	$Z + b$-jets	Z+jets	Z incl
muon resolution	-1.2	$+1.6$	$+0.76$	$+0.84$	-0.077
muon momentum scale ($-$)	-1.5	$+1.5$	-5.8	-4.0	-6.4
muon momentum scale ($+$)	-0.98	$+7.5$	$+8.1$	$+6.9$	$+5.8$
muon efficiency	-2.0	-3.0	-3.8	-2.7	-2.1
electron resolution	± 0	$+1.5$	± 0	± 0	± 0
electron momentum scale ($-$)	± 0	$+4.5$	± 0	$+0.022$	± 0
electron momentum scale ($+$)	± 0	± 0	± 0	± 0	± 0
electron efficiency	-0.022	± 0	± 0	± 0	± 0
jet resolution	-0.26	$+1.5$	-0.18	-0.012	-0.026
jet energy scale ($-$)	$+0.58$	$+27$	-1.1	-0.86	-0.31
jet energy scale ($+$)	-1.5	-24	-3.6	-1.04	-0.34
jet efficiency	± 0	± 0	± 0	± 0	± 0
b-tagging efficiency ($+$)	-0.60	$+1.5$	-1.2	-0.015	± 0
b-tagging efficiency ($-$)	$+1.3$	$+18$	$+3.3$	$+0.060$	$+0.077$
l-jet rejection ($+$)	$+0.022$	± 0	± 0	$+0.028$	$+0.039$
l-jet rejection ($-$)	-0.015	± 0	± 0	± 0	± 0

Table 6.5: Relative systematic shifts Δ (in $\%$) for the number of selected events in the signal for $m_A = 130\,\text{GeV}$ and for the major background processes for different sources of systematic errors in the 0 b-jet final state.

6.2.2 Impact of Systematic Uncertainties on the Performance of the Background Estimation from Control Data

The performance of the background estimation method introduced in Chapter 5 is evaluated in the presence of the systematic uncertainties. For that purpose, the fit of the ratio $N_{ee}/N_{\mu\mu}$ of the invariant mass distributions is performed for every systematic error separately. This

systematic source	Signal	$t\bar{t}$	$Z+b$-jets	Z+jets	Z incl
muon resolution	-1.1	$+1.4$	$+1.9$	-1.5	$+4.3$
muon momentum scale $(-)$	-1.5	±0	±0	-1.5	-4.3
muon momentum scale $(+)$	$+9.7$	-2.9	$+4.8$	$+2.5$	$+8.6$
muon efficiency	-2.2	-1.4	-1.6	±0	-3.2
electron resolution	±0	±0	±0	±0	±0
electron momentum scale $(-)$	±0	±0	±0	±0	±0
electron momentum scale $(+)$	±0	±0	±0	±0	±0
electron efficiency	$+0.13$	±0	±0	±0	±0
jet resolution	$+0.26$	-5.8	$+3.8$	-2.8	-1.1
jet energy scale $(-)$	-0.97	$+2.9$	$+6.8$	-19	-1.1
jet energy scale $(+)$	$+0.48$	-33	-4.0	-51	$+2.2$
jet efficiency	±0	±0	±0	±0	±0
b-tagging efficiency $(+)$	$+3.6$	±0	$+1.8$	±0	$+1.1$
b-tagging efficiency $(-)$	-5.3	-10	$-4,1$	±0	-4.3
b-tagging rejection $(+)$	-0.044	±0	±0	-4.6	-6.5
b-tagging rejection $(-)$	$+0.044$	±0	±0	±0	$+2.2$

Table 6.6: Relative systematic shifts Δ (in %) for the number of selected events in the signal for $m_A = 130\,\text{GeV}$ and for the major background processes for different sources of systematic errors in the > 0 b-jet final state.

systematic sources	Signal	$t\bar{t}$	Z incl
jet energy scale $(-)$	-8	-9	-6
jet energy scale $(+)$	$+3$	-28	$+4$

Table 6.7: Relative systematic shifts Δ (in %) for the number of selected events in the signal for $m_A = 130\,\text{GeV}$ and for the major background processes, for the dominant systematic uncertainty, the jet energy scale, in the > 0 b-jet final state using the looser event selection (no $\sum p_T^{jet}$ cut).

allows for the determination of the most dominant uncertainties. It is expected that some of the systematic effects cancel each other in the ratio ${}^{N_{ee}}/_{N_{\mu\mu}}$ such that the remaining uncertainty is smaller than the numbers in Tables 6.5, 6.6 and 6.7.

The effect of each of the 16 different sources of systematic uncertainty on the normalization and shape of the total muon background will be shown for three different integrated luminosities of $4\,\text{fb}^{-1}$, $1\,\text{fb}^{-1}$ and $200\,\text{pb}^{-1}$. As shown in Section 5.5, the b-jet analysis suffers from low statistics after all selection cuts. Therefore the evaluation of the systematic uncertainties in the b-jet final state is only performed for an integrated luminosity of $4\,\text{fb}^{-1}$.

For an integrated luminosity of $4\,\text{fb}^{-1}$ in the 0 b-jet final state the estimation of both the background shape and normalization is very robust against systematic uncertainties (see Fig. 6.1). The normalization is mainly affected by the jet energy scale, which causes a relative change of $\sim 4\,\%$. The shape is also mainly affected by the jet energy scale, but nearly the same accuracy of $\sim 8.4\,\%$ can be achieved for the estimation of the shape as in the absence of systematic uncertainties (instead of $\sim 8.3\,\%$).

The > 0 b-jet analysis is more sensitive to systematic effects related to the jet reconstruction (see Fig. 6.2). With the error on the jet energy scale taken into account, the normalization is underestimated by $10\,\%$ with respect to the case without systematic uncertainties The deviation of the shape is, however, less than $0.6\,\%$.

As proposed at the end of the previous chapter, one can loosen the event selection in order

to reduce the statistical uncertainties in the latter analysis mode by not applying the $\sum p_T^{jet}$ cut. The systematic uncertainties for this modified event selection arising from jet energy miscalibration are shown in Table 6.8. The higher accuracy on the shape estimation, due to the looser event selection is contrasted by an increased systematic uncertainty on the normalization.
The probable explanation why the effects of a systematic error in the jet reconstruction do not cancel each other in the $^{N_{ee}}/_{N_{\mu\mu}}$ ratios as expected is the following:
The set of quality cuts which defines medium electrons contains a loose isolation criterion. This implies that electrons are reconstructed with lower efficiency in events with high jet activity. For the re-scaling procedure, however, the isolated medium electron efficiency obtained from inclusive PYTHIA $Z \rightarrow ee$ events is used since for early data the lepton reconstruction efficiencies will be measured in inclusive Z events using tag-and-probe methods. Thus, the re-scaling procedure used in this work is only correct for events with low jet activity. In particular in $t\bar{t}$ events, the ee final states (and also $e\mu$) are underestimated. This causes exactly the shift in the $^{ee}/_{\mu\mu}$ ratios which can be observed in the previous chapter whenever the $t\bar{t}$ background cannot be neglicted.
If the cut on $\sum p_T^{jet}$ is not applied, one gains significantly more statistics, but on the other hand, events with a very high jet activity are selected. A systematic error of the jet energy scale can cause a broader distribution of the missing transvers energy E_T^{miss} in those events with high jet activity. Thus, it can be expected that in ee+jets final states more events are rejected by the E_T^{miss} cut than in $\mu\mu$+jets final states.
As a consquence, a systematic error on the jet energy scale produces a shift in the normalization to lower values when the jet energy is over- or underestimated.

The effect, caused by an underestimated re-scaling factor for $t\bar{t}$ events, is negligible in the 0 b-jet analysis mode, since in this case, the Z background is by far the dominating contribution. Thus, the background estimation method performs very stable in this final state even for lower integrated luminosities and in the presence of systematic uncertainties. The results for integrated luminosities of $1\,\text{fb}^{-1}$ and $200\,\text{pb}^{-1}$ can be seen in Figs. 6.3 and 6.4. For $1\,\text{fb}^{-1}$ the uncertainties of the normalization are similar as for $4\,\text{fb}^{-1}$ and the estimation of the background shape degrades by the order of only $2\,\%$. For $0.2\,\text{pb}^{-1}$ an additional systematic error source becomes important. An uncertainty in the momentum scale of electrons for example shifts the ee invariant mass distribution, whereas the muon distribtuion remains unshifted. This relative shift affects clearly the $^{N_{ee}}/_{N_{\mu\mu}}$ ratio. Nevertheless, the systematic errors on the momentum scale of leptons and the jet energy scale, result in a degradation of the background shape estimation of only $\sim 0.1\,\%$ each.

In conclusion, the presented background estimation method is very robust in the presence of systematic uncertainties for background shape. Table 6.9 gives an overview of the evaluated accuracies on the shape estimation including the total systematic uncertainties obtained form the quadratic sum of the single uncertainties. Applying the looser event selection the shape accuracy inproves by almost a factor of two while the systematic uncertainty remains almost unaffected compared to the tighter event selection. On the other hand it has been shown, that the method does not achieve reliable results for the estimation of the background normalization for the > 0 b-jet final state. For the 0 b-jet final state the normalization can be estimated but in both final states additional information on the normalization of the total background can be obtained from side band fits to the dimuon invariant mass distribtuion, as will be shown in the next chapter.

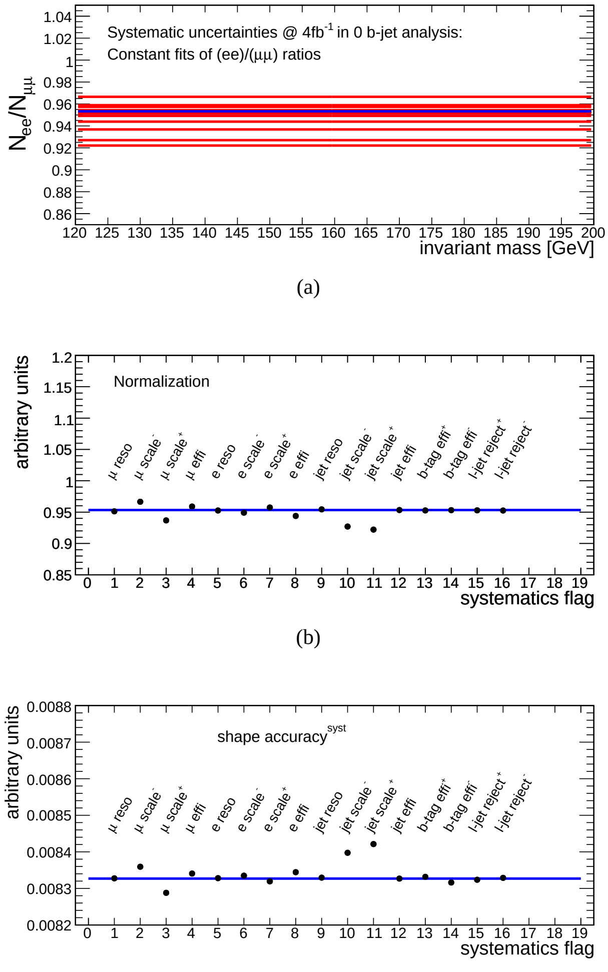

(c)

Figure 6.1: Systematic effects on the ratio $^{N_{ee}}\!/_{N_{\mu\mu}}$ of the total $\mu\mu$ background and the ee control sample for an integrated luminosity of $4\,\text{fb}^{-1}$ for the 0 b-jet analysis with (a) the fit results for each systematic effect, (b) the corresponding accuracy for the normalization and (c) the estimation of the background shape for every systematic effect separately.

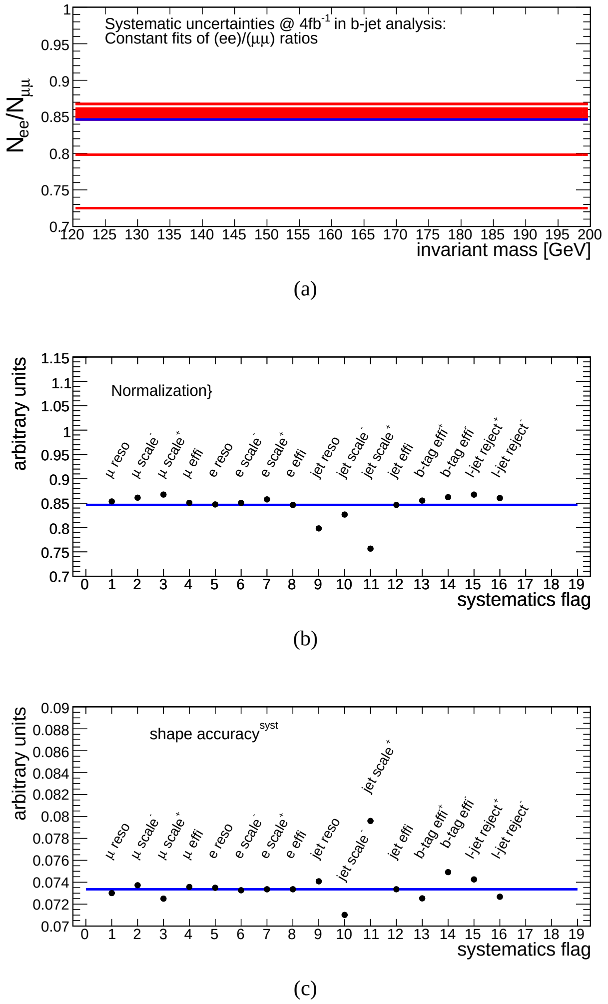

(a)

(b)

(c)

Figure 6.2: Systematic effects on the ratio $^{N_{ee}}/_{N_{\mu\mu}}$ of the total $\mu\mu$ background and the ee control sample for an integrated luminosity of $4\,\text{fb}^{-1}$ for the > 0 b-jet analysis with (a) the fit results for each systematic effect, (b) the corresponding accuracy for the normalization and (c) the estimation of the background shape for every systematic effect separately.

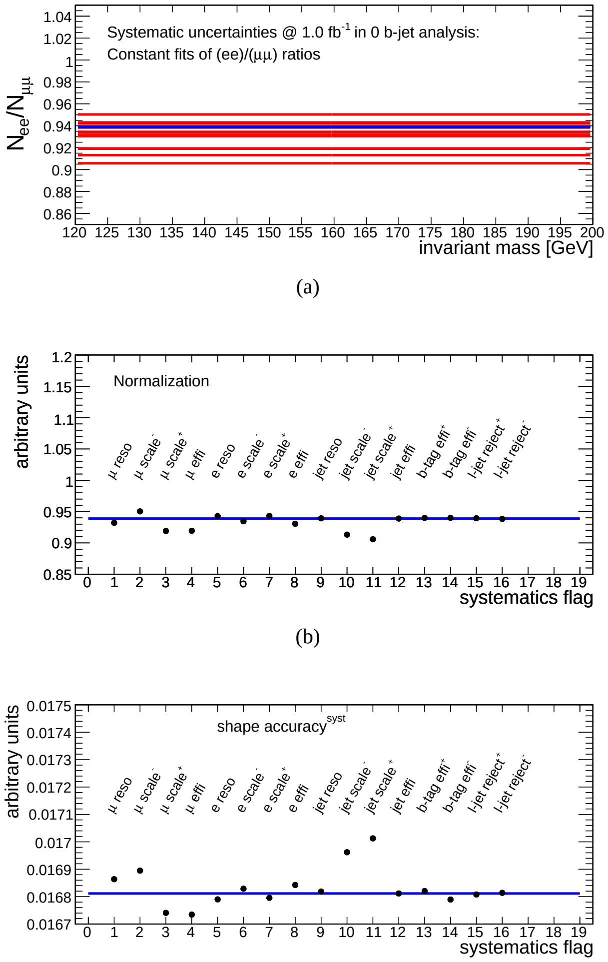

(a)

(b)

(c)

Figure 6.3: Systematic effects on the ratio $^{N_{ee}}/_{N_{\mu\mu}}$ of the total $\mu\mu$ background and the ee control sample for an integrated luminosity of 1 fb^{-1} for the 0 b-jet analysis with (a) the fit results for each systematic effect, (b) the corresponding accuracy for the normalization and (c) the estimation of the background shape for every systematic effect separately.

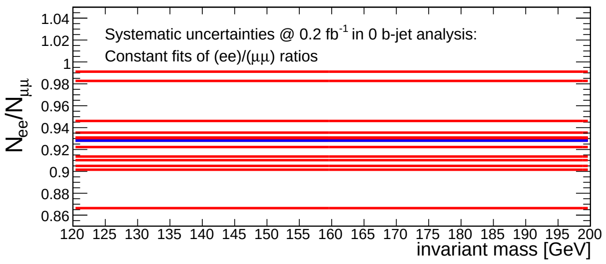

(a)

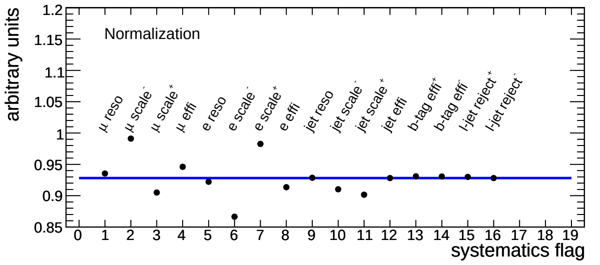

(b)

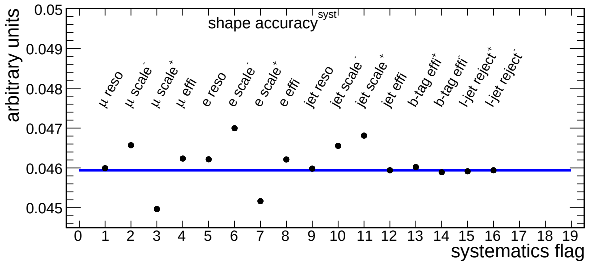

(c)

Figure 6.4: Systematic effects on the ratio $^{N_{ee}}/_{N_{\mu\mu}}$ of the total $\mu\mu$ background and the ee control sample for an integrated luminosity of $0.2\,\mathrm{fb}^{-1}$ for the 0 b-jet analysis with (a) the fit results for each systematic effect, (b) the corresponding accuracy for the normalization and (c) the estimation of the background shape for every systematic effect separately.

	norm	shape
no systematics	$-9\,\%$	$3.8\,\%$
jet energy scale ($+$)	$-16\,\%$	$4.6\,\%$
jet energy scale ($-$)	$-14\,\%$	$4.1\,\%$

Table 6.8: Accuracy for the estimation of the normalization and the shape of the total background in the presence of a systematic error on the jet energy scale, for the b-jet analysis without $\sum p_T^{jet}$ cut for an integrated luminosity of $4\,\text{fb}^{-1}$.

	$4\,\text{fb}^{-1}$	$1\,\text{fb}^{-1}$	$0.2\,\text{fb}^{-1}$
0 b-jet analysis	$(0.83 \pm 0.01)\,\%$	$(1.68 \pm 0.03)\,\%$	$(4.6 \pm 0.2)\,\%$
b-jet analysis	$(7.3 \pm 0.7)\,\%$	–	–
b-jet analysis (only jet energy scale)	$(7.3 \pm 0.7)\,\%$	–	–
b-jet analysis (loose) (only jet energy scale)	$(3.8 \pm 0.9)\,\%$	–	–

Table 6.9: Accuracy of the background shape estimation, including systematic uncertainties. For the looser b-jet analysis cuts only systematic uncertainties on the jet energy scale have been taken into account. Therefore, the uncertainties of the tight b-jet analysis cuts have been calculated once accounting for all systematic error sources and once, for comparison, only with the uncertainties on the jet energy scale.

Chapter 7

Evaluation of Exclusion Limits

In this chapter the limits for the exclusion of the $b\bar{b}A$ signal in the decay channel $h/H/A \to \mu^+\mu^-$ at the $95\,\%$ confidence level are calculated for the three mass points considered in this thesis. Mass degeneracy of the A and H bosons is assumed resulting in doubling the signal with respect of the pure A resonance. Exclusion limits are obtained from a fit of parametrized signal and background functions to the observed data. Results are shown for two scenarios. In the first case, the background contribution is obtained from the side bands of the signal region in the $\mu\mu$ invariant mass distribution. In the second case, the background fit is simultaneously performed on the $\mu\mu$ signal and the ee control sample.

7.1 Parametrization of the Invariant Mass Distributions

In order to evaluate the exclusion limits, a fit of the signal+background function $f_{SB}(x) = f_S(x) + f_B(x)$ is performed to the observed $\mu\mu$ invariant mass distribution. The background function $f_B(x)$ can in addition be fitted simultaneously to the invariant mass distribution from the ee control sample providing additional constraints on the background.

The total background is parametrized by a combination of a Breit-Wigner and an exponential distribution,

$$f_B(x) = \frac{p_0}{x} \cdot \left[\frac{1}{\left(x^2 - M_Z^2\right)^2 + M_Z^2 \Gamma_Z^2} + p_1 \cdot \exp\left(-p_2 \cdot x\right) \right], \tag{7.1}$$

where x is the dilepton mass and $p_{0,1,2}$ are the free fit parameters. The Breit-Wigner function with the mean M_Z and the width Γ_Z describes the Z resonance. The normalization factor p_0 is determined by the fit to the side bands of the signal region of the dimuon mass distribution since the control samples provide only limited accuracy for the normalization as shown in the previous chapters. The ee control sample can be used to constraint the parameters p_1 and p_2, controlling the background shape.

The $\mu\mu$ invariant mass distribution in the presence of a signal can be parametrized by the function

$$f_{SB}(x) = f_B + p_3 \cdot f_S = f_B + p_3 \cdot \frac{1}{p_4\sqrt{2\pi}} \cdot \exp\left(-\frac{(x-p_5)^2}{2p_4^2}\right), \tag{7.2}$$

where the background function f_B from equation 7.1 is superimposed by a Gaussian distribution f_S describing the signal. The parameter p_5 is the expected Higgs mass which can either be fixed or left free as a floating fit parameter. The width of the Higgs resonance is described by p_4 and the parameter p_3 corresponds to the total number of signal events.

7.2 The Profile Likelihood Method

The two fit functions introduced in Equations 7.1 and 7.2 are used to extract the number of signal-plus-background events N_{SB} and the number of background-only events N_B by integration over a mass window of $p_5 \pm 2\sigma_A$. For the evaluation of the exclusion limits the same procedure as in the reference analysis [21] is used, referred to as the *profile likelihood method*. The principles of this method explained in this section are described in [36, 37].

A given experimental observation (typically a distribution of a certain variable, like the dilepton invariant mass) is specified by the numbers of entries $\boldsymbol{n} = (n_1, ..., n_N)$ in a histogram with bins $i = 1, ..., N$. The number n_i of entries in bin i is assumed to be distributed according to a Poisson distribution with the mean value $E(n_i)$ given by

$$E(n_i) = \mu s_i + b_i, \tag{7.3}$$

where s_i and b_i are the numbers of signal and background events, respectively, described by the parametrization in equations 7.1 and 7.2. μ is the signal strength parameter defined such that $\mu = 0$ corresponds to the absence of a signal and $\mu = 1$ gives the signal rate expected from the MSSM cross sections. In the case of a fixed Higgs mass, the only parameter of interest is μ, while the remaining parameters needed to describe the measurement are called *nuisance parameters*. Since the signal and background are described by the fit functions f_{SB} and f_B, the nuisance parameters correspond to the fit parameters $p_{0,...,5}$.

If in addition a subsidiary measurement $\boldsymbol{m} = (m_1, ..., m_M)$ is available, i.e. in our case the ee background control sample, its entries also are assumed to follow the Poisson distribution with the mean value

$$E(m_i) = u_i, \tag{7.4}$$

where the quantities u_i are also determined by the above nuisance parameters.

The likelihood function is the product of the Poisson probabilities for all bins

$$L(\mu, \theta) = \prod_{j=1}^{N} \frac{(\mu s_j + b_j)^{n_j}}{n_j!} \exp\left[-(\mu s_j + b_j)\right] \prod_{k=1}^{M} \frac{u_k^{m_k}}{m_k!} \exp\left[-u_k\right], \tag{7.5}$$

where θ is the set of all nuisance parameters, i.e. $\theta = (p_0, ..., p_5)$. Equivalently the log-likelihood funktion is given by

$$\ln L(\mu, \theta) = \sum_{j=1}^{N} \left(n_j \ln(\mu s_j + b_j) - (\mu s_j + b_j)\right) + \sum_{k=1}^{M} (m_k \ln u_k - u_k) + C, \tag{7.6}$$

where C represents constant terms which can be dropped. The fit of the signal and background functions to the measured data is performed by minimizing the negative log-likelihood function $-\ln L(\mu, \theta)$. In equation 7.5 the first term corresponds to the fit of the signal-plus-background distribution to the $\mu\mu$ invariant mass distribution and the second term to the fit to the ee control data sample.

The probability for observing a signal with a given strength parameter μ can be probed by the profile likelihood ratio

$$\lambda(\mu) = \frac{L\left(\mu, \hat{\hat{\theta}}\right)}{L\left(\hat{\mu}, \hat{\theta}\right)} \tag{7.7}$$

of the two maximized likelihoods. $\hat{\hat{\theta}}$ represents the set of nuisance parameter values obtained when the likelihood function $L(\mu, \hat{\hat{\theta}})$ in the numerator is maximized for a fixed value

of μ. The likelihood function $L(\hat{\mu}, \hat{\theta})$ in the denominator is maximized by leaving both the parameter μ and the set of parameters θ free.
The result of the profile likelihood ratio can be expressed in the more convenient quantity

$$q_\mu = -2 \ln \lambda(\mu), \tag{7.8}$$

which allows for quantifying the agreement between the two likelihood functions in equation 7.7. Low values of q_μ (i.e. $\lambda(\mu)$ close to zero) correspond to a good agreement between the observed data and the scenario with assumed signal strength μ. If the observed value q_μ^{obs} is large, the probability for a signal with strength μ is low. If this probability is smaller than $5\,\%$, we claim an exclusion at a $95\,\%$ confidence level.

The probability for observing a given value q_{mu}^{obs} can be obtained by means of a large number of pseudoexperiments by varying each bin entry of the signal and background histograms corresponding to a Poisson distribution. Each pseudoexperiment gives one value of q_μ. All pseudoexperiments generate the probability density function $f(q_\mu \mid \mu)$. The p-value defined as

$$p_\mu = \int\limits_{q_{\mu,\,obs}}^{\infty} f\left(q_\mu \mid \mu\right) dq_\mu, \tag{7.9}$$

gives is the probability for a signal with strength μ. The lowest μ-value for which $1 - p$ is still greater than $95\,\%$ corresponds to the upper limit μ_{up} on the MSSM cross section.

7.3 Setting the Exclusion Limits

The result of the fits of the function f_{SB} is shown in Fig. 7.1 where the green and the black entries represent the ee control and the $\mu\mu$ mass distributions, respectively. In the two plots on the left the background-only hypothesis ($\mu = 0$) is fitted. The plots on the right hand side show the fit of the signal-plus-background hypothesis with a signal strength of 10 times the MSSM cross section for illustration. The purple line in each plot represents the fit result for the background where both, the $\mu\mu$ side band region and the ee control region are fitted simultaneously. The red line represents the fit results for the signal-plus-background distribution.
To determine the robustness of the fit procedure and accuracy of the background parametrization for the described method, a large number of Monte Carlo pseudoexperiments has been generated for a given integrated luminosity, with the signal strength set to zero. The above procedure is performed in each pseudoexperiment . Typical deviations $\Delta B/B$ between the number of events extracted from the fit and the number of actually observed background events in a mass window from $143 - 157\,\text{GeV}$ around the Higgs mass $m_A = 150\,\text{GeV}$ are shown in Fig. 7.2 for the 0 b-jet and the b-jet final state at three different integrated luminosities of $0.2\,\text{fb}^{-1}$, $1\,\text{fb}^{-1}$ and $4\,\text{fb}^{-1}$. The corresponding widths of the distributions are listed in Table 7.1. For the 0 b-jet final state the background can be measured with a very good accuracy already from the side bands of the $\mu\mu$ mass distribution alone. By accounting for additional information from the ee control sample the background resolution improves only slightly. In the b-jet final state the information from the control sample is crucial for the background estimation, in particular for low integrated luminosities $\mathcal{L} \leq 1\,\text{fb}^{-1}$. For $\mathcal{L} = 1\,\text{fb}^{-1}$ the accuracy of the fit nearly doubles if the ee sample is included in the fit. For $0.2\,\text{fb}^{-1}$ a fit can only be performed if the ee control samples are taken into account.
Another measure of the robustness of the fit is given by the fraction of pseudoexperiments in which the fit has successfully converged, relative to the total number of pseudoexperiments. The corresponding numbers are summarized in Table 7.2. Due to the relatively high statistics in the 0 b-jet final state the success rate of the two fits with and without the

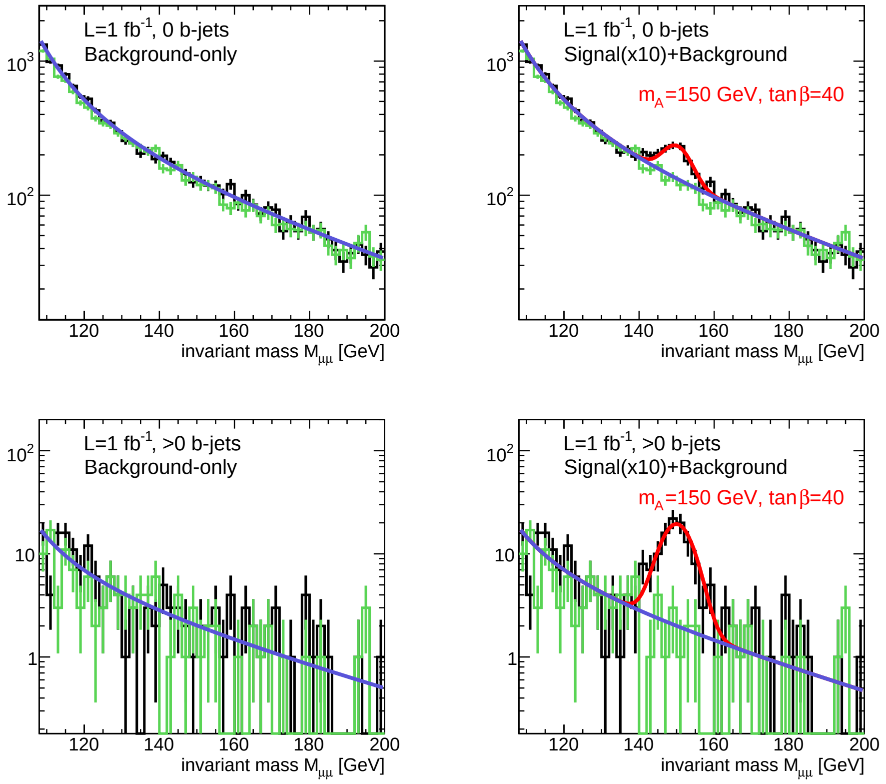

Figure 7.1: Fit of the function f_{SB} to the $\mu\mu$ and ee invariant mass distributions: The open and filled points represent the ee control data and $\mu\mu$ mass distributions, respectively. The purple line represents the result for the background from a simultaneous fit to the $\mu\mu$ and ee distributions. The red line represents the fit result for the signal-plus-background distribution. The signal mass parameter p_5 was fixed to $m_A = 150\,\text{GeV}$.

ee control samples are comparable, with a slightly degradation in the latter case for lower integrated luminosities. In the b-jet final state the difference between the two fit procedures becomes even more pronounced. For $0.2\,\text{fb}^{-1}$ and $1\,\text{fb}^{-1}$ almost no fits succeed if the ee control samples are not considered. Even for $4\,\text{fb}^{-1}$ the success rate is at the level of only $15\,\%$. On the contrary, if the control samples are used for the fit, the success rates are almost constant at a level of $\sim 80\,\%$.

Summarizing, we have seen that the parametrization of the background is very robust for both final states if the ee control samples are simultaneously used for the fit, down to a very low integrated luminosity of $0.2\,\text{fb}^{-1}$. If only the side band information from the $\mu\mu$ distribution is used for background measurement, reliable results can only be achieved in the 0 b-jet final state, or for very high integrated luminosities. The results thus show a clear improvement by means of the background estimation method developed in this thesis. To probe for the expected improvement in the performance of the $h/H/A \to \mu^+\mu^-$ analysis, the exclusion limits are calculated as a closing result in the following.

For the calculation of exclusion limits at a $95\,\%$ confidence level the previously introduced profile likelihood method is used. The p-value is evaluated different non-zero values of μ, with the restriction $\mu \leq \hat{\mu}$. The $95\,\%$ CL exclusion limit is reached for a given signal strength μ_{up} for which the p-value reaches its upper bound of 0.05.

The limits are calculated with respect to the neutral MSSM Higgs boson production cross sections at a benchmark point of $\tan\beta = 40$. The results for integrated luminosities of

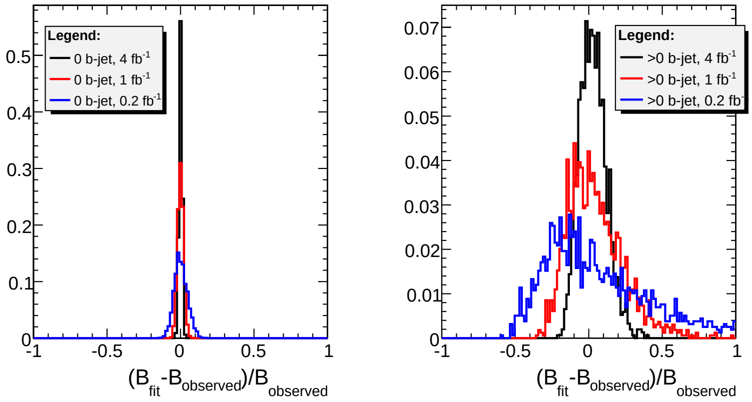

Figure 7.2: Relative difference between the observed number of background events $B_{observed}$ and the number B_{fit} obtained from the fit procedure described in the text for the mass window around $m_A = 150\,\text{GeV}$ in the 0 b-jet final state (left) and the > 0 b-jet final state (right). Both the $\mu\mu$ and ee mass distributions have been fitted.

	0 b-jet final state			> 0 b-jet final state		
M_A	0.2 fb^{-1}	1.0 fb^{-1}	4.0 fb^{-1}	0.2 fb^{-1}	1.0 fb^{-1}	4.0 fb^{-1}
130 GeV	4.4 %	2.0 %	1.1 %	34 %	17 %	9 %
	(4.6 %)	(1.9 %)	(1.1 %)	(×)	(33 %)	(8.7 %)
150 GeV	6.5 %	2.8 %	1.5 %	40 %	23 %	13 %
	(9.3 %)	(2.9 %)	(1.3 %)	(×)	(47 %)	(12 %)
200 GeV	11 %	5.4 %	2.8 %	48 %	35 %	21 %
	(11 %)	(4.9 %)	(2.4 %)	(×)	(73 %)	(42 %)

Table 7.1: Resolution $\sigma({}^{(B_{fit}-B_{observed})}/_{B_{observed}})$ obtained from the fit of the function f_{SB} (Eq. 7.2) to the invariant mass distribution. The results are obtained from a simultaneous fit to the $\mu\mu$ and ee invariant mass distributions. For the numbers in brackets only the $\mu\mu$ distribution is taken into account, i.e. the background contribution is determined by the side bands only.

0.2, 1 and 4 fb^{-1} in the two final states are given in Table 7.3 for different Higgs masses of m_A = 130, 150 and 200 GeV. A mass degeneracy of the two Higgs bosons A and H is taken into account leading to a signal which is twice as high as the single A resonance.
As can be seen in Table 7.3, neutral MSSM Higgs bosons with masses $M_A < 200\,\text{GeV}$ can be excluded with an integrated luminosity of $\sim$1 fb^{-1} for $\sqrt{s} = 10\,\text{TeV}$ collision data at $\tan\beta = 40$. The background estimation method introduced in this thesis allows for a slight improvement of the exclusion limits in the 0 b-jet final state. In the > 0 b-jet final state the benefit of this additional ee control sample is crucial. Due to very low statistics in this final state the limits cannot be set if only the side bands of the $\mu\mu$ distribution are considered. The shape information on the background shape from the control data, however, provides promising results even for integrated luminosites below 1 fb^{-1}.

	0 b-jet final state			>0 b-jet final state		
M_A	$0.2\,\mathrm{fb}^{-1}$	$1.0\,\mathrm{fb}^{-1}$	$4.0\,\mathrm{fb}^{-1}$	$0.2\,\mathrm{fb}^{-1}$	$1.0\,\mathrm{fb}^{-1}$	$4.0\,\mathrm{fb}^{-1}$
130 GeV	97 %	95 %	89 %	86 %	82 %	76 %
	(60 %)	(61 %)	(83 %)	(0.6 %)	(4 %)	(15 %)
150 GeV	88 %	94 %	87 %	87 %	81 %	79 %
	(50 %)	(64 %)	(78 %)	(0.6 %)	(3 %)	(15 %)
200 GeV	84 %	94 %	86 %	61 %	74 %	87 %
	(52 %)	(65 %)	(82 %)	(0.5 %)	(5 %)	(18 %)

Table 7.2: Fraction of pseudoexperiments in which the fit successfully converged. The results are obtained from a simultaneous fit to the $\mu\mu$ and ee invariant mass distributions. For the numbers in brackets only the $\mu\mu$ distribution is taken into account, i.e. the background contribution is determined by the side bands only.

	0 b-jet final state			>0 b-jet final state		
M_A	$0.2\,\mathrm{fb}^{-1}$	$1.0\,\mathrm{fb}^{-1}$	$4.0\,\mathrm{fb}^{-1}$	$0.2\,\mathrm{fb}^{-1}$	$1.0\,\mathrm{fb}^{-1}$	$4.0\,\mathrm{fb}^{-1}$
130 GeV	2.29	1.03	0.55	2.90	1.11	0.61
	(2.30)	(1.11)	(0.57)	(×)	(×)	(0.64)
150 GeV	2.08	0.76	0.27	4.81	1.51	0.86
	(2.09)	(0.78)	(0.28)	(×)	(×)	(0.89)
200 GeV	5.02	2.14	1.04	×	1.55	0.68
	(5.24)	(2.50)	(1.22)	(×)	(×)	(0.68)

Table 7.3: $\mu_{up}\times$MSSM Higgs production cross section which can be excluded at $95\,\%$ confidence level according to the pseudoexperiment estimate. The results are obtained from a simultaneous fit to the ee and $\mu\mu$ invariant mass distributions. For the numbers in brackets only the $\mu\mu$ distribution is taken into account, i.e. the background contribution is determined by the side bands only. Mass degeneracy of A and H bosons was assumed.

Chapter 8

Conclusions

The Large Hadron Collider (LHC) at CERN is now ready to start its operation and first proton-proton collisions are expected in late 2009. With its centre-of-mass energy of up to $\sqrt{s} = 14\,\mathrm{TeV}$ it will open up a new era in particle physics and allow to access a wide range of new physics phenomena.

The ATLAS experiment at the LHC is designed to study a wide spectrum of such phenomena and is expected to confirm the predictions of the standard model connected with the origin of particle masses or open up directions towards new theories beyond the standard model. The minimal supersymmetric extension of the standard model (MSSM) is one prominent candidate of such theories which could solve several problems of the standard model in an elegant way. The MSSM predicts five Higgs bosons, three neutral and two charged ones.

The subject of this thesis was the study of the discovery potential of the ATLAS experiment for the neutral MSSM Higgs bosons $A/h/H$ in the decay channel into muon pairs assuming a benchmark point in the MSSM parameter space with $\tan\beta = 40$.

The dominant production mode for neutral MSSM Higgs bosons at the LHC is the associated production mode with b-quarks. In spite of its low branching ratio, the decay $h/H/A \to \mu^+\mu^-$ provides a very clean signature and allows for an accurate Higgs mass measurement.

The $h/H/A \to \mu^+\mu^-$ decay process and the compelling background processes have been studied in detail with Monte Carlo simulations at a centre-of-mass energy of $\sqrt{s} = 10\,\mathrm{TeV}$ including a full simulation of the detector response.

Two complementary search strategies have been pursued: Final states without reconstructed b-jets provide a high signal selection efficiency but are plagued by the very high background contribution from $Z \to \mu^+\mu^-$ production. Final states with at least one reconstructed b-jet provide good suppression of the dominant Z background but lead to low signal efficiency and therefore to difficulties, in particular for the early collision data.

To discover or exclude neutral MSSM Higgs bosons, the background has to be estimated with a high accuracy in both analysis modes. A method for background estimation from measured collision data has been developed which uses control data samples with signal-free ee and $e\mu$ final states. The reliability of this method was evaluated for different integrated luminosities and modified event selection criteria taking into account the different reconstruction efficiencies for electrons and muons. It was shown that the lepton momentum resolution has negligible impact on this method, unlike energy losses due to final state radiation and Bremsstrahlung which, however, cannot be corrected.

The method presented predicts the background shape in the $\mu\mu$ invariant mass distribution very well and allows to put constraints on the background normalization. In the final state without reconstructed b-jets, the method is applicable even for integrated luminosities down to $200\,\mathrm{pb}^{-1}$. The shape of the background can be estimated with less than $5\,\%$ and its normalization with $\sim 7\,\%$ accuracy. In the more difficult final state with at least one

reconstructed b-jet one has to cope with very low statistics and therefore looser event selection criteria have been studied which should be considered for early data. In this case at least the shape of the background can be estimated with an accuracy of better than $\sim 5\,\%$ for an integrated luminosity of $4\,\text{fb}^{-1}$.
The impact of systematic uncertainties due to incomplete knowledge of the detector performance is an important aspect especially for early data taking. The background estimation method shows robust performance in the presence of systematic uncertainties and gives reliable results with accuracies af a few $\%$ for the estimation of the background shape for both the 0 b-jet and > 0 b-jet final states The normalization can at least be constrained in the 0 b-jet final state, while additional information has to be obtained from the side-bands of the signal region in the invariant $\mu\mu$ mass distribution.
Finally, the exclusion limits for the $b\bar{b}A$ signal at $\tan\beta = 40$ have been evaluated. In order to probe the performance of the background estimation method from the ee control samples, the limits have been evaluated for two cases. In the first one only the side-bands of the $\mu\mu$ mass distribution are used for background measurement. In the second case, the ee control sample is simultaneously used for the fit. While the control data improve the exclusion limits in the 0 b-jet final state only slightly, the are crucial for scenarios with very low statistics. In the b-jet final state at integrated luminosities below $1\,\text{fb}^{-1}$, exclusion limits can only be set if the control data information is used.

Bibliography

[1] L. R. Evans and P. Bryant. LHC Machine. *J. Instrum.*, 3:S08001. 164 p, 2008. This report is an abridged version of the LHC Design Report (CERN-2004-003).

[2] ATLAS Collaboration. The ATLAS Experiment at the CERN Large Hadron Collider. *J. Instrum.*, 3:S08008, 2008.

[3] A. Djouadi. The Anatomy of Electro-Weak Symmetry Breaking. I: The Higgs Boson in the Standard Model. Technical Report hep-ph/0503172. LPT-ORSAY-2005-17, Paris 11. Lab. Phys. Theor., Orsay, Mar 2005.

[4] H. Fritsch, Gell-Mann M., and Leutwyler H. Advantages of the color octet gluon picture. *Phys. Lett. B*, 47(4):365–368, 1973.

[5] S.L. Glashow. Partial-symmetries of weak interactions. *Nuclear Physics*, 22(4):579 – 588, 1961.

[6] A. Salam. Weak and Electromagnetic Interactions. Originally printed in *Svartholm: Elementary Particle Theory, Proceedings Of The Nobel Symposium Held 1968 At Lerum, Sweden*, Stockholm 1968, 367-377.

[7] S. Weinberg. A Model of Leptons. *Phys. Rev. Lett.*, 19(21):1264–1266, Nov 1967.

[8] Peter W. Higgs. Broken Symmetries, Massless Particles and Gauge Fields. *Phys. Rev. Lett.*, 12(9):132–134, Mar 1964.

[9] Peter W. Higgs. Broken Symmetries and the Masses of Gauge Bosons. *Phys. Rev. Lett.*, 13(16):508–509, Oct 1964.

[10] F. Englert and R. Brout. Broken Symmetry and the Mass of Gauge Vector Mesons. *Phys. Rev. Lett.*, 13(9):321–323, Aug 1964.

[11] G. S. Guralnik, C. R. Hagen, and T. W. B. Kibble. Global Conservation Laws and Massless Particles. *Phys. Rev. Lett.*, 13(20):585–587, Nov 1964.

[12] T. W. B. Kibble. Symmetry Breaking in Non-Abelian Gauge Theories. *Phys. Rev.*, 155(5):1554–1561, Mar 1967.

[13] The ALEPH, CDF, D0, DELPHI, L3, OPAL, SLD Collaborations, the LEP Electroweak Working Group, the Tevatron Electroweak Working Group and the SLD electroweak and heavy flavour groups. Precision Electroweak Measuremets and Constraints on the Standard Model. *CERN-PH-EP/2008-020*, 2008.

[14] A. Djouadi. The Anatomy of Electro-Weak Symmetry Breaking; Tome II: The Higgs Boson in the Minimal Sypersymmetric Model. Technical Report hep-ph/0503173. LPT-ORSAY-2005-18, Paris 11. Lab. Phys. Theor., Orsay, Mar 2005.

[15] F. Zwirner. The quest for low-energy supersymmetry and the role of high-energy e^+e^- colliders. *arXiv:hep-ph/9203204*, 1991.

[16] G. Degrassi, S. Heinemeyer, W. F. L. Hollik, P. Slavich, and G. Weiglein. Towards High-Precision Predictions for the MSSM Higgs Sector. *Eur. Phys. J. C*, 28(hep-ph/0212020. DCPT-2002-126. IPPP-2002-63. LMU-2002-11. MPI-PHT-2002-73. RM-3-TH-2002-19):133–143. 19 p, Dec 2002.

[17] B. C. Allanach, A. Djouadi, J. L. Kneur, W. Porod, and P. Slavich. Precise determination of the neutral Higgs boson masses in the MSSM. *J. High Energy Phys.*, 09(hep-ph/0406166. IFIC-2004-21. LAPP-TH-1046. MPP-2004-50. PM-2004-13. ZU-TH-2004-08):044. 56 p, Jun 2004.

[18] LEP Higgs Working Group. Searches for the neutral Higgs bosons of the MSSM: Preliminary combined results using LEP data collected at energies up to 209-GeV. *arXiv:hep-ex/0107030*, 2001.

[19] The TEVNPH Working Group. Combined CDF and D∅ upper limits on MSSM Higgs boson production in tau-tau final states with $2.2\,\mathrm{fb}^{-1}$ of data. *FERMILAB-PUB-09-394-E*, 2009.

[20] ATLAS Collaboration. Expected Performance of the ATLAS Experiment: Detector, Trigger and Physics. Technical Report arXiv:0901.0512. CERN-OPEN-2008-020, CERN, Geneva, 2009.

[21] ATLAS Collaboration. Search for the Neural MSSM Higgs Bosons in the Decay Channel $A/H/h \rightarrow \mu^+\mu^-$. In *Expected Performance of the ATLAS Experiment*, pages 1391–1418. CERN, 2009.

[22] Dobbs, M.A. and others. Les Houches Guidebook to Monte Carlo Generators for Hadron Collider Physics. *arXiv:hep-ph/0403045v2*, 2004.

[23] Agostinelli S. and others. GEANT4: A Simulation toolkit. *Nucl. Instrum. Methods Phys. Res., A*, 506(CERN-IT-2002-003. SLAC-PUB-9350. 3):250–303. 86 p, Jul 2002.

[24] Allison, J. and others. GEANT4 developments and applications. *IEEE Trans. Nucl. Sci.*, 53:270, 2006.

[25] ATLAS Collaboration. *ATLAS computing: Technical Design Report*. Number CERN-LHCC-2005-022 in Technical Design Report ATLAS. CERN, Geneva, 2005.

[26] E. Richter-Was, D. Froidevaux, and L. Poggioli. ATLFAST 2.0 a fast simulation package for ATLAS. Technical Report ATL-PHYS-98-131, CERN, Geneva, Nov 1998.

[27] The ATLFAST-II benchmark group. The ATLFAST-II performance in release 14 - particle signatures and selected benchmark processes -. Technical Report ATL-COM-PHYS-2009-554, CERN, Geneva, Oct 2009.

[28] S. Hassani et al. A Muon Identification and Combined Reconstruction Procedure for the ATLAS Detector at the LHC using the (MUONBOY, STACO, MuTag) Reconstruction Packages. *Nucl. Instrum. Methods Phys. Res., A*, 572(1):77–79, 2007.

[29] T. Lagouri et al. A Muon Identification and Combined Reconstruction Procedure for the ATLAS Detector at the LHC at CERN. *IEEE Trans. Nucl. Sci.*, 51:3030–3033, Dec 2004.

[30] ATLAS Collaboration. Muon Reconstruction and Identification: Studies with Simulated Monte Carlo Samples. In *Expected Performance of the ATLAS Experiment*, pages 162–184. CERN, 2009.

[31] ATLAS Collaboration. Reconstruction and Identification of Electrons. In *Expected Performance of the ATLAS Experiment*, pages 72–93. CERN, 2009.

[32] ATLAS Collaboration. Reconstruction and Identification of Photons. In *Expected Performance of the ATLAS Experiment*, pages 94–111. CERN, 2009.

[33] ATLAS Collaboration. Jets and Missig Transverse Energy. In *Expected Performance of the ATLAS Experiment*, pages 261–396. CERN, 2009.

[34] ATLAS Collaboration. b-Tagging. In *Expected Performance of the ATLAS Experiment*, pages 396–548. CERN, 2009.

[35] S. Gentile, H. Bilokon, V. Chiarella, and G. Nicoletti. Data based method for $Z \rightarrow \mu^+\mu^-$ background subtraction in ATLAS detector at LHC. Technical Report ATL-PHYS-PUB-2006-019. ATL-COM-PHYS-2006-043. CERN-ATL-COM-PHYS-2006-043, CERN, Geneva, Jun 2006.

[36] ATLAS Collaboration. Statistical Combination of Several Important Standard Model Higgs Boson Search Channels. In *Expected Performance of the ATLAS Experiment*, pages 1480–1511. CERN, 2009.

[37] Rolke W. R., Lopez A. M., and Conrad J. Limits and confidence intervals in the presence of nuisance parameters. *Nucl. Instrum. Methods Phys. Res., A*, 551(2-3):493–503, 2005.

List of Figures

List of Tables